This document is comprised by:

Response to Reviewer 1

We thank Reviewer 1 for her thoughtful and helpful second review of our paper. These insights motivate us to explore more possibilities to explain key observations and to particularly to explain our data and interpretations more clearly. We think that the Reviewer's comments have significantly improved the reasoning and clarity in our paper.

Reviewers comments are in blue type. <mark>Highlight:</mark> new text in the manuscript highlighted in the same colour.

Grain Boundary Sliding (GBS)

The main concern of the reviewer remains - why do we include GBS as an interpretation for the weaker CPOs of small grains? As we explain below, it is our misorientation axis data that push us to maintain inclusion of GBS as a viable, even likely process whereby nucleated grains can change orientation. We added these misorientation data after the first review to address this issue, but clearly had not used or explained these data effectively. We believe we have rectified these issues in the revised manuscript. Below is a detailed explanation of why the misorientation data are key to our interpretation.

We agree with the reviewer that subgrain rotation recrystallization is the most likely nucleation mechanism. We agree that, if the small grains represent nuclei developed through subgrain rotation recrystallization, they would likely have a wider dispersion of orientations than larger ("parent"?) grains. However, the accepted understanding of subgrain rotation recrystallisation is that immediately upon nucleation, a new grain should have an orientation relative to the parent that reflects the dislocation structure of the final subgrain boundary segment at the moment it becomes a grain boundary. This is implicit in the first descriptions of the subgrain rotation recrystallisation process (Guillope and Poirier, 1979; Poirier and Nicolas, 1975), is built into numerical simulations of the process (Gomez-Rivas et al., 2017; Signorelli and Tommasi, 2015) and is stated in all editions of John Humphrey's textbook (Humphreys and Hatherley, 1996; Rollett et al., 2017): "The orientation of the nucleus is present in the deformed structure. There is no evidence that new orientations are formed during or after nucleation, except by twinning" (from section 6.63, 7.63 or 7.62 depending on edition).

The rotation recrystallisation model, at least in part, was erected on the basis of misorientation data, although such data were very hard to collect at the time (Poirier and Guillope, 1979; Poirier and Nicolas, 1975; White, 1973). EBSD has made such data much easier to collect. One of the authors (Prior) was involved in one of the first more extensive EBSD investigations (Bestmann and Prior, 2003) of microstructures that would conventionally be explained recovery, subgrain rotation and subgrain rotation recrystallisation. In this study subgrains and recrystallised grains of approximately the same size are developed in a shear zone within a large crystal (the parent). Low-angle boundaries around subgrains have misorientation axes in rational crystallographic orientations, as would be expected for subgrain rotation. High-angle grain boundaries surrounding recrystallised grains have misorientation axes that are randomly oriented within the crystal, inconsistent with the operation of subgrain rotation recrystallisation alone. Bestmann and Prior (2003) explained these observations by allowing the newly formed nuclei to change orientation by sliding on grain boundaries. Comparable observations have been made in many dynamically recrystallised rocks (see citations of Bestmann and Prior (2003) and the reference list below) and many have been interpreted in the same way.

In our paper, the ice misorientation axes for low- and high-angle boundaries have the same general pattern as that identified by Bestmann and Prior (2003). Low-angle boundaries have

misorientation axes that are oriented tightly in the basal plane, consistent with these boundaries comprising arrays of dislocations that have developed by recovery and subgrain rotation. High-angle boundaries, on the other hand, do not have misorientation axes oriented in the basal plane, nor in any other preferred crystallographic orientation. This relationship still holds when the data are restricted to the high-angle boundaries between central large grains (parents?) and surrounding small grains in the "core and mantle" structures of the lower-temperature experiments. Explaining the misorientation data requires either a different nucleation mechanism (i.e. not rotation recrystallisation) or an additional process to change the orientation of grains during or after nucleation. The common interpretation of comparable data in the rock deformation literature (not just our group) is that GBS changes the orientation of grains after nucleation. For these reasons, we chose to retain GBS as our preferred explanation of the CPO data for nucleated grains.

We continue to emphasise that GBS is just one interpretation of the data, and we present the other possibilities that can explain the same observations. We think it is important to include GBS as a viable explanation of the data so that future generations of scientists can test its validity and importance.

The discussion of the role of grain size-sensitive processes (including GBS) in the evolution of the mechanical data has also been substantially reduced.

point-by-point reply to comments

R1.1: First, I acknowledge the simplification made by removing the part concerning the WBV study that was, indeed, not utilised enough. This lightens the paper, and makes it clearer.

Nevertheless, my remarks concerning the calculation of a subgrain size remains the same since, whether one uses the WBV analysis results, or misorientation measurements (here with a threshold of 10°) does not modify the fact that the results presented here do not show any subgrain substructure that would enable to identify an "average" subgrain size.

In the situation of figure R1.1 a, when considering the large grains separated by a unique and nearly straight subgrain, what is the subgrain size deduced from your measurement? The same question arises when considering the grains that are surrounded, at their boundaries by a few small subgrains. What is the subgrain size in this condition? Does it include the part of the inner part of the large grain (that is, indeed, a subgrain)? See figure below, within which we can really question the representativity of a subgrain size...

To bring this to light, maybe you could have plot not only the median, but the quartile, that would very likely have shown a large spread of data.

Since the authors strongly reduced the focus on the subgrain size data, this aspect concerning the metric is less critical, but the problem has not been solved to my point of view.

The stereological issues associated with WBV analyses will be presented in a separate paper, which is under preparation for future publication.

We thank the reviewer for pointing out some lack of clarity with respect to the metrics we use in subgrain size statistics. In our study, the subgrain size metrics consider all the inner parts of grains segmented by subgrain boundaries, including both large and small subgrains. Grains entirely surrounded by high-angle boundaries and without an internal subgrain boundary are also included, as the high-angle boundaries are above the chosen threshold for subgrain boundary misorientation. A figure from Trimby et al (1998) is useful here (Fig. R1.1). The upper picture shows boundaries with ≥4° misorientation, and the lower shows boundaries with ≥10° misorientation for the same field of view. If the subgrain boundary misorientation threshold is set at ≥4° and the grain boundary misorientation threshold is set at ≥10° then all the enclosed areas in the upper figure are counted as subgrains and all the enclosed areas in the

lower figure as grains. We have added a statement to section 2.5.1 to clarify this. This approach is a standard approach in geology and in metallurgy (e.g. (Adams et al., 1993; Coutinho et al., 2017; Humphreys, 2001, 2004; Sintay et al., 2009) although the values of the misorientation thresholds vary.
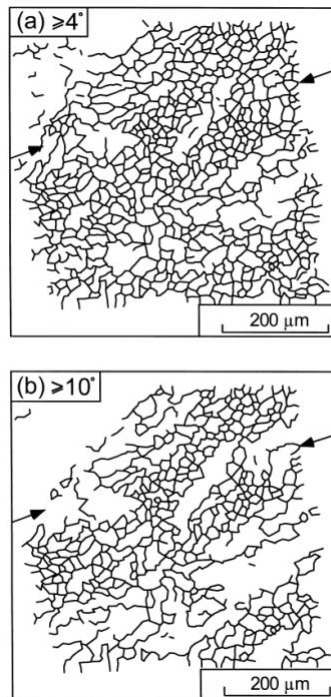
Fig. R1.1 Boundary misorientation maps for the low strain zone from quartz mylonite shear zone from Torridon, NW Scotland (after Fig. 5 from Trimby et al., 1998). (a) Boundaries with ≥ 4° misorientation. (b) Boundaries with ≥ 10° misorientation.

We also thank the reviewer for the suggestion of using interquartile measures to better describe the skewed subgrain size distributions. In the modified manuscript, we have added a lower quartile and higher quartile of subgrain size in Table 3 and the interquartile range (IQR), with upper and lower bounds constrained by higher and lower quartile subgrain size, respectively, that have been plotted along with mean and median subgrain size in Fig. 11(b). The related description of our approach is given in section 3.3.3.

R1.2 - Second, concerning the willingness of the authors to use GBS in order to explain the weakening associated to their observations.

Once again, there is absolutely no observation made here, neither the necessity, that render this GBS explanation robust.

Weakening can be explained by GBM, nucleation, subgrain rotation that are very clearly observed. Texture formation can be very well explained by the same processes, together with dislocation creep, and the results at -30°C are new and very interesting in the sense that they make a clearer link between nucleation of small grains and strong clustered texture, so here again, GBS is not necessary

… so why?

Why is it so necessary to evoke GBS?

Our reasoning for including GBS is explained at the beginning of this response to the reviewer (see above). We will add here that there has always been an issue with the microstructural identification of GBS. The microstructures that can be used to interpret the operation of the other processes, such as GBM (irregular-lobate boundaries), nucleation (in an experiment or a strain series in nature, determined by the increase in the number of grains), subgrain rotation

4

(low-angle boundaries, increasing misorientation angles with strain, rational misorientation axes) are clear and generally easy to identify. The signature of GBS is more subtle: if a grain rotates by sliding on its boundary, how does one recognize that in a final microstructure? To understand the difficulty of identifying GBS in experiments, it is worth looking at the beautiful syn-microscopic experiments on octachloropropylene published by Jin Han Ree (Ree, 1994), described below.

Fig R1.2 shows part of Ree's Figure 10; a time series of drawings of the microstructure. Ree was able to use marker particle lines to demonstrate translational movement on grain boundaries (GBS). In the absence of the (fiducial) marker lines, or some other strain marker, it would be very difficult to identify GBS, even in the case of a time-series experiment. The single time step microstructures show good evidence of GBM (lobate boundaries) and subgrain rotation (low angle boundaries) but finding evidence for GBS in a single microstructural image is difficult.
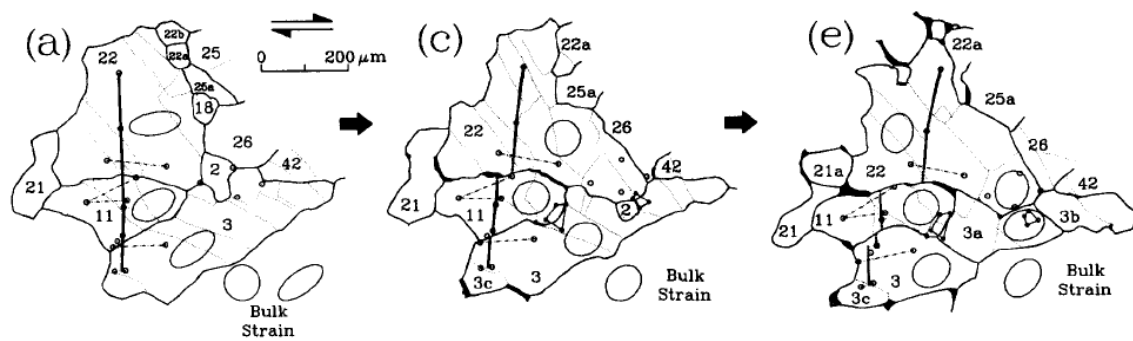
Figure R1.2 Part of Figure 10 from Ree (1994), showing a time series of drawings of the microstructure of deforming octachloropropane.

This is why the misorientation axis criteria outlined earlier in this response are so important. The change from crystallographically controlled low-angle boundaries to high-angle boundaries with little crystallographic control requires explanation and could be a GBS signal. In the case of our experiments, this interpretation works bests for the low-temperature experiments, but in the -10 °C experiments it is less clear, as the "core and mantle" structures are absent. It is likely that GBM will modify the grain boundary topology, particularly in those warmer experiments. Ree's experiments shown above and other time series experiments (Drury and Humphreys, 1988) show that GBM and GBS can (and indeed must, Ashby, 1972; Sundberg and Cooper, 2008) operate in parallel and that GBS would be cryptic in a final microstructure.

We have restructured the discussion to address the reviewer's concerns. The misorientation data are now discussed more thoroughly in section 4.1.2.2. (Dislocation activity, recovery, subgrain rotation and subgrain rotation recrystallisation). In this section we highlight the difference of misorientation axes of low- and high-angle boundaries and the implication that subgrain rotation recrystallisation alone cannot explain these data. GBS is not mentioned in this section. In section 4.1.4 (CPO development: differences related to grain size) we discuss the greater orientation spread of the small grains. We note that subgrain rotation recrystallisation can give a bigger orientation spread, but the lack of crystallographic control across high-angle boundaries, particularly the small-large grains in core and mantle structures (in the cold experiments), means that it is difficult to explain the weakening of the CPO by subgrain rotation recrystallization alone. We then discuss briefly two ways to explain these

data: a different nucleation process (nucleation with random orientations) and GBS following nucleation. We state (in section 4.1.4) that data to infer GBS in the higher-temperature experiments are less clear but we still allow that it is possible, given the cryptic nature of microstructures under conditions where enhanced GBM and GBS coexist, as discussed above.

We emphasize that the interaction of GBS with dislocation processes and GBM is well-recognized in the ice literature. Duval (1985) states "*Grain boundary migration associated with grain growth appears to be an efficient accommodation process for grain boundary sliding and dislocation glide.*" The literature review by Faria and others (2014) states: "*Hondoh and Higashi (1983) and Liu et al. (1993, 1995) used X-ray topography to study the interactions between dislocations and grain boundaries in ice bicrystals and polycrystalline ice, respectively. They could demonstrate that the regions surrounding grain boundaries (viz. the "mantle" of the grain, after Gifkins, 1976) generally deform before the grain interiors (viz. the "core" of the grain). Dislocations are emitted from stress concentrations at grain boundaries, caused by strain misfits and/or grain boundary sliding, and this process completely overwhelms any lattice dislocation generation mechanism.*" and "*Above -10 °C, the increase of the minimum strain rate with temperature is enhanced and the Arrhenius law breaks down (Glen, 1955, 1975; Hooke, 1981; Budd and Jacka, 1989). It is believed that grain boundary sliding and the presence of water within the grain boundaries may be the main causes of this creep enhancement (Barnes et al., 1971)*".

R1.3: Let me mention that most of the articles evoked to justify GBS are coming from the same team as the authors', and also mention GBS as an interpretation, and are not providing any evidence of GBS. These interpretations are basically all built on the only observation of area with small grains.

To address the reviewer's comment that most of the interpretations of GBS are from the authors' group, we provide two lists of published papers on ice and rock deformation in which GBS is a key interpretation of mechanical data and/or microstructural observations or is integral to the description of deformation. The lists are appended to the end of this document and are separate from the main reference list for this document.

GBS is accepted as a process that can occur in rock deformation. The data we use to infer GBS from ice microstructures is very similar to data used to infer GBS from rock microstructures, by us and by many other authors. *List 1* (page 11-13) is an incomplete list of papers that have inferred GBS in rocks in the last 5 years: generated from a quick Web of Science search, with a manual check that the paper really does infer GBS. We have not included papers from our broad group although authors who Prior and Goldsby have published with are highlighted (neither Prior or Goldsby had any role in these publications).

GBS in the ice microstructure literature extends to authors well beyond our broad research group. We are responsible for approximately a quarter of the papers that infer GBS in ice (see *List 2* (page 13-14)).

R1.4: On top of that, I have a strong concern about the explanations given after my comment 8-2, and based on figure R1.5.

The flow laws that are commonly used to characterized the mechanical response of a material are based on STATIONNARY behaviors, even if very short such as the peak stress for ice (or minimum creep rate in constant load conditions). Therefore a law of the type given by equation R1.1 (or the Glen's law for the minimum creep rate of ice), does hold only during this (pseudo) stationnary state. In the case provided by the curves of figure R1.5, the only place where it should be tested is the peak stress, since no other minimum, maximum or stationary behavior could be reached (such a stationary state is sometime reached during tertiary creep after 10% strain, as in Treverrow et al. 2012 for instance, but this quasi-stationary behavior results from a balance between a recovery process and a hardening one).

We thank the reviewer for their comment. A time-dependent parameter should be considered during the modelling of ice mechanical behaviour. This is a very useful suggestion, as we are modelling ice mechanical behaviour based on grain size and CPO data in another paper. We realise there are balances of mechanical hardening and softening mechanisms as the strain increases during ice deformation. Modelling the ice mechanical behaviour is beyond the scope of this paper, and we have reduced the discussion of it significantly in this paper. We plan to present a much more complete analysis of our data and literature data in a separate paper.

R1.5: One comment about figure R1.6: Wheeler et al. 1999 make it very clear, in the way they evaluate the WBV, that it is not an absolute measurement, and that it only provides an "lower bound", and therefore can only be used as a comparative tool with a lot of care (same type of surfaces observed, very similar deformation history, enough grains for enough statistics, etc...). We have tried to be very careful about that in our papers (Chauve et al. 2017, and Journaux et al. 2019) although our quantitative comparison must still be taken with care, and we made it "relative" (WBV_c / WBV_a). I thank the authors for this clear demonstration of such a necessity to treat this type of EBSD analysis with care.

We thank the reviewer very much for appreciating our work related with stereological issues of WBV. The stereological issues associated with WBV analyses will be presented in a separate paper, which is under preparation for future publication.

R1.6: About comment 14-1: I am sorry to read that a link was done between "spontaneous" nucleation and the study by Falus et al. 2011. Spontaneous nucleation, like modelled by Duval et al. 2012 can not give any clue about the nucleus orientation... and Chauve et al. 2017 only evoked it as a way to explain an orientation (of one single nucleus!) that had, apparently, no relation with the parents' orientations. Falus et al. 2011, and applicable also for most nuclei observed by Chauve et al. 2017, mentioned subgrain rotation (rotation or continuous recrystallization) as the main explanation for a weakening of the texture, and orientation spread away from the parent grain orientations, but not totally disconnected from these initial orientations. In section 4.1.4, mentioning nucleation by subgrain rotation (including bulging resulting from strain induced grain boundary migration, as in Chauve et al. 2017b) would be enough to explain the texture weakening, and more in phase with your observations in the small grain networks where small grains keep a strong relation of orientation with parent grains, cf fig 7b and 12 (such as explained by Humphreys and Haterly 2004 for metals, but already mentioned to impact recrystallization texture by Guillop. and Poirier 1979, suggested also for recrystallization along ice core by De La Chapelle et al. 1998, and clearly shown by Falus et al. 2011). Spontaneous nucleation is not expected to produce nucleus with any specific orientation, and GBS could also lead to very different orientations that are not observed here. By the way, the increasing role of subgrain rotation with decreasing temperature (clearly stated in your conclusion, points 2 and 3), together with the fact that there is more difference between small grain orientations and large grain orientations at lower temperature is coherent with the dominant role of nucleation by subgrain rotation at lower temperature.

We apologize for making an improper connection between "spontaneous" nucleation and the study by Falus and others (2011). Falus and others (2011) suggest that subgrain rotation recrystallization has a contribution to CPO weakening but cannot explain the most extreme dispersions in the recrystallised grain orientations as these exceed what is even possible by subgrain rotation (p1532). Their interpretation is that "*The higher dispersion of the olivine CPO in the mylonites may be attributed to a more important contribution of bulging processes to nucleation, which allows for higher misorientations between parent and recrystallized grains.*"(p1539). We cannot compare directly with the Falus et al. data set as they only show misorientation axis data for low-angle boundaries; instead their interpretations are informed by dispersion data for individual crystal directions. They do not rule out GBS: "*Finally, although the studied samples present no clear evidence for grain boundary sliding, this process might also contribute to a higher dispersion of the CPO in the finest-grained samples.*" (p1539).

Extracted from the longer comment above: nucleation by subgrain rotation (refs) would be enough to explain the texture weakening, more in phase with your observations in the small grain networks where small grains keep a strong relation of orientation with parent grains, cf fig 7b and 12. This response, in part, repeats what we have already said, but we would like to address this sub-comment directly. The coloured dispersed orientations in fig 7b represent the larger grains (ref 1-5) in 7a and their dispersion pattern (~

great circles) and the misorientation axes of low-angle boundaries (7c) fits a recovery and subgrain rotation model as shown schematically by the grey dashed line representing subgrain boundaries in fig 12 (labelled SGR-subgrain rotation, but not recrystallisation). We think we are in agreement with the reviewer in this part of the interpretation. The problem comes in linking neighboring small grains and large grains. The left-most figure of 7d (ref 1), for example, shows all of the misorientation axes between pixels on either side of the grain boundary enclosing grain ref1 (i.e., all misorientations linking pixels along the boundary of grain ref1 to neighbouring pixels in small grains). These are high-angle boundaries so the angular error on the misorientation axis is low. Each cluster in this fig relates to misorientations to a single grain and the variance in each cluster relates to the internal distortion of ref1 and the small grain in question. The misorientations for ref1 (or any of the other ref grains) do not lie in the basal plane and have no preferred nor rational crystallographic orientation. Subgrain rotation recrystallisation can be considered a nucleation mechanism for the small grains, but alone it cannot explain the misorientation axes of the high-angle boundaries. Either a different nucleation mechanism is needed, or an additional process is needed to change the orientation of grains during or after nucleation.

We thank the reviewer for clarifying their view of nucleus orientations associated with spontaneous nucleation. In our discussion we now refer to nucleation of grains with random orientations rather than spontaneous nucleation. There is some precedent for this idea in publications on metals deformed at high homologous temperatures that interpret small recrystallised grains as nuclei with random orientations (Hasegawa and Fukutomi, 2002; Hasegawa et al., 2003). The proposed mechanism for the randomly oriented nuclei is that they are produced at the tips of irregular boundaries of "parent" grains, without introducing GBS (Hasegawa and Fukutomi, 2002; Hasegawa et al., 2003).

R1.7: Another question, that I am not sure to have asked in the previous comments: at strain rates close to 10-5 s-1, with no hydrostatic pressure, ice is weakening by the formation of decohesion or fracture at or close to grain boundaries, in order to accommodate the imposed strain and the strain incompatibilities between grains. The hydrostatic pressure prevent microcracks to open, but then, what could be its impact on recrystallization mechanisms? And could it be that, as in Bourcier et al. 2013, a regime so close to the brittle behavior would, indeed, enhance GBS by the help of microcracks and decohesion?

The chief purpose of the confining pressure in these experiments is to suppress brittle phenomena including cracking and frictional sliding. Figure R1.3 shows the experiment with the highest differential stress, plotted on a Mohr diagram for stress. The green circle shows the shear and normal stresses for surfaces of all orientations and the maximum (σ_1) and minimum ($\sigma_3 = \sigma_2 =$ confining pressure) plot along the line of zero shear stress. Superposed are two failure envelopes. One is a Coulomb (frictional sliding) envelope using the friction coefficient for ice-ice sliding from McCarthy et al. (2017). Coulomb envelopes usually underestimate brittle strength. The second failure envelope is the composite envelope from Beeman et al. (1988). Red and blue Mohr circles show the stress states needed for brittle failure at a confining pressure of 20 MPa with each of these envelopes. Maximum differential stresses applied in our experiments are substantially below those for needed for frictional sliding or brittle failure. Ice deformed in the study were far away from the brittle or frictional sliding regime.
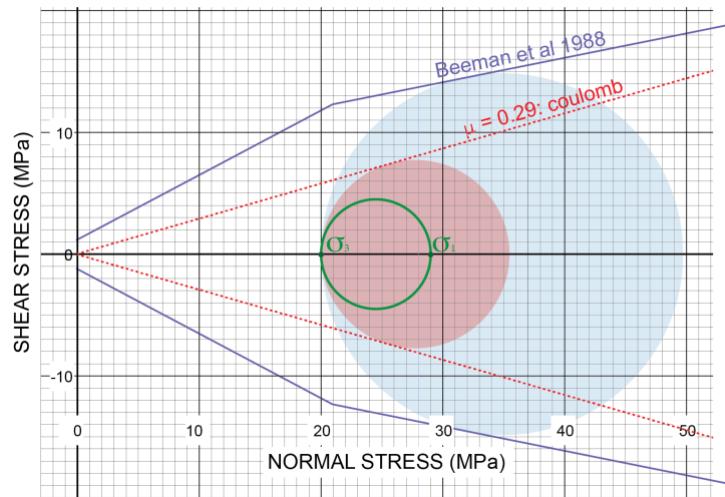
Figure R1.3. Mohr diagram showing stress state of sample PIL164 (the largest differential stress) in green. A coulomb failure envelope using a friction coefficient of 0.29 from (McCarthy et al., 2017) is shown with a red dashed line and the Mohr circle for failure at 20MPa confining pressure is shown in red. The blue lines show the (Beeman et al., 1988) failure envelope from and the Mohr circle for failure at 20MPa confining pressure is shown in blue.

The effect of pressure in affecting recrystallisation processes of ice is not fully investigated. We have very similar results from microstructural and mechanical from -10 °C experiments at 10MPa and 20MPa and warm temperature experiments at -5 °C have microstructures very similar to the many published unconfined experiments at this temperature, so at present we do not think the pressure has a significant effect on recrystallisation. In the Bourcier and others (2013) paper the bulk tests image unconfined free surfaces and the SEM tests image free surfaces under high vacuum. These are great experiments and clearly cracking and GBS are closely linked processes, but in the unconfined state at the strain rates they employ cracking is expected. The confining pressure in our experiments puts our experiments further away from the brittle field than a typical unconfined ice experiment. The Mohr analysis outlined above estimates that the shear stresses developed are at least ~3 MPa below what would be needed for shear failure and no tensile stresses will be developed in the sample.

R1.8: Abstract: lines 9-11. Please correct, see previous comment, by replacing the mention to spontaneous nucleation by the mention of nucleation by rotation of subgrains (rotation recrystallization) instead. Spontaneous nucleation model, as existing so far, does not allow to predict any type of orientation relation between nuclei and parent grains.

We have replaced references to "spontaneous nucleation" with "nucleation of grains in random orientation". As discussed in previous responses nucleation by subgrain rotation recrystallisation alone is not consistent with high-angle boundary misorientation axis data.

R1.9: Part 3.3.2: I don't understand what is this square mean root diameter... I know Root Mean Square parameter (RMS), that is square(mean(x^2)), and that has a statistical meaning, but I don't know the meaning of mean((square(x))^2), or (mean(square(x)))^2, it is not clear... Please verify

Square mean root diameter ($D_{SMR} = (\overline{\sqrt{D}})^2$), with the equation shown in section 3.3.2, is different from root mean square. Root mean square will exaggerate the difference between finer and coarser grain sizes, because each grain size will be squared before averaging. On the contrary, square mean root will decrease the difference between finer and coarser grain sizes, because the root of each grain size will be before averaging. The square mean root diameter is often useful for dynamically recrystallised grain sizes, as a frequency (probability) plot of the square root of grain size (or the log of grain size) often approximates a normal distribution.

9

R1.10: Part 3.4.4, line 14: Fig 8-10 instead of 9-11?

Corrected.

R1.11: p 12 line 27, "strai,n" → "strain"

Corrected.

R1.12: p 15 line 9, only here is the definition of "number density" given while it is used before, please give the definition when first using it.

We thank the reviewer for catching this unclear statement. We have clarified terminology in section 4.1.2.1 and elsewhere refer to the number of grains per unit area.

R1.13: p 16 line 2: reference by Placidi et al. 2004 has no reason to be here since it is modeling.

We have removed the reference of Placidi et al., 2004.

R1.14: p16 line 16-17: I don't see why is this study by Eleti et al. mentioned here? I would suggest to keep it for the discussion part.

We have removed the reference of Eleti et al., 2020 from section 4.1.2.2. This reference is kept in the discussion part.

R1.15: p 16 line 20: please also mention the reduced role of GBM when decreasing temperature in impacting the grain size! This is likely the most important one, since grain boundary mobility is strongly reduced...

The rate of GBM depends on two parameters - the boundary mobility, which is a function of temperature, and the driving force, conventionally defined by the dislocation density difference (Humphreys and Hatherley, 1996). The dislocation density difference is likely to be controlled by stress (Bailey and Hirsch, 1960; Ajaja, 1991). At a lower temperature, the grain boundary mobility is likely to reduce as suggested by the reviewer. However, the differential stress for a given strain rate increases (Fig. 3). Consequently, the dislocation density difference is likely to be higher at a lower temperature. We have adjusted the text (in section 4.1.2.3) to incorporate this line of discussion.

R1.16: Part 4.1.4: please see my comment about the various hypotheses for nucleation mechanisms and impact on texture.

Again here, the two strong hypotheses to mention concerning the weakening of texture in the small grains would be (1) nucleation by subgrain rotation (strengthened by the observation of subgrains whatever the level of strain and the temperature conditions), and (2) GBS in the fine grain necklace (I am not convinced, but let's assume it as a likely mechanism, and here you could mention the ref of Eleti et al.). The first hypothesis has been documented directly and indirectly by several authors (see reference in my previous comment on this subject, but there might exist others). Spontaneous nucleation could be mentioned, but can not be used at the same level since there exist no study showing it systematically, and showing the clear effect on nucleus orientation. Furthermore, if this spontaneous nucleation dominates, then there should be no orientation relation between nucleus and parent grains, while you observe one here. And please correct the fact that Falus et al. 2011 only mention rotation recrystallization and not at all spontaneous nucleation.

Please refer to previous replies

R1.17: p 18 line 32: please correct "observations" into "interpretations" since Craw et al 2018 do not show more proof than you of GBS, but use, as you do, GBS to interpret their observations...

Corrected.

R1.18: p 19 line 9-11: please be careful with the interpretation of a "hidden grain size sensitivity". I suspect that this is mainly because data from non stationary flow are used to extract parameters from a law including a grain size sensitivity devoted to a stationary state, see my comment about your figure R1.5. Therefore this is not "hidden", this is just not applicable...

We have removed such statement in the modified manuscript. Modelling work on ice mechanical behaviour will be presented in a separate paper.

R1.19: p 19 line 12: replace "spontaneous nucleation" by "nucleation by subgrain rotation".

We have replaced references to "spontaneous nucleation" with "nucleation of grains in random orientation". As discussed in previous responses, nucleation by subgrain rotation recrystallisation alone is not consistent with high-angle boundary misorientation axis data.

R1.20 - p19 line 21: the assertion (1) is incorrect, or not clearly stated... You might mean "softening owing to the reduction of stored strain energy by nucleation and grain boundary migration (or recrystallization processes)" (not "defects", because we don't know which defect you are talking about). This softening has been documented for ages by people studying recrystallization... So please cite Humphreys and Haterly 1996 for a review (or maybe Derby and Ashby 1987), and for ice, maybe Duval 1979, or maybe also Weertman 1983 ?

We have modified the statement (in section 4.2) in accordance with the reviewer's suggestion.

R1.21: p 19 line 27-28: again, the statement is wrong. The balance is between accumulated stored strain energy through dislocation (hardening) and recrystallization mechanisms that reduce this stored energy (both nucleation and GBM, recovery processes)... And again, Montagnat et al. or Sakai et al. are not the one showing that, it had been demonstrated by the whole recrystallization community for a long time!

We have modified this discussion (in section 4.2) in accordance with the reviewer's suggestion and have cited some of the older references.

R1.22: p 20 line 9: same mistake again! Not at all the balance between "GBM and nucleation"! Both processes are the softening processes associated with recrystallization... So it is about a balance between softening and hardening processes (that is indeed not balanced here since your experiments still are in the softening part).

We have modified the statement in (section 4.2) in accordance with the reviewer's comment

R1.23: p 21 line 6 "we interpret that the of"... something is missing

Oops: We interpret that the open c-axis cone develops because strain-induced GBM favours the growth of grains in easy slip orientations. Text corrected in section 5.

R1.24: conclusion point 5: reference to "spontaneous" nucleation should be replaced, here, by the mention of nucleation by rotation recrystallization, as detailed in my comments before. Or you could keep it, but as a 3rd and very hypothetic mechanism.

We have replaced references from "spontaneous nucleation" with "nucleation of grains in random orientation". Again, as discussed in previous responses nucleation by subgrain rotation recrystallisation alone is not consistent with high-angle boundary misorientation axis data.

11

List 1: Papers on rock deformation that infer GBS *(last 5 years only.)*

References that make interpretations of grain boundary sliding in rocks (natural and experimental) or use GBS as part of microstructural modelling framework not from the Otago/Liverpool or UPenn research groups. People we have worked with (and published with) highlighted in yellow. Last 5 years only.

Bollinger, C., Marquardt, K., and Ferreira, F., 2019, Intragranular plasticity vs. grain boundary sliding (GBS) in forsterite: Microstructural evidence at high pressures (3.5-5.0 GPa): American Mineralogist, v. 104, no. 2, p. 220-231.

Cao, Y., Jung, H., and Song, S. G., 2017, Olivine fabrics and tectonic evolution of fore-arc mantles: A natural perspective from the Songshugou dunite and harzburgite in the Qinling orogenic belt, central China: Geochemistry Geophysics Geosystems, v. 18, no. 3, p. 907-934.

Ceccato, A., Menegon, L., Pennacchioni, G., and Morales, L. F. G., 2018, Myrmekite and strain weakening in granitoid mylonites: Solid Earth, v. 9, no. 6, p. 1399-1419.

Chatzaras, V., Kruckenberg, S. C., Cohen, S. M., Medaris, L. G., Withers, A. C., and Bagley, B., 2016, Axial-type olivine crystallographic preferred orientations: The effect of strain geometry on mantle texture: Journal of Geophysical Research-Solid Earth, v. 121, no. 7, p. 4895-4922.

Cobden, L., Trampert, J., and Fichtner, A., 2018, Insights on Upper Mantle Melting, Rheology, and Anelastic Behavior From Seismic Shear Wave Tomography: Geochemistry Geophysics Geosystems, v. 19, no. 10, p. 3892-3916.

Czaplinska, D., Piazolo, S., and Zibra, I., 2015, The influence of phase and grain size distribution on the dynamics of strain localization in polymineralic rocks: Journal of Structural Geology, v. 72, p. 15-32.

De Paola, N., Holdsworth, R. E., Viti, C., Collettini, C., and Bullock, R., 2015, Can grain size sensitive flow lubricate faults during the initial stages of earthquake propagation?: Earth and Planetary Science Letters, v. 431, p. 48-58.

Faul, U., and Jackson, I., 2015, Transient Creep and Strain Energy Dissipation: An Experimental Perspective, *in* Jeanloz, R., and Freeman, K. H., eds., Annual Review of Earth and Planetary Sciences, Vol 43, Volume 43, p. 541-569.

Finch, M. A., Weinberg, R. F., and Hunter, N. J. R., 2016, Water loss and the origin of thick ultramylonites: Geology, v. 44, no. 8, p. 599-602.

Gardner, R., Piazolo, S., Evans, L., and Daczko, N., 2017, Patterns of strain localization in heterogeneous, polycrystalline rocks-a numerical perspective: Earth and Planetary Science Letters, v. 463, p. 253-265.

Gardner, R. L., Piazolo, S., Daczko, N. R., and Trimby, P., 2020, Microstructures reveal multistage melt present strain localisation in mid-ocean gabbros: Lithos, v. 366.

Gasc, J., Demouchy, S., Barou, F., Koizumi, S., and Cordier, P., 2019, Creep mechanisms in the lithospheric mantle inferred from deformation of iron-free forsterite aggregates at 900-1200 degrees C: Tectonophysics, v. 761, p. 16-30.

Gilgannon, J., Fusseis, F., Menegon, L., Regenauer-Lieb, K., and Buckman, J., 2017, Hierarchical creep cavity formation in an ultramylonite and implications for phase mixing: Solid Earth, v. 8, no. 6, p. 1193-1209.

Giuntoli, F., Brovarone, A. V., and Menegon, L., 2020, Feedback between high-pressure genesis of abiotic methane and strain localization in subducted carbonate rocks: Scientific Reports, v. 10, no. 1.

Goncalves, P., Poilvet, J. C., Oliot, E., Trap, P., and Marquer, D., 2016, How does shear zone nucleate? An example from the Suretta nappe (Swiss Eastern Alps): Journal of Structural Geology, v. 86, p. 166-180.

Graziani, R., Larson, K. P., and Soret, M., 2020, The effect of hydrous mineral content on competitive strain localization mechanisms in felsic granulites: Journal of Structural Geology, v. 134.

Hansen, L. N., Conrad, C. P., Boneh, Y., Skemer, P., Warren, J. M., and Kohlstedt, D. L., 2016a, Viscous anisotropy of textured olivine aggregates: 2. Micromechanical model: Journal of Geophysical Research-Solid Earth, v. 121, no. 10, p. 7137-7160.

Hansen, L. N., Warren, J. M., Zimmerman, M. E., and Kohlstedt, D. L., 2016b, Viscous anisotropy of textured olivine aggregates, Part 1: Measurement of the magnitude and evolution of anisotropy: Earth and Planetary Science Letters, v. 445, p. 92-103.

Karato, S. I., Olugboji, T., and Park, J., 2015, Mechanisms and geologic significance of the mid-lithosphere discontinuity in the continents: Nature Geoscience, v. 8, no. 7, p. 509-514.

Keppler, R., Stipp, M., Behrmann, J. H., Ullemeyer, K., and Heidelbach, F., 2016, Deformation inside a paleosubduction channel - Insights from microstructures and crystallographic preferred orientations of eclogites and metasediments from the Tauern Window, Austria: Journal of Structural Geology, v. 82, p. 60-79.

Linckens, J., Zulauf, G., and Hammer, J., 2016, Experimental deformation of coarse-grained rock salt to high strain: Journal of Geophysical Research-Solid Earth, v. 121, no. 8, p. 6150-6171.

Liu, S. R., Zhang, J. J., Qi, G. W., and Wang, M., 2016, Ductile deformation and its geological implications for retrograded eclogites from the Hongqiyingzi Complex in Chicheng, northern Hebei, China: Science China-Earth Sciences, v. 59, no. 8, p. 1610-1621.

Lopez-Sanchez, M. A., and Llana-Funez, S., 2018, A cavitation-seal mechanism for ultramylonite formation in quartzofeldspathic rocks within the semi-brittle field (Vivero fault, NW Spain): Tectonophysics, v. 745, p. 132-153.

Maierova, P., Lexa, O., Jerabek, P., Schulmann, K., and Franek, J., 2017, Computational study of deformation mechanisms and grain size evolution in granulites - Implications for the rheology of the lower crust: Earth and Planetary Science Letters, v. 466, p. 91-102.

Mansard, N., Raimbourg, H., Augier, R., Precigout, J., and Le Breton, N., 2018, Large-scale strain localization induced by phase nucleation in mid-crustal granitoids of the south Armorican massif: Tectonophysics, v. 745, p. 46-65.

Marti, S., Stunitz, H., Heilbronner, R., Plumper, O., and Drury, M., 2017, Experimental investigation of the brittle-viscous transition in mafic rocks - Interplay between fracturing, reaction, and viscous deformation: Journal of Structural Geology, v. 105, p. 62-79.

Marti, S., Stunitz, H., Heilbronner, R., Plumper, O., and Kilian, R., 2018, Syn-kinematic hydration reactions, grain size reduction, and dissolution-precipitation creep in experimentally deformed plagioclase-pyroxene mixtures: Solid Earth, v. 9, no. 4, p. 985-1009.

Maruyama, G., and Hiraga, T., 2017a, Grain- to multiple-grain-scale deformation processes during diffusion creep of forsterite plus diopside aggregate: 1. Direct observations: Journal of Geophysical Research-Solid Earth, v. 122, no. 8, p. 5890-5915.

Maruyama, G., and Hiraga, T, 2017b, Grain- to multiple-grain-scale deformation processes during diffusion creep of forsterite plus diopside aggregate: 2. Grain boundary sliding-induced grain rotation and its role in crystallographic preferred orientation in rocks: Journal of Geophysical Research-Solid Earth, v. 122, no. 8, p. 5916-5934.

Menegon, L., Fusseis, F., Stunitz, H., and Xiao, X. H., 2015, Creep cavitation bands control porosity and fluid flow in lower crustal shear zones: Geology, v. 43, no. 3, p. 227-230.

Miranda, E. A., Hirth, G., and John, B. E., 2016, Microstructural evidence for the transition from dislocation creep to dislocation-accommodated grain boundary sliding in naturally deformed plagioclase: Journal of Structural Geology, v. 92, p. 30-45.

Ohuchi, T., Kawazoe, T., Higo, Y., Funakoshi, K., Suzuki, A., Kikegawa, T., and Irifune, T., 2015, Dislocation-accommodated grain boundary sliding as the major deformation mechanism of olivine in the Earth's upper mantle: Science Advances, v. 1, no. 9.

Okudaira, T., Jerabek, P., Stunitz, H., and Fusseis, F., 2015, High-temperature fracturing and subsequent grain-size-sensitive creep in lower crustal gabbros: Evidence for coseismic loading followed by creep during decaying stress in the lower crust?: Journal of Geophysical Research-Solid Earth, v. 120, no. 5, p. 3119-3141.

Papa, S., Pennacchioni, G., Menegon, L., and Thielmann, M., 2020, High-stress creep preceding coseismic rupturing in amphibolite-facies ultramylonites: Earth and Planetary Science Letters, v. 541.

Papeschi, S., Musumeci, G., Massonne, H. J., Bartoli, O., and Cesare, B., 2019, Partial melting and strain localization in metapelites at very low-pressure conditions: The northern Apennines magmatic arc on the Island of Elba, Italy: Lithos, v. 350.

Park, M., and Jung, H., 2017, Microstructural evolution of the Yugu peridotites in the Gyeonggi Massif, Korea: Implications for olivine fabric transition in mantle shear zones: Tectonophysics, v. 709, p. 55-68.

Platt, J. P., 2015, Rheology of two-phase systems: A microphysical and observational approach: Journal of Structural Geology, v. 77, p. 213-227.

Precigout, J., and Stunitz, H., 2016, Evidence of phase nucleation during olivine diffusion creep: A new perspective for mantle strain localisation: Earth and Planetary Science Letters, v. 455, p. 94-105.

Quintanilla-Terminel, A., Zimmerman, M. E., Evans, B., and Kohlstedt, D. L., 2017, Microscale and nanoscale strain mapping techniques applied to creep of rocks: Solid Earth, v. 8, no. 4, p. 751-765.

Rogowitz, A., White, J. C., and Grasemann, B., 2016, Strain localization in ultramylonitic marbles by simultaneous activation of dislocation motion and grain boundary sliding (Syros, Greece): Solid Earth, v. 7, no. 2, p. 355-366.

Sorensen, B. E., Grant, T., Ryan, E. J., and Larsen, R. B., 2019, In situ evidence of earthquakes near the crust mantle boundary initiated by mantle CO2 fluxing and reaction-driven strain softening: Earth and Planetary Science Letters, v. 524.

Soret, M., Agard, P., Ildefonse, B., Dubacq, B., Prigent, C., and Rosenberg, C., 2019, Deformation mechanisms in mafic amphibolites and granulites: record from the Semail metamorphic sole during subduction infancy: Solid Earth, v. 10, no. 5, p. 1733-1755.

Spruzeniece, L., and Piazolo, S., 2015, Strain localization in brittle-ductile shear zones: fluid-abundant vs. fluid-limited conditions (an example from Wyangala area, Australia): Solid Earth, v. 6, no. 3, p. 881-901.

Stewart, C. A., and Miranda, E. A., 2017, The Rheological Evolution of Brittle-Ductile Transition Rocks During the Earthquake Cycle: Evidence for a Ductile Precursor to Pseudotachylyte in an Extensional Fault System, South Mountains, Arizona: Journal of Geophysical Research-Solid Earth, v. 122, no. 12, p. 10643-10665.

Sullivan, W. A., and Monz, M. E., 2016, Rheologic evolution of low-grade metasedimentary rocks and granite across a large strike-slip fault zone: A case study of the Kellyland fault zone, Maine, USA: Journal of Structural Geology, v. 86, p. 13-31.

Tasaka, M., Zimmerman, M. E., and Kohlstedt, D. L., 2017, Rheological Weakening of Olivine plus Orthopyroxene Aggregates Due to Phase Mixing: 1. Mechanical Behavior: Journal of Geophysical Research-Solid Earth, v. 122, no. 10, p. 7584-7596.

Thielmann, M., 2018, Grain size assisted thermal runaway as a nucleation mechanism for continental mantle earthquakes: Impact of complex rheologies: Tectonophysics, v. 746, p. 611-623.

Verberne, B. A., Chen, J. Y., Niemeijer, A. R., de Bresser, J. H. P., Pennock, G. M., Drury, M. R., and Spiers, C. J., 2017, Microscale cavitation as a mechanism for nucleating earthquakes at the base of the seismogenic zone: Nature Communications, v. 8.

Wiesman, H. S., Zimmerman, M. E., and Kohlstedt, D. L., 2018, Laboratory investigation of mechanisms for phase mixing in olivine plus ferropericlase aggregates: Philosophical Transactions of the Royal Society a-Mathematical Physical and Engineering Sciences, v. 376, no. 2132.

Yao, Z. S., Qin, K. Z., Wang, Q., and Xue, S. C., 2019, Weak B-Type Olivine Fabric Induced by Fast Compaction of Crystal Mush in a Crustal Magma Reservoir: Journal of Geophysical Research-Solid Earth, v. 124, no. 4, p. 3530-3556.

Yao, Z. S., Qin, K. Z., and Xue, S. C., 2017, Kinetic processes for plastic deformation of olivine in the Poyi ultramafic intrusion, NW China: Insights from the textural analysis of a similar to 1700 m fully cored succession: Lithos, v. 284, p. 462-476.

Zavada, P., Desbois, G., Urai, J. L., Schulmann, K., Rahmati, M., Lexa, O., and Wollenberg, U., 2015, Impact of solid second phases on deformation mechanisms of naturally deformed salt rocks (Kuh-e-Namak, Dashti, Iran) and rheological stratification of the Hormuz Salt Formation: Journal of Structural Geology, v. 74, p. 117-144.

Zhao, N. L., Hirth, G., Cooper, R. F., Kruckenberg, S. C., and Cukjati, J., 2019, Low viscosity of mantle rocks linked to phase boundary sliding: Earth and Planetary Science Letters, v. 517, p. 83-94.

List 2: Papers on ice deformation that recognise GBS as a potential process in ice deformation

GBS inferred from mechanical data
GBS observation in v. course individual GBs (e.g. columnar)inc X-ray and TEM studies of individual boundaries
GBS used to explain geophysical phenomena (planetary in particular)
GBS inferred from microstructures
GBS inferred from microstructure and mechanics
GBS inferred from observations in natural systems
GBS used in modelling

BOLD: not Otago/ UPenn or related research

Barr, A. C., and Pappalardo, R. T., 2005, Onset of convection in the icy Galilean satellites: Influence of rheology: Journal of Geophysical Research-Planets, v. 110, no. E12.

Barnes, P., Tabor, D., and Walker, J. C. F., 1971, Friction and creep of polycrystalline ice: Proceedings of the Royal Society of London Series a-Mathematical and Physical Sciences, v. 324, no. 1557, p. 127-&.

Caswell, T. E., Cooper, R. F., and Goldsby, D. L., 2015, The constant-hardness creep compliance of polycrystalline ice: Geophysical Research Letters, v. 42, no. 15, p. 6261-6268.

Craw, L., Qi, C., Prior, D. J., Goldsby, D. L., and Kim, D., 2018, Mechanics and microstructure of deformed natural anisotropic ice: Journal of Structural Geology, v. 115, p. 152-166.

Cuffey, K. M., Conway, H., Gades, A., Hallet, B., Raymond, C. F., and Whitlow, S., 2000, Deformation properties of subfreezing glacier ice: Role of crystal size, chemical impurities, and rock particles inferred from in situ measurements: Journal of Geophysical Research-Solid Earth, v. 105, no. B12, p. 27895-27915.

Durham, W. B., Prieto-Ballesteros, O., Goldsby, D. L., and Kargel, J. S., 2010, Rheological and Thermal Properties of Icy Materials: Space Science Reviews, v. 153, no. 1-4, p. 273-298.

Duval, P.: Grain Growth and Mechanical Behaviour of Polar Ice, Annals of Glaciology, 6, 79–82, doi:10.3189/1985AoG6-1-79-82, 1985.

Elvin, A. A., and Sunder, S. S., 1996, Microcracking due to grain boundary sliding in polycrystalline ice under uniaxial compression: Acta Materialia, v. 44, no. 1, p. 43-56.

Faria, S. H., Weikusat, I., and Azuma, N., 2014, The microstructure of polar ice. Part II: State of the art: Journal of Structural Geology, v. 61, p. 21-49.

Freeman, J., Moresi, L., and May, D. A., 2006, Thermal convection with a water ice I rheology: Implications for icy satellite evolution: Icarus, v. 180, no. 1, p. 251-264.

Freitag, J., Kipfstuhl, S., and Faria, S. H., 2008, The connectivity of crystallite agglomerates in low-density firn at Kohnen station, Dronning Maud Land, Antarctica, *in* Schneebeli, M., ed., Annals of Glaciology, Vol 49, 2008, Volume 49, p. 114-+.

Goldsby, D. L., 2006, Superplastic Flow of Ice Relevant to Glacier and Ice-Sheet Mechanics, *in* Knight, P. G., ed., Glacier Science and Environmental Change: Oxford, Blackwell, p. 308-314.

Goldsby, D. L., and Kohlstedt, D. L., 1997, Grain boundary sliding in fine-grained Ice I: Scripta Materialia, v. 37, no. 9, p. 1399-1406.

Goldsby, D. L., and Kohlstedt, D. L., 2001, Superplastic deformation of ice: Experimental observations: Journal of Geophysical Research-Solid Earth, v. 106, no. B6, p. 11017-11030.

Golding, N., Durham, W. B., Prior, D. J., and Stern, L. A., 2020, Plastic Faulting in Ice: Journal of Geophysical Research: Solid Earth, v. 125, no. 5, p. e2019JB018749.

Han, L. J., and Showman, A. P., 2011, Coupled convection and tidal dissipation in Europa's ice shell using non-Newtonian grain-size-sensitive (GSS) creep rheology: Icarus, v. 212, no. 1, p. 262-267.

Hawley, R. L., and Morris, E. M., 2006, Borehole optical stratigraphy and neutron-scattering density measurements at Summit, Greenland: Journal of Glaciology, v. 52, no. 179, p. 491-496.

Hondoh, T., and Higashi, A., 1983, Generation and absorption of dislocations at large-angle grain-boundaries in deformed ice crystals: Journal of Physical Chemistry, v. 87, no. 21, p. 4044-4050.

Ignat, M., and Frost, H. J., 1987, Grain-boundary sliding in ice: Journal De Physique, v. 48, no. C-1, p. 189-195.

Iliescu, D., Murdza, A., Schulson, E. M., and Renshaw, C. E., 2017, Strengthening ice through cyclic loading: Journal of Glaciology, v. 63, no. 240, p. 663-669.

Kuiper, E. J. N., de Bresser, J. H. P., Drury, M. R., Eichler, J., Pennock, G. M., and Weikusat, I., 2020a, Using a composite flow law to model deformation in the NEEM deep ice core, Greenland – Part 2: The role of grain size and premelting on ice deformation at high homologous temperature: The Cryosphere, v. 14, no. 7, p. 2449-2467.

Kuiper, E. J. N., Weikusat, I., de Bresser, J. H. P., Jansen, D., Pennock, G. M., and Drury, M. R., 2020b, Using a composite flow law to model deformation in the NEEM deep ice core, Greenland – Part 1: The role of grain size and grain size distribution on deformation of the upper 2207 m: The Cryosphere, v. 14, no. 7, p. 2429-2448.

Liu, F. P., Baker, I., and Dudley, M., 1993, Dynamic observations of dislocation generation at grain-boundaries in ice: Philosophical Magazine a-Physics of Condensed Matter Structure Defects and Mechanical Properties, v. 67, no. 5, p. 1261-1276.

Liu, F. P., Baker, I., and Dudley, M., 1995, Dislocation-grain boundary interactions in ice crystals: Philosophical Magazine a-Physics of Condensed Matter Structure Defects and Mechanical Properties, v. 71, no. 1, p. 15-42.

Min, S., Cole, D. M., and Baker, I., 2007, Effect of fine particles on the flow behavior of polycrystalline ice - (II) anelastic behavior: Chinese Journal of Geophysics-Chinese Edition, v. 50, no. 4, p. 1156-1160.

Qi, C., Prior, D. J., Craw, L., Fan, S., Llorens, M. G., Griera, A., Negrini, M., Bons, P. D., and Goldsby, D. L., 2019, Crystallographic preferred orientations of ice deformed in direct-shear experiments at low temperatures: The Cryosphere, v. 13, no. 1, p. 351-371.

Qi, C., Stern, L. A., Pathare, A., Durham, W. B., and Goldsby, D. L., 2018, Inhibition of Grain Boundary Sliding in Fine-Grained Ice by Intergranular Particles: Implications for Planetary Ice Masses: Geophysical Research Letters, v. 45, no. 23, p. 12757-12765.

Ruiz, J., 2010, Equilibrium Convection on a Tidally Heated and Stressed Icy Shell of Europa for a Composite Water Ice Rheology: Earth Moon and Planets, v. 107, no. 2-4, p. 157-167.

Song, M., 2006, Effects of particles on the anelasticity of granular ice: Philosophical Magazine Letters, v. 86, no. 10, p. 669-672.

Song, M., Cole, D. M., and Baker, I., 2004, Initial experiments on the effects of particles at grain boundaries on the anelasticity and creep behavior of granular ice, in Jacka, J., ed., Annals of Glaciology, Vol 39, 2004, Volume 39, p. 397-401.

Song, 2006, An investigation of the effects of particles on creep of polycrystalline ice: Scripta Materialia, v. 55, no. 1, p. 91-94.

Weiss, J., and Schulson, E. M., 2000, Grain-boundary sliding and crack nucleation in ice: Philosophical Magazine a-Physics of Condensed Matter Structure Defects and Mechanical Properties, v. 80, no. 2, p. 279-300.

References cited in the responses

Adams, B. L., Wright, S. I., and Kunze, K., 1993, Orientation Imaging - the Emergence of a New Microscopy: Metallurgical Transactions A-Physical Metallurgy and Materials Science, v. 24, no. 4, p. 819-831.

Ajaja, O., 1991, Role of recovery in high temperature constant strain rate deformation: Journal of Materials Science, v. 26, no. 24, p. 6599–6605, doi:10.1007/BF02402651.

Bailey, J. E., and P. B. Hirsch, 1960, The dislocation distribution, flow stress, and stored energy in cold-worked polycrystalline silver: Philosophical Magazine, v. 5, no. 53, p. 485–497.

Beeman, M., W. B. Durham, and S. H. Kirby, 1988, Friction of ice: Journal of Geophysical Research: Solid Earth, v. 93, no. B7, p. 7625–7633, doi:10.1029/JB093iB07p07625.

Bestmann, M., and D. J. Prior, 2003, Intragranular dynamic recrystallization in naturally deformed calcite marble: diffusion accommodated grain boundary sliding as a result of subgrain rotation recrystallization: Journal of Structural Geology, v. 25, no. 10, p. 1597–1613.

Bourcier, M., M. Bornert, A. Dimanov, E. Héripré, and J. L. Raphanel, 2013, Multiscale experimental investigation of crystal plasticity and grain boundary sliding in synthetic halite using digital image correlation: Journal of Geophysical Research: Solid Earth, v. 118, no. 2, p. 511–526.

Coutinho, Y. A., Rooney, S. C. K., and Payton, E. J., 2017, Analysis of EBSD Grain Size Measurements Using Microstructure Simulations and a Customizable Pattern Matching Library for Grain Perimeter Estimation: Metallurgical and Materials Transactions a-Physical Metallurgy and Materials Science, v. 48A, no. 5, p. 2375-2395.

Drury, M., and Humphreys, F. J., 1988, Microstructural shear criteria associated with grain boundary sliding during ductile deformation: Journal of Structural Geology, v. 10, p. 83-89.

Duval, P., 1985, Grain-growth and mechanical-behavior of polar ice: Annals of Glaciology, v. 6, p. 79-82.

Faria, S. H., Weikusat, I., and Azuma, N., 2014, The microstructure of polar ice. Part II: State of the art: Journal of Structural Geology, v. 61, p. 21-49.

Falus, G., A. Tommasi, and V. Soustelle, 2011, The effect of dynamic recrystallization on olivine crystal preferred orientations in mantle xenoliths deformed under varied stress conditions: Journal of Structural Geology, v. 33, no. 11, p. 1528–1540.

Gomez-Rivas, E., A. Griera, M. G. Llorens, P. D. Bons, R. A. Lebensohn, and S. Piazolo, 2017, Subgrain rotation recrystallization during shearing: Insights from full-field numerical simulations of halite polycrystals: Journal of Geophysical Research: Solid Earth, v. 122, no. 11, p. 8810–8827.

Guillope, M., and J. P. Poirier, 1979, Dynamic recrystallization during creep of single‐crystalline halite: An experimental study: Journal of Geophysical Research, v. 84, no. B10, p. 5557‐5567, doi:10.1029/JB084iB10p05557.

Hasegawa, M., and H. Fukutomi, 2002, Microstructural Study on Dynamic Recrystallization and Texture Formation in Pure Nickel: Materials Transactions, v. 43, no. 5, p. 1183–1190.

Hasegawa, M., M. Yamamoto, and H. Fukutomi, 2003, Formation mechanism of texture during dynamic recrystallization in γ-TiAl, nickel and copper examined by microstructure observation and grain boundary analysis based on local orientation measurements: Acta Materialia, v. 51, no. 13, p. 3939–3950.

Humphreys, F. J., and Hatherley, M., 1996, Recrystallization and Related Annealing Phenomena, Elsevier Science.

Humphreys, F. J., 2001, Review - Grain and subgrain characterisation by electron backscatter diffraction: Journal of Materials Science, v. 36, no. 16, p. 3833-3854.

Humphreys, F. J., 2004, Reconstruction of grains and subgrains from electron backscatter diffraction maps: Journal of Microscopy-Oxford, v. 213, p. 247-256.

McCarthy, C., H. Savage, and M. Nettles, 2017, Temperature dependence of ice-on-rock friction at realistic glacier conditions: Philosophical Transactions of the Royal Society A: Mathematical, Physical and Engineering Sciences, v. 375, no. 2086, p. 20150348–20150348.

Poirier, J. P., and A. Nicolas, 1975, Deformation-Induced Recrystallization Due to Progressive Misorientation of Subgrains, with Special Reference to Mantle Peridotites: The Journal of Geology, v. 83, no. 6, p. 707–720.

Ree, J. H., 1994, Grain-Boundary Sliding and Development of Grain-Boundary Openings in Experimentally Deformed Octachloropropane: Journal of Structural Geology, v. 16, no. 3, p. 403-418.

Rollett, A. D., Rohrer, G. S., and Humphreys, F. J., 2017, Recrystallization and Related Annealing Phenomena, Elsevier Science.

Signorelli, J., and Tommasi, A., 2015, Modeling the effect of subgrain rotation recrystallization on the evolution of olivine crystal preferred orientations in simple shear: Earth and Planetary Science Letters, v. 430, p. 356-366.

Sintay, S., Groeber, M. A., and Rollett, A. D., 2009, 3D Reconstruction of Grains, in Schwartz, A. J., Kumar, M., Adams, B. L., and Field, D. P., eds., Electron Backscatter Diffraction in Materials Science.

Sundberg, M., and R. F. Cooper, 2008, Crystallographic preferred orientation produced by diffusional creep of harzburgite: Effects of chemical interactions among phases during plastic flow: Journal of Geophysical Research, v. 113, no. B12, p. 498–16.

Trimby, P. W., D. J. Prior, and J. Wheeler, 1998, Grain boundary hierarchy development in a quartz mylonite : Journal of Structural Geology, v. 20, no. 7, p. 917–935.

White, S., 1973, Syntectonic Recrystallization and Texture Development in Quartz: Nature, v. 244, no. 5414, p. 276-278.

Response to Reviewer 2

We thank Reviewer 2 for his thoughtful and helpful review of our paper for a second time. Reviewers comments are in blue type. <mark style="background-color:#00ff00">Highlight:</mark> new text in the manuscript highlighted in the same colour.

Grain boundary sliding (GBS)

The main reviewer concern is still why we include GBS as an interpretation. The reviewer encourages us to further explore the effect of complex dislocation processes that might leave similar signals in microstructural or mechanical data as GBS. The development of subgrain boundaries is the manifestation of dislocation activities. Subgrain rotation recrystallization, through which low-angle subgrain boundaries comprised of arrays of dislocations can be transformed into high-angle grain boundaries, is interpreted as a dominant dynamic recrystallization process in this study. Therefore, we tested the role of subgrain rotation recrystallization on the weakening of CPO within a small grain population using misorientation data. These data were added after the first review. The misorientation data were clearly not used or discussed effectively in our last revision of the manuscript. In this newly modified manuscript, these misorientation data are more extensively discussed. It is the misorientation axis data that push us to maintain inclusion of GBS as a possible deformation mechanism. We discuss in detail below why the misorientation data are key to our interpretation.

The accepted understanding of subgrain rotation recrystallisation is that immediately upon nucleation of a new grain, the nucleus should have an orientation relative to the parent that reflects the dislocation structure of the final subgrain boundary segment at the moment it becomes a grain boundary. This is implicit in the first descriptions of the subgrain rotation recrystallisation (Poirier and Guillope, 1979; Poirier and Nicolas, 1975), is built into numerical simulations of the process (Gomez-Rivas et al., 2017; Signorelli and Tommasi, 2015) and is stated in all editions of John Humphrey's textbook (Humphreys and Hatherley, 1996; Rollett et al., 2017): "The orientation of the nucleus is present in the deformed structure. There is no evidence that new orientations are formed during or after nucleation, except by twinning" (from section 6.63, 7.63 or 7.62 depending on the edition).

The rotation recrystallisation model, at least in part, was erected on the basis of misorientation data, although such data were very difficult to collect at the time (Poirier and Guillope, 1979; Poirier and Nicolas, 1975; White, 1973). EBSD has made acquisition of such data much easier. One of the authors (Prior) was involved in one of the first more extensive EBSD investigations (Bestmann and Prior, 2003) of microstructures that would conventionally be explained by recovery, subgrain rotation and subgrain rotation recrystallisation. In this study subgrains and recrystallised grains of approximately the same size are developed in a shear zone within a large crystal (the parent). Low-angle boundaries surrounding subgrains have misorientation axes in rational crystallographic orientations as would be expected for subgrain rotation. High-angle grain boundaries, surrounding recrystallised grains, have misorientation axes that are randomly oriented within the crystal, inconsistent with the operation of subgrain rotation recrystallisation alone. Bestmann and Prior (2003) chose to explain these observations by allowing the newly formed nuclei to change orientation by sliding on grain boundaries. Comparable observations have been made in many dynamically recrystallised rocks (see citations of Bestmann and Prior (2003) and the reference list later on) and many have been interpreted in the same way.

In our paper, the ice misorientation axes for low- and high-angle boundaries have the same general pattern as that identified by Bestmann and Prior (2003). Low-angle boundaries have misorientation axes that are oriented tightly in the basal plane, consistent with these boundaries comprising arrays of dislocations (primarily basal dislocations) that have developed by recovery and subgrain rotation. High-angle boundaries, on the other hand, do not have misorientation axes oriented in the basal plane, nor in any other preferred crystallographic orientation. This relationship still holds when the data are restricted to the high-angle boundaries between central large grains (parents?) and surrounding small grains in the "core and mantle" structures of the lower-temperature experiments. Explaining the misorientation data requires either a different nucleation mechanism (i.e. not rotation recrystallisation) or an additional process to change the orientation of grains during or after nucleation. The common interpretation of comparable data in the rock deformation literature (not just our group) is that GBS changes the orientation of grains after nucleation. Thus, we choose to keep this as our preferred interpretation.

We continue to emphasise that GBS is just one interpretation and we present other possibilities that can explain the same observations. We feel it is important to include the GBS interpretation so that future generations of scientists can test it's validity.

Section two: point-by-point reply to comments

R2.1: Page 19, lines 5-18. I don't like the discussion on GBS which I find extremely restrictive (less than the first version of the paper but still). Apparently the authors want to prove that if there is a grain size sensitivity of the mechanical behaviour (weakening) then it must come from GBS. This is without remembering that plasticity essentially comes from dislocation slip, and that dislocations interact with other dislocations, with grain boundaries, with the internal stress field, can annihilate or climb or be nucleated, etc. leading to many possible size effects. One could for example rewrite line 9-10 "The grain size sensitivity is hidden in the flow stress data as grain size becomes controlled by the flow stress" by "The dislocation processes are hidden in the flow stress data as dislocation motion is controlled by the flow stress". But there is unfortunately no mention of possible complex dislocation processes in the paper, that are well known to be size dependent (in a complex way, the literature is abundant !). Size effects due to strain-gradient plasticity could also be invoked (e.g. work by Geers, Forest, Fleck, etc). Line 14, the sentence "Without GBS another explanation is needed for the grain size sensitivity" require a more open discussion based on all other possible weakening mechanisms. Concerning that point, the response letter cannot be considered as satisfactory. Page 27, concerning the (inverse) Hall-Petch effect, the authors write: "Some recent work relates GBS associated with the inverse Hall-Petch relationship with amorphization of the grain boundaries (Guo et al., 2018) and a molecular dynamics modelling study of ice (Cao et al., 2018) generates an inverse Hall-Petch relationship that involves a combination of GBS, grain rotation, amorphization and recrystallization, phase transformation, and dislocation nucleation in both bicrystals and polycrystals. ». BUT: Guo's paper is on nanocrystalline superhard materials (hardness similar than diamond), and Cao's paper is a MD computational study on 40nm polycrystalline ice with flow stress around 600MPa ! Of course GBS can occurs in some materials but these two references on nm grains have nothing to do with the hundred-microns ice grains considered here. This is not to say that GBS is not active in ice, but the authors should be convincing by using a correct argumentation. That GBS occurs in some nanometric superhard material does not guarantee that it also occurs in ice.

We thank the reviewer for these thoughtful comments. The discussion of the role of grain size-sensitive processes (including GBS) in mechanical evolution is has been substantially reduced. Because this paper is focused on the microstructural and CPO evolution of deformed ice samples, a full discussion of all issues related to grain size-sensitivity, which are quite complex as pointed out by the reviewer, is beyond the scope of this paper. We have another manuscript in preparation wherein grain size-sensitivity is the central topic and we consider these helpful discussion points in writing that paper.

R2.2: Page 16 line 16 : similarly, strange to put reference to Elati et al. here to show that GBS happens in some fine grain structure materials. This reference is on a High Entropy Alloy, which may differ significantly from ice deformation (if not please justify). There are other materials in which GBS is active without having to go to fine grains, such as Salt (see papers by Bornert, Dimanov and Bourcier).

We have removed the Eleti et al reference in the modified manuscript.

R2.3: Page 8 line 10 : as already indicated in my first review, the distribution shown in figure 4 can really not be described as a "bimodal" one ! Same line 17 (bimodal grain size). Please modify.

Thanks to the reviewer for pointing out this mistake. We have modified the statement in section <mark>3.3.2</mark> in accordance with the reviewer's comment.

R2.4: Page 15 line 4 : I don't know whether this is a standard treatment in the glaciology or mineral physics community, but the identification of an activation energy for the "flow stress" (or tertiary creep in "constant load experiments") is not accurate, as the sample microstructures vary between specimens.

The identification of an activation energy for the "flow stress" is a common treatment in the rock deformation community (e.g. Hirth et al., 2001; Hirth, 2002; Renner and Evans, 2002; Karato, 2008; Hansen et al, 2012) and has been applied to an ice flow law (Durham et al, 1983). It can be considered as empirical. Arrhenius plots with large data sets often produce good straight-line fits to the data (e.g., Durham et al., 1983).

R2.5: Page 2 line 25 : "displacement rate" instead of "displacement"

Corrected.

References

Bestmann, M., and Prior, D. J., 2003, Intragranular dynamic recrystallization in naturally deformed calcite marble: diffusion accommodated grain boundary sliding as a result of subgrain rotation recrystallization: Journal of Structural Geology, v. 25, no. 10, p. 1597-1613.

Durham, W. B., Heard, H. C., and Kirby, S. H., 1983, Experimental deformation of polycrystalline h2o ice at high-pressure and low-temperature - preliminary-results: Journal of Geophysical Research, v. 88, p. B377-B392.

Gomez-Rivas, E., Griera, A., Llorens, M. G., Bons, P. D., Lebensohn, R. A., and Piazolo, S., 2017, Subgrain Rotation Recrystallization During Shearing: Insights From Full-Field Numerical Simulations of Halite Polycrystals: Journal of Geophysical Research-Solid Earth, v. 122, no. 11, p. 8810-8827.

Hansen, L. N., Zimmerman, M. E., Dillman, A. M., and Kohlstedt, D. L., 2012, Strain localization in olivine aggregates at high temperature: A laboratory comparison of constant-strain-rate and constant-stress boundary conditions: Earth And Planetary Science Letters, v. 333, p. 134-145.

Hirth, G., 2002, Laboratory constraints on the rheology of the upper mantle, Plastic Deformation of Minerals and Rocks, Volume 51, p. 97-120.

Hirth, G., Teyssier, C., and Dunlap, W. J., 2001, An evaluation of quartzite flow laws based on comparisons between experimentally and naturally deformed rocks: International Journal of Earth Sciences, v. 90, no. 1, p. 77-87.

Humphreys, F. J., and Hatherley, M., 1996, Recrystallization and Related Annealing Phenomena, Elsevier Science.

Karato, S., 2008, Deformation of Earth Materials, Cambridge, Cambridge University Press.

Poirier, J. P., and Guillope, M., 1979, Deformation Induced Recrystallization of Minerals: Bulletin de Mineralogie, v. 102, no. 2-3, p. 67-74.

Poirier, J. P., and Nicolas, A., 1975, Deformation-Induced Recrystallization Due to Progressive Misorientation of Subgrains, with Special Reference to Mantle Peridotites: Journal of Geology, v. 83, no. 6, p. 707-720.

Renner, J., and Evans, B., 2002, Do calcite rocks obey the power-law creep equation?, *in* DeMeer, S., Drury, M. R., DeBresser, J. H. P., and Pennock, G. M., eds., Deformation Mechanisms, Rheology and Tectonics: Current Status and Future Perspectives, Volume 200, p. 293-307.

Rollett, A. D., Rohrer, G. S., and Humphreys, F. J., 2017, Recrystallization and Related Annealing Phenomena, Elsevier Science.

Signorelli, J., and Tommasi, A., 2015, Modeling the effect of subgrain rotation recrystallization on the evolution of olivine crystal preferred orientations in simple shear: Earth and Planetary Science Letters, v. 430, p. 356-366.

White, S., 1973, Syntectonic Recrystallization and Texture Development in Quartz: Nature, v. 244, no. 5414, p. 276-278.

A list of all relevant changes made in the manuscript

Extracts from original manuscript are in blue type (**P**=Page, **L**=Line, in the original manuscript). *Extracts from our revised manuscript are in italics (**P**=Page, **L**=Line, in the revised manuscript).*

1. Modifications in section "Abstract"

1.1 Add statement:*"Nucleation during recrystallisation cannot be explained by subgrain rotation recrystallisation alone" (P2, L9)*

1.2 "Grain boundary sliding of finer grains or nucleation of those grains in random orientations ("spontaneous" nucleation) could explain the weaker CPO of the fine-grained fraction and the lack of crystallographic control on high-angle grain boundaries." **(P2, L9-11)** re-written as:
"*Grain boundary sliding of finer grains or a different nucleation mechanism that generates grains with random orientations could explain the weaker CPO of the fine-grained fraction and the lack of crystallographic control on high-angle grain boundaries." (P2, L9 –11)*

2. Modifications in section "Introduction"

2.1 Remove references of "Kuiper et al., 2019a, 2019b " *(P2, L18; P2, L18)*

2.2 Modify "displacement" **(P2, L25)** to:
"displacement rate" (P2, L25)

3. Modifications in section "Method"

3.1 Add sentence of *"This method counts all areas enclosed by boundaries ⩾ 2˚ within area enclosed by ⩾ 10˚ boundaries; no internal boundaries ⩾ 2˚ will be counted as either a subgrain or a grain (see Figure 5 in Trimby et al., 1998)." (P5, L22-24).*

3.2 "Fig. 9-11." *(P12, L14) to* "Fig. 8-10." *(P12, L18)*

3.3 "strai,n" *(P12, L27) to* "strain" *(P13, L3)*

4. Modifications in section "Results"

4.1 Modify "For samples deformed to ~3% strain, the grain size distributions are strongly skewed or possibly bimodal, with a clear main peak at finer grain sizes and a tail of coarser sizes with a broad, poorly defined secondary peak corresponding to the mean grain size of the starting material (Fig. 4(d), 5(d) and 6(d))." **(P8, L10-12)** to:
"For samples deformed to ~3% strain, the grain size distributions are strongly skewed, with a clear main peak at finer grain sizes and a tail of coarser sizes with a possible broad, poorly defined secondary peak corresponding to the mean grain size of the starting material (Fig. 4(d), 5(d) and 6(d))." (P8, L10-12)

4.2 Add figure reference of "*Fig. 11(b)*" *(P10, L14)*

4.3 Add statement of "*The interquartile range (IQR) of subgrain sizes, with upper and lower limits bounded by higher quartile and lower quartile subgrain sizes, respectively, generally decreases with an increasing strain at all temperatures (Fig. 11(b)). IQR covers a wide range of subgrain size for samples deformed at -10 °C, but it narrows as the temperature decreases (Fig. 11(b))." (P10, L17-20)*

5 Modifications in section "Discussion"

5.1 "Grain number density generally 15 increases and all measures of 2-D grain size decrease with strain (Table 3), …" **(P15, L15-16)** revised to:

"The number of grains per unit area (accounting for multiple occurrences of the same 3-D grain) generally increases and all measures of 2-D grain size decrease with strain (Table 3), ..." (**P15, L23-24**)

5.2 *Remove statement of* Lately, Eleti and others (2020) used a fiducial marker grid to show that the deformation of finer grains in the necklace structure includes a significant component of GBS." (**P16, L16-17**)

5.3 Add statements *"For all deformed samples, neighbour-pair misorientation axes at misorientation angles of 5°-10° show primary maxima lying in the basal plane (Fig. 4(g), 5(g), 6(g)). Similarly, misorientation axes of 5°-10° boundaries within the large reference grains of the "core-and-mantle" structure have primary maxima lying in the basal plane (Fig. 7(c)). These observations suggest low-angle boundaries (5°-10°) are crystallographically controlled, consistent with them being subgrain boundaries that comprise arrays of dislocations.*
The general understanding of the subgrain rotation recrystallisation process (Poirier, 1972; Poirier and Nicolas, 1975), is that a new "nucleus" forms when all of the enclosing subgrain boundaries, comprising arrays of dislocations, are transformed to grain boundaries, that have no formally defined structure (Rollett et al., 2017). In simplified terms there is a limit to the misorientation that can be sustained by an array of dislocations (related to limits of the Read-Shockley equation: Read and Shockley, 1950; Rollett et al., 2017) so at some point continued addition of dislocations to a boundary prompts the change in boundary structure. There is no mechanism understood by which the misorientation of a subgrain boundary changes when it transforms to a grain boundary. Thus, high-angle grain boundaries of nuclei generated by subgrain rotation recrystallization should have the same orientation as the subgrain that forms the nucleus and should also be crystallographically controlled (Rollett et al., 2017), if additional processes are not activated after their production.
In all deformed samples, neighbour-pair misorientation axes at misorientation angles larger than 10° have a distribution close to random (Fig. 4(g), 5(g), 6(g)), suggesting high-angle grain boundaries lack a crystallographic control. The "core-and-mantle" structures observed at lower temperatures (-20 °C and -30 °C) have misorientations axes of boundaries between small grains and their large or small neighbours that do not lie in the basal plane and have no preferred nor rational crystallographic orientation (Fig. 7(d)). High-angle grain boundaries of "small" grains lack a crystallographic control within deformed samples. Subgrain rotation recrystallisation can be considered a nucleation mechanism, but alone it cannot explain the misorientation axes of high angle boundaries. Either a different nucleation mechanism is needed or an additional process is needed to change the orientation of grains during or after nucleation. This discussion continues in the context of the CPO data in section 4.1.4." (**P16, 26 to P17, L13**)

5.4 Remove statements: *"At lower temperatures (-20 °C and -30 °C) typical "core-and-mantle" structures have small grains with orientations that are dispersed around neighbouring large grains (Fig. 7) and the misorientations of small grains with large or small neighbours lack a consistent or rational crystallographic control crystallographic control. Whole sample misorientations show that boundaries with >10° misorientation are less crystallographically-controlled than low angle boundaries."* (**P18, L21-25**)

5.5 Add statements *"Microstructural analyses suggest subgrain rotation and subgrain rotation recrystallization are dominant processes responsible for the production of "small" grains within samples deformed at both high and low temperatures (see section 4.1.2.2). Subgrain rotation and subgrain rotation recrystallization will disperse orientations away from the parent grain orientation and small grains, if representative of nuclei formed by subgrain rotation recrystallization will represent the most extreme dispersion from the parent orientation. However, subgrain rotation recrystallization alone should produce nuclei with crystallographically controlled grain boundaries linked to the parent grain orientation. As this is not the case (see section 4.1.2.2) it is difficult to explain CPO weakening by subgrain rotation recrystallization alone; additional processes should be responsible for a weaker CPO within small grains. Data from our experiments suggest such hypothesis works better for experiments at -20 and -30 °C. At -10 °C the contrast of CPO intensity between "big" and "small" grains becomes less clear, and the "core-and-mantle" structure is absent. One way to explain these data is that the modification of grain boundary topology via grain boundary migration (GBM) could be more widespread at a warmer temperature, which could obscure evidence of the additional process responsible for a weaker CPO in smaller grains. The interaction of GBS with dislocation processes and GBM is developed a little in the ice literature (Hondoh and Higashi, 1983; Liu et al, 1993; 1995; Duval, 1985; Faria et al., 2014) and experiments that show offsets of grain boundaries whilst GBM occurs (Drury and Humphreys 1988; Ree, 1994) suggest that GBS may not leave a clear signal when GBS and GBM coexist."* (**P19, L26 to P20, L7**)

5.6 Remove "Ice experiments at -10°C with two initial grain sizes, one similar to our experiments (PIL007 is one of these older experiments) and the other coarser, show significant peak stress grain size sensitivity (Fig. 3 in Qi et al., 2017), with a 2 to 3 fold increase in strain rate for a given stress. The grain size sensitivity is hidden in flow

stress data as the grain size becomes controlled by the stress (Jacka and Li, 1994; De Bresser et al, 2001) and a flow law relationship can be defined independent of the grain size (De Bresser et al, 2001)" **(P19, L7-11)**

5.7 Remove "We have greater confidence in the GBS interpretation because it is consistent with the grain size sensitivity that is observed in comparable ice deformation experiments. Without GBS another explanation is needed for the grain size sensitivity." **(P19, L13-15)**

5.8 Adjust format: **(P18, L25 to P19, L7)** now **(P20, L8 to P20, L29)**

5.7 Modify "Both hypotheses— "spontaneous" nucleation and GBS—explain a weakening of CPO in "small" grains and these two ideas are not mutually exclusive." **(P19, L12-13)** to
"The two hypotheses—GBS and nucleation of grains with random orientations—can explain a weakening of CPO in "small" grains and these two ideas are not mutually exclusive." (P20, L30-31)

5.8 Modify "(1) the softening of grains related to reduction in defect content associated with dynamic recovery and recrystallisation (Montagnat and Duval., 2000; Sakai et al., 2014)," **(P19, L21-22)** to
"(1) the softening owing to the reduction of stored strain energy by dynamic recrystallisation processes such as nucleation and grain boundary migration (Duval, 1979; Weertman, 1983; Derby and Ashby, 1987; Humphreys and Hatherley, 2008; Rollett et al 2017)," (P21, L5-7)

5.9 Modify "Weakening is classically observed during dynamic recrystallization, and it was attributed to a balance between GBM and nucleation of new grains (Montagnat and Duval., 2000; Sakai et al., 2014)." **(P19, L27-28)** to
"Weakening is classically observed during dynamic recrystallization; the mechanical evolution from peak to flow stress in constant displacement rate experiments or from secondary to tertiary creep stage in constant load experiments was attributed to a balance between processes favouring strain hardening (e.g. accumulation of stored strain energy through dislocation) and weakening (e.g. reduction of stored strain energy through dynamic recrystallisation) (Duval, 1979; Weertman, 1983; Derby and Ashby, 1987; Humphreys and Hatherley, 2008)." (P21, L13-17)

5.10 Modify "Therefore, further studies are required to quantify: (1) the contribution of nucleation and GBM to the total stress drop if the balance of GBM and nucleation is considered as the weakening mechanism; (2) The contribution of grain size insensitive, e.g. dislocation creep, and grain size 10 sensitive processes, e.g. GBS, to the total stress drop if grain size reduction is considered as the weakening mechanism." **(P20, L8-11)** to
"Therefore, further studies are required to quantify the contribution of candidate weakening (enhancement) mechanisms including (1) dynamic recrystallisation processes such as nucleation and GBM, (2) grain size reduction and the resulting contribution of GBS, (3) CPO development to the mechanical weakening observed during ice deformation." (P21, L28-31)

6 Modifications in section "Conclusions"

6.1 Modify "We interpret that the of the open c-axis cone develops because strain-induced GBM favours the growth of grains in easy slip orientations." **(P21, L6-7)** to
"We interpret that the open c-axis cone develops because strain-induced GBM favours the growth of grains in easy slip orientations." (P22, L26-27)

6.1 Modify "We identify two candidate processes; (1) grain boundary sliding causing rotation of grains without crystallographic control on the rotation axes and (2) "spontaneous" nucleation in random initial orientations." **(P21, L13-14)** to
"We identify two candidate processes; (1) grain boundary sliding causing rotation of grains without crystallographic control on the rotation axes, and (2) nucleation of grains with random orientations." (P23, L1-2)

7 Added references:

Derby, B. and Ashby, M. F.: On dynamic recrystallization, Scripta Metallurgica, 21(6), 879–884, https://doi.org/10.1016/0036-9748(87)90341-3, 1987.
Drury, M. R. and Humphreys, F. J.: Microstructural shear criteria associated with grain-boundary sliding during ductile deformation, Journal of Structural Geology, 10(1), 83–89, https://doi.org/10.1016/0191-8141(88)90130-7, 1988.

Duval, P.: Grain Growth and Mechanical Behaviour of Polar Ice, Annals of Glaciology, 6, 79–82, https://doi.org/10.3189/1985AoG6-1-79-82, 1985.

Hasegawa, M. and Fukutomi, H.: Microstructural Study on Dynamic Recrystallization and Texture Formation in Pure Nickel, Mater. Trans., 43(5), 1183–1190, https://doi.org/10.2320/matertrans.43.1183, 2002.

Hasegawa, M., Yamamoto, M. and Fukutomi, H.: Formation mechanism of texture during dynamic recrystallization in γ-TiAl, nickel and copper examined by microstructure observation and grain boundary analysis based on local orientation measurements, Acta Materialia, 51(13), 3939–3950, https://doi.org/10.1016/S1359-6454(03)00218-0, 2003.

Hondoh, T. and Higashi, A.: Generation and absorption of dislocations at large-angle grain boundaries in deformed ice crystals, The Journal of Physical Chemistry, 87(21), 4044–4050, https://doi.org/10.1021/j100244a009, 1983.

Humphreys, F. J. and Hatherly, M. (2nd Eds.): Recrystallization and related annealing phenomena, Elsevier, 2008.

Kamb, B.: Basal Zone of the West Antarctic Ice Streams and its Role in Lubrication of Their Rapid Motion, in: Antarctic Research Series, American Geophysical Union (AGU), edited by: Alley, R. B., Bindschadle, R. A., Washington, D. C., USA, 157-199, https://doi.org/10.1029/AR077p0157, 2008.

Kuiper, E.-J. N., Weikusat, I., de Bresser, J. H. P., Jansen, D., Pennock, G. M. and Drury, M. R.: Using a composite flow law to model deformation in the NEEM deep ice core, Greenland – Part 1: The role of grain size and grain size distribution on deformation of the upper 2207 m, The Cryosphere, 14(7), 2429–2448, https://doi.org/10.5194/tc-14-2429-2020, 2020.

Kuiper, E.-J. N., de Bresser, J. H. P., Drury, M. R., Eichler, J., Pennock, G. M. and Weikusat, I.: Using a composite flow law to model deformation in the NEEM deep ice core, Greenland – Part 2: The role of grain size and premelting on ice deformation at high homologous temperature, The Cryosphere, 14(7), 2449–2467, https://doi.org/10.5194/tc-14-2449-2020, 2020.

Liu, F., Baker, I. and Dudley, M.: Dynamic observations of dislocation generation at grain boundaries in ice, Philosophical Magazine A, 67(5), 1261–1276, https://doi.org/10.1080/01418619308224770, 1993.

Liu, F., Baker, I. and Dudley, M.: Dislocation-grain boundary interactions in ice crystals, Philosophical Magazine A, 71(1), 15–42, https://doi.org/10.1080/01418619508242954, 1995.

Maruyama, G. and Hiraga, T.: Grain- to multiple-grain-scale deformation processes during diffusion creep of forsterite + diopside aggregate: 1. Direct observations, Journal of Geophysical Research: Solid Earth, 122(8), 5890–5915, https://doi.org/10.1002/2017jb014254, 2017.

Poirier, J. P.: High-temperature creep of single crystalline sodium chloride, The Philosophical Magazine: A Journal of Theoretical Experimental and Applied Physics, 26(3), 701–712, https://doi.org/10.1080/14786437208230114, 1972.

Read, W. T. and Shockley, W.: Dislocation Models of Crystal Grain Boundaries, Phys. Rev., 78(3), 275–15, https://doi.org/10.1103/PhysRev.78.275, 1950.

Ree, J. H.: Grain boundary sliding and development of grain boundary openings in experimentally deformed octachloropropane, Journal of Structural Geology, 16(3), 403–418, https://doi.org/10.1016/0191-8141(94)90044-2, 1994.

Rollett, A. D., Rohrer, G. S., and Humphreys, F. J., (3rd Eds.), Recrystallization and Related Annealing Phenomena, Elsevier Science, 2017.

8 Modifications to "Tables"

8.1 Add interquartile ranges of subgrain size ($d_{q,25\%}$ and $d_{q,25\%}$) in Table 3.

8.2 Correct two data mistakes in Table 4.

9 Modifications to "Figures"

9.1 Add interquartile range of subgrain sizes in Fig. 11(b)

Temperature and strain controls on ice deformation mechanisms: insights from the microstructures of samples deformed to progressively higher strains at -10, -20 and -30 °C

Sheng Fan[1], Travis Hager[2], David J. Prior[1], Andrew J. Cross[2,3], David L. Goldsby[2], Chao Qi[4], Marianne Negrini[1], John Wheeler[5]

[1] Department of Geology, University of Otago, Dunedin, New Zealand
[2] Department of Earth and Environmental Science, University of Pennsylvania, Philadelphia, PA, USA
[3] Department of Geology and Geophysics, Woods Hole Oceanographic Institution, Woods Hole, MA, USA
[4] Key laboratory of Earth and Planetary Physics, Institute of Geology and Geophysics, Chinese Academy of Sciences, Beijing, China
[5] Department of Earth and Ocean Sciences, University of Liverpool, Liverpool, UK

Correspondence to: Sheng Fan (sheng.fan@postgrad.otago.ac.nz).

Abstract In order to better understand ice deformation mechanisms, we document the microstructural evolution of ice with increasing strain. We include data from experiments at relatively low temperatures (-20 and -30 °C), where the microstructural evolution with axial strain has never before been documented. Polycrystalline pure water ice was deformed under a constant displacement rate (strain rate $\sim 1.0 \times 10^{-5}\ s^{-1}$) to progressively higher strains ($\sim$3, 5, 8, 12 and 20%) at temperatures of -10, -20 and -30 °C. Microstructural data were generated from cryogenic electron backscattered diffraction (cryo-EBSD) analyses. All deformed samples contain sub-grain (low-angle misorientations) structures with misorientation axes that lie dominantly in the basal plane suggesting the activity of dislocation creep (glide primarily on the basal plane), recovery and subgrain rotation. Grain boundaries are lobate in all experiments suggesting the operation of strain-induced grain boundary migration (GBM). Deformed ice samples are characterised by interlocking big and small grains and are, on average, finer grained than undeformed samples. Misorientation analyses between nearby grains in 2-D EBSD maps are consistent with some 2-D grains being different limbs of the same irregular grain in the 3-D volume. The proportion of repeated (i.e. interconnected) grains is greater in the higher-temperature experiments suggesting that grains have more irregular shapes, probably because GBM is more widespread at higher temperatures. The number of grains per unit area (accounting for multiple occurrences of the same 3-D grain) is higher in deformed samples than undeformed samples, and it increases with strain, suggesting that nucleation is involved in recrystallisation. "Core-and-mantle" structures (rings of small grains surrounding big grains) occur in -20 and -30 °C experiments, suggesting that subgrain rotation recrystallization is active. At temperatures warmer than -20 °C, *c*-axes develop a crystallographic preferred orientation (CPO) characterized by a cone (i.e., small circle) around the compression axis. We suggest the *c*-axis cone forms via the selective growth of grains in easy slip orientations (i.e., ~45° to shortening direction) by GBM. The opening-angle of the *c*-axis cone decreases with strain, suggesting strain-induced GBM is balanced by grain rotation. Furthermore, the opening-angle of the *c*-axis cone decreases with temperature. At -30 °C, the *c*-axis CPO changes

from a narrow cone to a cluster, parallel to compression, with increasing strain. This closure of the *c*-axis cone is interpreted as the result of a more active grain rotation together with a less effective GBM. We suggest that lattice rotation, facilitated by intracrystalline dislocation glide on the basal plane is the dominant mechanism controlling grain rotation. Low-angle neighbour-pair misorientations, relating to subgrain boundaries, are more extensive and extend to higher misorientation angles at lower temperatures and higher strains supporting a relative increase in importance of dislocation activity. As the temperature decreases, the overall CPO intensity decreases, primarily because the CPO of small grains is weaker. High-angle grain boundaries between small grains have misorientation axes that have distributed crystallographic orientations. This implies that, in contrast to subgrain boundaries, grain boundary misorientation is not controlled by crystallography. Nucleation during recrystallisation cannot be explained by subgrain rotation recrystallisation alone. Grain boundary sliding of finer grains or a different nucleation mechanism that generates grains with random orientations could explain the weaker CPO of the fine-grained fraction and the lack of crystallographic control on high-angle grain boundaries.

1 Introduction

Glaciers and ice sheets play key roles in shaping planetary surfaces, and form important feedbacks with climate, both on Earth (Pollard, 2010; Hudleston, 2015; Kopp et al., 2017) and elsewhere in the solar system (Hartmann, 1980; Whalley and Azizi, 2003). Understanding the controls on the flow rate of terrestrial glaciers and ice sheets is crucial, as this will be a major control on future sea level change (Bindschadler et al., 2013; Dutton et al., 2015; Bamber et al., 2019). Ice core studies and field investigations suggest the temperature of ice in Antarctica and Greenland ranges between ice melting temperature and ~-30 °C (Kamb, 2008; Montagnat et al., 2014). Glacial flow is driven by gravity and facilitated by both basal sliding along the ice-bedrock interface (and/or with the shearing of subglacial till deposits) and the internal creep of ice masses. The contribution of creep deformation to the total flow rate is controlled primarily by differential stress and temperature within the ice body (Rignot et al., 2011; Hudleston, 2015). Creep experiments show a change in the mechanical behaviour as initially isotropic polycrystalline ice is deformed (Budd and Jacka, 1989; Faria et al., 2014; Hudleston, 2015). Mechanical weakening occurs during the transition from secondary creep (minimum strain rate) to tertiary creep (quasi-constant strain rate) in constant load experiments (e.g., Budd and Jacka, 1989; Montagnat et al., 2015; Hudleston, 2015; Wilson et al 2014) and from peak stress to steady-state stress in constant displacement rate experiments (e.g., Weertman, 1983; Durham et al., 1983, 2010; Vaughan et al., 2017; Qi et al., 2017). This mechanical weakening is often referred to as strain rate "enhancement" in the glaciological and ice sheet literature (Budd and Jacka, 1989; Alley, 1992; Placidi et al., 2010; Treverrow et al 2012; Budd et al., 2013). Enhancement correlates with the development of a crystallographic preferred orientation (CPO) (Jacka and Maccagnan, 1984; Vaughan et al., 2017) and also with other microstructural changes, particularly those associated with dynamic recrystallization (Duval, 1979; Duval et al., 2010; Faria et al., 2014; Montagnat et al., 2015), including grain size reduction (Craw et al., 2018; Qi et al., 2019). Understanding the deformation and recrystallization mechanisms responsible for ice microstructure and CPO development is therefore essential for quantifying how different mechanisms contribute to ice creep enhancement in nature.

2

The relative roles of intracrystalline plasticity, recrystallization and grain size sensitive mechanisms, especially at low temperatures, are not well known.

In this contribution we present microstructural analyses of samples deformed to successively higher strains through the transition from peak stress to flow stress at -10, -20 and -30 °C. These conditions were chosen so that the experiments included evolution of CPO towards a cone (small circle, centred on the compression direction) that occurs at high temperature and towards a cluster (maximum parallel to the compression direction) at low temperature. Our results include microstructural data from samples deformed to progressively higher strains at -20 and -30 °C. Such data have not been presented before, and they are important, as understanding how and why different CPOs develop as a function of temperature should give a better insight into the mechanisms that control CPO development and mechanical behaviour. Furthermore, understanding CPOs in nature requires extrapolation of laboratory results to the much lower strain rates that occur in nature. To do this effectively we need to know how CPOs evolve across as wide a range of temperatures and strain rates as is possible. In this paper our objectives are to study the influences of temperature and strain on microstructure and CPO development and to discuss implications for mechanical behaviour.

2 Methods

2.1 Sample fabrication

Dense, polycrystalline ice samples were prepared by the flood-freeze (standard ice) method (Cole, 1979; Durham et al., 1983; Stern et al., 1997) to produce samples with controlled grain size, random CPO and minimised porosity. We crushed ice cubes made from frozen Milli-Q water (ultra-pure water), into ice powders. These ice powders were then sieved at -30 °C in a chest freezer, to limit the particle sizes to between 180 and 250 μm. Particles were then packed into the bottom of lightly greased stainless-steel cylindrical moulds (inner diameter 25.4 mm) to achieve a porosity of ~40%. A perforated brass spacer was placed on top of the packed ice power and the mould was sealed with a double O-ring plug. Air was removed from pore spaces with a vacuum pump after the moulds were equilibrated at 0 °C in a water-ice bath for 40 minutes. Degassed Milli-Q water (at 0 °C) was then flooded into the pore spaces. The perforated spacer prevented ice particles from floating in the water. After flooding, the moulds were transferred to a -30 °C chest freezer and placed vertically into cylindrical holes in a polystyrene block, with the base of moulds touching a copper plate at the bottom of the freezer. This ensures that a freezing front migrates slowly upwards. After 24 hours the ice samples were gently pushed out of the moulds using an Arbor press. Both ends of the cylindrical samples were cut and polished to be flat, parallel with one another, and perpendicular to the sample's long axis, and the length of the sample was recorded (Table 1). Each sample was encapsulated in a thin-walled indium jacket (~0.38 mm wall thickness), the bottom of which had already been welded to (melted against) a stainless-steel end-cap. The top of the indium tube was then welded to a steel semi-internal force gauge, with a thermally insulating zirconia spacer placed between the force gauge and sample. The sample was kept cold in a -60 °C ethanol bath (Qi et al., 2017) during welding.

2.2 Experimental set up and process

We conducted axial compression experiments at the Ice Physics Laboratory, University of Pennsylvania. Experiments were conducted at a nitrogen gas confining pressure of ~20 ± 0.5 MPa at temperatures of -10, -20, and -30°C (±0.5°C), in a cryogenic, gas-medium apparatus (Durham et al., 1983; Heard et al., 1990). Samples were left to thermally equilibrate with the apparatus for more than 60 minutes before deformation started. Deformation experiments were performed at a constant axial displacement rate, giving an initial constant strain rate of ~1.0×10^{-5} s-1. The experiments were terminated once final axial true strains of ~3%, 5%, 8%, 12% and 20% were achieved. After deformation, the ice samples were immediately extracted from the apparatus, photographed and measured. To minimize thermal cracking, samples were progressively cooled to ~ -30, -100 and -196 °C in about 15 minutes, and thereafter stored in a liquid nitrogen dewar. Typical time between the end of the experiments and the start of cooling was between 10 and 30 minutes. Minor static recovery of the ice microstructures may happen on this timescale (Hidas et al., 2017), but significant change in CPO or grain size is unlikely.

2.3 Mechanical data processing

During each experimental run, time, displacement and load were recorded once every five to seven seconds. The axial stress was calculated from the load supported by the sample divided by the instantaneous cross-sectional area of the sample, which was calculated by assuming constant sample volume during the deformation. The sample length $L(t)$ at time t is calculated from the displacement and the initial sample length (L_0). From this we calculate the axial stretch (λ: Eq. (1)) and the true axial strain (ε: Eq. (2)) (Hobbs et al., 1976).

$$\lambda = \frac{L(t)}{L_0} \tag{1}$$

$$\varepsilon = -\ln(\lambda) \tag{2}$$

2.4 Cryo-EBSD data

The relatively recent development of cryo-EBSD (electron backscatter diffraction) technique (Iliescu et al., 2004, Obbard et al., 2006; Piazolo et al., 2008) enables measurement of full crystallographic orientations. EBSD maps provide quantitative microstructural data, with significant detail in ice samples with sizes up to about 70 mm by 40 mm (Prior et al., 2015). We prepared the ice samples and acquired the cryo-EBSD data following the procedures described by Prior and others (2015). Samples were cut in half along the cylindrical long-axis using a band saw in a -20 °C cold room and a ~5 mm slice was cut from half of the sample. One side of the slice, at a temperature of ~-30 to -50 °C, was placed against a copper ingot (70 mm by 35 mm) at ~5 °C. As soon as a bond formed between the ice sample and the ingot, the samples were placed in a polystyrene sample transfer box (~-100 °C). We acquired a polished sample surface for cryo-EBSD by hand lapping on grit paper. The samples were polished at ~-40 °C using grit sizes of 80, 240, 600, 1200 and 2400. The sample-ingot assemblies were then

transferred to the polystyrene sample transfer box and cooled to close to liquid nitrogen temperature, before they were transferred into the SEM for the collection of cryo-EBSD data.

EBSD data were acquired using a Zeiss Sigma VP FEGSEM combined with a NordlysF EBSD camera from Oxford Instruments. We used pressure cycling in the SEM chamber remove frost and create a damage-free sample surface (Prior et al., 2015). EBSD data were acquired at a stage temperature of ~-95 °C, with 5-7 Pa nitrogen gas pressure, 30kV accelerating voltage and a beam current of ~60 nA. For each ice sample, we collected a reconnaissance map with a step size of 30 µm from the whole section and a map with a step size of 5 µm, from a selected sub-area, for detailed microanalysis (mapped areas listed in Table 2). We acquired and montaged the raw EBSD data using Oxford Instruments' Aztec software. Details on the raw EBSD data have been summarized in Table 2. The angular resolution (error of crystallographic orientation measurement for each pixel) of the EBSD data is ~0.5°.

2.5 Processing of the cryo-EBSD data

Grain size, grain shape, grain boundary morphology, and CPO provide useful information for inferring ice deformation processes. We quantified these microstructural parameters (among others) from raw EBSD data using the MTEX toolbox (Bachmann et al., 2011; Mainprice et al., 2015) in MATLAB.

2.5.1 Grain size and subgrain size

Ice grains were reconstructed from the raw EBSD pixel maps with 5 µm step size using the MTEX algorithm of Bachmann and others (2011) with a grain boundary threshold of 10°. Grains with area equivalent diameters lower than 20 µm were removed from the data. No pixel interpolation was applied to the EBSD pixel map, preserving any non-indexed space. Deformed ice is often characterised by a development of subgrain boundaries where the misorientations between neighbouring pixels are lower than the misorientation angle threshold of grain boundaries (e.g. Montagnat et al., 2015; Weikusat et al., 2017). An ice grain can be separated into several subgrains by one or more subgrain boundaries. We calculated subgrain size using boundary misorientation thresholds of ≥ 2°. This method counts all areas enclosed by boundaries ≥ 2° within area enclosed by ≥ 10° boundaries; no internal boundaries ≥ 2° will be counted as either a subgrain or a grain (see Figure 5 in Trimby et al., 1998). Grain size and subgrain size were calculated as the diameter of a circle with the area equal to the measured area of each grain or subgrain. Note that grain size or subgrain sizes represent the sizes of 2-D cross sections through 3-D grains. The 2-D measurements of a grain will always underestimate the 3-D size. It is also possible that grains, with irregular 3-D geometries, could be appear as two or more separate grains in the same 2-D slice (Monz et al., 2020). To assess these stereological issues, we have analysed the maps with some 1-D lines; the comparison of 1-D and 2-D giving some insights (Cross et al., 2017a) into the effects of taking a 2-D slice through a 3-D volume (section S3 of supplementary material). We have also assessed how many grains are in the same orientation on a 2-D slice. Grains (in 2-D) that are in the same orientation (they have a misorientation below a defined threshold) and in reasonable proximity (which depends on grain size) are

candidates for being 2-D slices through the same grain that has an irregular geometry in 3-D. These analyses are presented in section S3 of the supplementary material.

2.5.2 Crystallographic preferred orientation

EBSD maps with 5 µm and 30 µm step size have been used to generate the crystallographic preferred orientation (CPO) data with one point per pixel. The CPO data were contoured with a half-width of 7.5° based on the maximum of multiples of a uniform distribution (MUD) of the points, to more clearly show the CPO patterns. CPO intensity was quantified using the M-index of Skemer and others (2005). M-indices and eigenvectors (orientation and magnitude) are consistent between CPOs generated from the EBSD maps with 30 µm and 5 µm step sizes.

Ice CPOs formed during uniaxial compression at high temperatures are often characterised by c-axes aligning in an open cone (i.e., a small circle) (Fig. 1(a)) around the compression axis (Kamb, 1972; Jacka and Maccagnan, 1984; Wilson et al., 2014; Jacka and Li, 2000; Qi et al., 2017). The opening-angle, θ, of c-axes cone is considered important in indicating the relative activity of grain rotation and grain boundary migration (GBM), which are competing processes in deforming ice (Piazolo et al., 2013; Qi et al., 2017). In order to quantify cone opening-angles, we counted the number of c-axes that lie at a given angle (co-latitude) from the compression axis—this method is adapted from Jacka and Maccagnan (1984) and Piazolo and others (2013). In practice we counted the c-axes between two co-latitudes separated by a 4° interval (selected by trial, see section S1 of the supplementary material) and calculated the MUD for this co-latitude range to plot on a graph of MUD as a function of co-latitude (Fig. 1(b-c)).

2.5.3 Misorientation

Deformation processes may leave signatures in misorientation data (Fliervoet et al., 1999; Wheeler et al., 2001, 2003; Montagnat et al., 2015; Qi et al., 2017). Misorientation describes the rotation axis and angle required to map one lattice orientation onto another (Wheeler, et al., 2001). Because of crystal symmetry, there is more than one rotation that can be used to describe a misorientation. We chose the minimum rotation angle and corresponding rotation axis to describe misorientation (i.e., the disorientation, in the material science nomenclature—Grimmer, 1979; Morawiec 1995; Wheeler et al., 2001). Here we refer to the minimum rotation angle and corresponding rotation axis as the misorientation angle and misorientation axis, separately. Misorientation angle distributions are illustrated as histograms; misorientation axes distributions are illustrated as inverse pole figures. In this study, we applied three groups of pixel-by-pixel misorientation analyses, using the EBSD data with 5 µm step size:

     (1) Neighbour-pair misorientations: using neighbouring pixels.

     (2) Random-pair misorientations: using randomly selected pixels.

     (3) Grain boundary misorientations: using pixels along the grain boundaries of neighbouring grains.

3 Results

3.1 Starting material

Undeformed samples exhibit a foam-like microstructure with straight or slightly curved grain boundaries and polygonal grain shapes (Fig. 2(a)). The grain size distribution is slightly skewed. The frequencies of grains increase slightly from the minimum cut off grain size (20 µm) to a peak at around 300 µm, and then decrease with further increasing grain size (Fig. 2(b)). Mean and median grain sizes are 297 µm and 291 µm, respectively (Table 3). The mean and median subgrain sizes at 291 and 280 µm, respectively, are very close to mean and median grain sizes (Table 3), indicating that there are very few subgrain boundaries. CPO is close to random (Fig. 2(c)), with an M-index of ~0.004 (Table 2). Neighbour-pair and random-pair misorientation angle distributions both resemble the distribution calculated for randomly oriented hexagonal crystals (Fig. 2(d), Morawiec, 1995; Wheeler et al., 2001).

3.2 Mechanical data

Stress-strain curves are plotted in Fig. 3. Imposed initial strain rate and temperature are shown in Table 1 together with peak and final stresses and corresponding strain rates. The strain rate increases slightly with strain (Table 1), as is required kinematically for a shortening sample at constant displacement rate. For all the deformation runs, stress initially increases as a function of strain, before reaching a peak stress at axial strains of $0.01 \leq \varepsilon \leq 0.04$. Beyond the peak stress, stress deceases with increasing strain, with the rate of stress drop decreasing with increasing strain. The rate of stress reduction is at a minimum, for each temperature, at strains larger than ~0.1. Peak and final stresses are larger at colder temperatures. Ratios of peak stress to stresses at higher strain (e.g. final stress of ~20% strain) are approximately the same at all temperatures so that all curves, when normalised to the peak stress look similar.

3.3 Microstructure

EBSD data are used to generate the illustrative grain orientation maps, grain sub-structure maps, grain size distributions, subgrain size distributions and misorientation angle distributions shown in Figs. 4-6. The grain size and subgrain size distributions are presented as histograms with 4 µm bins. We only show selected areas of EBSD maps so that the reader can resolve microstructural features. Quantitative microstructural analyses are based on much larger areas than those presented in the figures (Table 2).

3.3.1 Sub-structure

All samples deformed at -10 °C and -20 °C show large, lobate grains interlocking with finer, less lobate grains (Fig. 4(a-b), 5(a-b)). Grain boundary lobateness increases at higher strains. The scale of lobateness—that is, the amplitude of grain boundary irregularities—is smaller at -20 °C than -10 °C. At -30 °C lobate grain boundaries are less common at low strains but are a common attribute of larger grains at 20% strain (Fig. 6(a-b)). Samples deformed at -20 °C and -30 °C to strains higher than

~12% show a "core-and-mantle" structure (Gifkins, 1976; White, 1976; Ponge and Gottstein, 1998), characterised by a "net" or "necklace" of finer grains encircling larger grains.

Distinct sub-grain boundaries can be observed in all the samples (Fig. 4 (c), 5 (c) and 6 (c)). Many of the subgrain boundaries appear to be straight, some with slight curvature. A small number have strong curvature. Interconnected subgrain boundaries can be observed in some of the grains. Subgrain boundaries subdivide grains into subgrains.

The colouring of the IPF maps changes with increasing strain, corresponding to the increasing strength of the CPO. At -10 °C, grains with near-pink-and-orange colours dominate the IPF maps at strains higher than ~8% (Fig. 4(a-b)). At -20 and -30 °C, grains with red, pink and orange colours dominate the IPF maps at ~20% strain (Fig. 5(a-b) and 6 (a-b)).

3.3.2 Grain size

For samples deformed to ~3% strain, the grain size distributions are strongly skewed, with a clear main peak at finer grain sizes and a tail of coarser sizes with a possible broad, poorly defined secondary peak corresponding to the mean grain size of the starting material (Fig. 4(d), 5(d) and 6(d)). As strain increases, the grain size distributions generally narrow and shift towards finer grain sizes (Fig. 3(d), 4(d) and 5(d)). The secondary peak, corresponding to the mean grain size of the starting material, becomes harder to see with increasing strain and is absent by 12% strain at all temperatures.

For each sample, we calculated the mean grain diameter ($\bar{D}$) and square mean root diameter ($D_{SMR} = (\overline{\sqrt{D}})^2$) and estimated the peak grain diameter (D_{peak}) by visual inspection of the distributions. D_{SMR} minimizes the bias from very large grains in the calculation of an average. To better describe the statistics of the skewed or bimodal grain size distributions, we also calculated median grain size (D_{median}), lower quartile ($D_{q,25\%}$) and higher quartile ($D_{q,75\%}$). Data are presented in Table 3. $\bar{D}$, D_{SMR}, D_{median} and D_{peak} have the relation of $\bar{D} > D_{SMR} > D_{median} > D_{peak}$, and converge as the strain increases (Fig. 4 (d), 5 (d), 6 (d) and Table 3).

We wish to compare the microstructures associated with different grain size populations. Ideally, we would like to distinguish the microstructural and CPO characteristics of recrystallised grains (i.e., grains formed during the experiment) and remnant grains (i.e., remnants of grains present in the starting material). While the mean diameter, $\bar{D}$, is commonly used to represent a characteristic sample grain size (e.g., Jacka and Maccagnan, 1984; Piazolo et al., 2013; Vaughan et al., 2017; Qi et al., 2017; Qi et al., 2019) it averages the recrystallised and remnant fractions. Lopez-Sanchez and Llana-Fúnez (2015) showed that the frequency peak (D_{peak}) of a grain size distribution provides a robust measure of the recrystallized grain size from the study of deformed rock samples. In our data, the population of grains smaller than D_{peak} is too small, in many samples, to provide representative data. Instead, we define, for each temperature series, a threshold grain size, equal to the D_{SMR} of the sample deformed to ~12% strain. Grains with the grain sizes greater than the threshold are classified as "big" grains and grains smaller than or equal to the threshold are classified as "small" grains.

Stereological artefacts inevitably arise from looking at microstructures on two-dimensional sections. Here we analyse two distinct (albeit related) stereological issues. The first issue relates to the *misidentification* of "small" grains, as these could

appear from slices cut close to the perimeter of a large grain in 3-D (Underwood, 1973). The second issue relates to the *oversampling* of grains that have highly irregular, branching shapes in 3-D and appear more than once on a 2-D surface (Hooke and Hudleston, 1980; Monz et al, 2020).

It is clear that 2-D grain size measurements will always underestimate the "true" 3-D grain size (Underwood, 1973; Berger et al., 2011). A trickier problem lies in understanding how, specifically, grain size distributions in two dimensions relate to those in three dimensions. As we have categorized grains in 2-D maps as "big" and "small" grain, we need to assess the likelihood of a "small" grain in 2-D being a slice through of a "big" grain in 3-D. One way to estimate this is to further flatten the two-dimensional data into one-dimension and measure grain sizes along a line. From this analysis, we can evaluate the likelihood that a "small" 1-D grain is indeed a "small" grain in 2-D. This analysis is presented in section S3 of the supplementary material. At ~20% strain the percentage of "small" grains on a 1-D line that correspond to "small" grains in the 2-D EBSD map is 64%, 76% and 43% at -30, -20 and -10 °C, respectively. These data suggest that at 20% strain the presence of "small" grains in 3-D is likely, with the confidence in this statement increasing at reduced temperatures. Another observation supports this: at 20% strain many "small" grains have "small" grain neighbours (Fig. 4-7). At -30 °C and -20 °C some "small" grains are entirely surrounded by other "small" grains. At -10 °C there are lines of "small" grains in contact along the boundary between "large" grains. It is very difficult (and at -30 °C impossible) to have all of these "small" grains linked to large grains in the third dimension whilst maintaining a microstructure (e.g. in an orthogonal plane) that looks like the microstructures in these maps. This is the case at 20% strain. At lower strains the percentage of "small" 1-D segments that correspond to "small" 2-D grains is lower so the confidence with which we can define "small" grains is reduced.

The linear intercept analyses described in the previous paragraph also allow a crude assessment of grain oversampling—in other words, how likely are we to measure a large, branching grain more than once? In all samples >90% of 2-D grains along an arbitrary line are unique (that is, they are cut only once). Of course, with lines in multiple directions the percentage of unique grains might decrease. Using EBSD crystal orientation data, we can assess the likelihood of nearby grains in the 2-D map belonging to the same grain in 3-D (Monz et al., 2020). For every grain identified within a given EBSD map, we searched for all the nearby grains misoriented by less than a 10°, within a 1mm radius. These thresholds probably overestimate the number of grains connected in 3D. 1mm is close to double the size of the largest grain and 10° is more than twice the median and significantly larger than the higher quartile in mis2mean data (the misorientation angle between all pixels in a grain and the mean orientation of that grain) for all samples.

Full details are outlined in section S4 of the supplementary material and key outcomes are listed in Table 3. The percentage of "unique" grains (that only appear at the surface once) relative to all grains in a 2D map is higher than 68% at all temperatures and strains (Table S2, Table 3). The procedure outlined in the last paragraph allows us to estimate the number of "distinct" grains (where all 2-D grains attributed to the same 3-D grain are counted as one grain) in each map and from this, the number density (grain number per unit area) of "distinct" grains. The number density of "distinct" grains within all deformed samples at all temperatures is greater by a factor of 3 than that in the starting material: reaching values > 6 times the starting material at -10 °C and >11 times the starting material at lower temperatures (Fig. 11(c), Table 3). The number density of "distinct"

grains is generally higher at strains of ε ≥~12% than at strains of ε ≤~8% at all temperatures, and it is generally higher in samples deformed at -20 and -30 °C than samples deformed at -10 °C (Fig. 11(c), Table 3).

The analyses above provide some confidence that in all the experiments the number density of grains has increased relative to the starting material and increases with strain. If we couple this to the grain size statistics presented and the analysis of whether we are misidentifying small grains, the weight of evidence suggests that we have a real population of smaller grains. Our confidence in this statement increases with reducing temperature and increasing strain. Now we come back to the issue of how we distinguish "big" and "small" grains. Our scheme for separating "big" and "small" grains, using D_{SMR} of the sample deformed to ~12% strain as the threshold, is not perfect, but it does provide a fast and repeatable way of looking at the possible differences in microstructures and CPO of smaller and larger grains. The grain size threshold chosen (peak, mean, median and SMR) to separate "big" and "small" grains has little impact on the CPOs of the "big" and "small" grain populations (see section S5 of the supplementary material).

3.3.3 Subgrain size

Subgrain size distributions (Fig. 4(e), 5(e) and 6(e)) are similar to the grain size distributions (Fig. 4(d), 5(d) and 6(d)), but the median and mean subgrain sizes are smaller than median and mean grain sizes (Table 3, Fig. 11(b)). In many cases, particularly at lower temperatures, the peak corresponds to the lower grain size resolution (cut off) indicating that we could be missing smaller subgrains. For this reason, the peak subgrain sizes are not useful and the median and mean subgrain sizes probably represent overestimates. The interquartile range (IQR) of subgrain sizes, with upper and lower limits bounded by higher quartile and lower quartile subgrain sizes, respectively, generally decreases with an increasing strain at all temperatures (Fig. 11(b)). IQR covers a wide range of subgrain size for samples deformed at -10 °C, but it narrows as the temperature decreases (Fig. 11(b)).

3.3.4 Misorientation

Misorientation angle distributions are presented for misorientations between 2° and 20° (Fig. 4(f), 5(f), 6(f)). Random-pair misorientation angle distributions show the misorientations expected for the measured CPO. It is important to identify differences between neighbour- and random-pair distributions, as these can be attributed to orientation inheritance, among other processes (Wheeler et al., 2001). Neighbour- and random-pair distributions at misorientation angles greater than 20° (not shown) are very similar in all samples, indicating that these are simply a function of the CPO. In all deformed samples there is a large peak at 2° in neighbour-pair data that is not present in random-pair data. The difference between neighbour-pair and random-pair frequency lessens as misorientation angle increases. The misorientation angle at which neighbour-pair frequency has reduced to be equal to the random-pair frequency increases with decreasing temperature. At -10°C, it is at 10° to 14° and does not change substantially with strain. At -20°C this angle is 10° to 14° at low strain but increases to around 18°-20° at 12% and 20% strain. At -30°C this angle is 16° to 18° at 3% strain, 18° to 20° at 5% strain and 20° at higher strain.

Neighbour-pair misorientation axes at misorientation angles 5°-10° show primary maxima lying in the basal plane (Fig. 4 (g), 5(g), 6(g)) for all deformed samples. Misorientation axes below 5° are omitted from these plots as the axes have relatively high angular errors (Prior, 1999). Misorientation axes from 2°-5° (not shown for all: an example is in Fig. 8(c)) also lie dominantly in the basal plane but have lower intensities, which we attributed to higher angular error. Grain boundary (>10°) misorientation axes for neighbouring grains are not strongly aligned. There is a very slight preference for misorientation axes lying in the basal plane (except PIL007) and this preference is slightly stronger at colder temperatures.

Figure 7 illustrates misorientation analyses of a typical "core-and-mantle" structure characterized by "small" grains (illustrated with thin boundaries) arranged along boundaries of "big" reference grains (ref1 to ref5 illustrated with thick boundaries) in sample PIL268 (-30 °C, ~20% strain). The c-axes of reference grains are dispersed in a complex way, with the c-axes within an individual reference grain varying by up to ~20°. The complex dispersions include some data that lie along great circles and maybe some small circles. Great circle dispersions indicate rotation axes in the basal plane, consistent with neighbour-pair misorientation axes of low angle boundaries, which have a primary maximum parallel with poles to m-planes ([-1100]) (Fig. 7(c)). The c-axes of "small" grains are dispersed around the c-axes of "big" reference grains (Fig. 7(b)); the small grains occupy a much wider range of orientations than the large grains. Some of the small grains have c-axes within the single grain that are dispersed in a great circle smear, with up to ~5° of c-axis orientation variation. The distributions of misorientation axes between each of the reference grains and it's neighbouring small grains show no particular pattern apart from an absence of misorientation axes close to [0001]. These are all high-angle (>10°) misorientation so the axis errors will be small (Prior, 1999). The boundary misorientation axes between neighbouring "small" grains are distributed relatively uniformly (Fig. 7(d)), apart from an absence of data close to [0001].

3.4 Crystallographic preferred orientations

The contoured c-axes, a-axes and poles to m-planes pole figures are illustrated in Fig. 8-10. The c-axes figures are presented with (1) the compression axis vertical and (2) the compression axis perpendicular to the page. These two reference frames, which are commonly used by different communities, enable different elements of symmetry to be illustrated. At all temperatures CPO intensity increases with strain.

3.4.1 -10 °C series

The CPO of the sample (PIL176) deformed to ~3% strain at -10 °C is characterized by several weak maxima of c-axes with similar angles relative to the compression direction, and random distributions of a-axes and poles to m-planes. As the strain increases from ~5%, the CPO becomes clearer, with c-axes aligned in a cone (small circle). The cone is incomplete, with distinct maxima that are distributed along a small circle and individually elongated along the small circle trajectory. The a-axes and poles to m-planes align in a broad swath along the plane perpendicular to the compression axis and bound by the c-axis cone.

3.4.2 -20 °C series

The CPO of the sample (PIL183) deformed to ~3% strain at -20 °C is very weak. At ~5% strain (PIL182), the CPO is characterized by a blurred cone formed by several weak maxima of *c*-axes, and randomly distributed *a*-axes and poles to *m*-planes. As the strain increases from ~8% to ~12%, the CPO becomes clearer, with *c*-axes aligned in distinct clusters superposed on a blurred broad small circle cone. The *a*-axes and poles to *m*-planes align in weak a broad swath along the plane perpendicular to the compression axis and bound by the *c*-axis small cone. At ~20% strain, the *c*-axes align in two clusters that lie in a cone (small circle), and the *a*-axes and poles to *m*-planes align in broad swath along the plane perpendicular to the compression axis and bound by the *c*-axis small cone.

3.4.3 -30 °C series

The CPOs of the samples (PIL165, PIL162) deformed to ~3% and ~5% strain at -30 °C are very weak. As the strain increases from ~8% to ~12%, the *c*-axis CPO exhibits a pattern of a distinct narrow cone superposed on an overall broad cluster, the *a*-axes and poles to *m*-planes align in a broad swath along the plane perpendicular to the compression axis. At ~20% strain, the *c*-axes align in distinct clusters superposed on an overall broad cluster, and the *a*-axes and poles to *m*-planes align in a broad swath along the plane perpendicular to the compression axis and bound by the *c*-axis narrow cone.

3.4.4 CPOs of different grain size fractions

"Big" and "small" grains have similar patterns of *c*-axes (i.e. maxima in approximately the same places)—samples deformed to ~12% strain illustrate this (Fig. 12). The data are taken from smaller area maps (Table 2) with a 5 μm step size; the CPOs for all grains are comparable to data from larger areas using a 30 μm step size (compare Fig. 12a with Fig. 8-10), with CPOs from the 30 μm maps being slightly weaker. At -10 °C, the CPO intensity of "small" grains is slightly lower than "big" grains (Fig. 12(b-c)). This contrast becomes strengthened as the temperature decreases. At -30 °C the CPO intensity of "small" grains is much lower than "big" grains (Fig. 12(b-c)). CPO intensity is not significantly affected by the number of grains used to calculate M-index—we verified this by calculating M-index for a subpopulation of small grains, of the same size as the "big" grain population (Fig. 12(d)).

To show how CPO strength differs for "big" and "small" grains for the whole data set we plot the M-indices for the grain size categories against strain (Fig. 11(d)). For all the deformed samples, the M-indices of "big" grains have the same pattern with strain as the complete data set (all grains). The "small" grains generally have lower M-indices at strains of $\varepsilon \geq$ ~5%. The grain size threshold ($\overline{D}$, D_{SMR}, D_{median} and D_{peak}) chosen to separate "big" and "small" grains has a minor impact on CPO, with no significant change in CPO pattern or intensity (see section S5 of the supplementary material for the test).

3.4.5 The opening-angle of the *c*-axis cone

To increase our understanding of the processes that might control the *c*-axes cone opening-angle θ, we plotted data from this study and previous studies in a diagram of θ as a function of strain with data subdivided with different temperatures and strain rates (Table 4 and Fig. 13). For data from the literature, we digitised the *c*-axis orientations from published stereonets (Jacka and Maccagnan, 1984; Jacka and Li, 2000) and calculated θ using the same method described in Section Two (Method). For data from Montagnat and others (2015) and Craw and others (2018), we measured the values of θ directly from contoured *c*-axis CPO figures. For data from Vaughan and others (2017), we calculated the values of θ from raw EBSD data. The values of θ from Hooke and Hudleston (1981), Piazolo and others (2013), Qi and others (2017) and Wilson and others (2020) are taken directly from these papers. The experiments reported by Piazolo and others (2013) were conducted on D_2O ice at -7 °C, which is a direct analogue for deforming H_2O ice at −10 °C (Wilson et al., 2019). These angles were analysed using methods similar to ours. In order to make a direct comparison with the data reported from this study and Qi and others (2017), we converted the reported axial engineering strain (e) and strain rate ($\dot{e}$) (Piazolo et al., 2013; Montagnat et al., 2015; Vaughan et al., 2017) to true axial strain (ε) and strain rate ($\dot{\varepsilon}$) using the equations:

$$\varepsilon = -\ln(1 - e) \tag{4}$$

$$\dot{\varepsilon} = \frac{\dot{e}}{1 - e} \tag{5}$$

Equation (6) and (7) were used to forward model axial engineering strain (e) and strain rate ($\dot{e}$) from octahedral shear strain (γ) and strain rate ($\dot{\gamma}$) (Jacka and Maccagnan, 1984; Jacka and Li, 2000).

$$\gamma = \frac{\sqrt{2}}{3}\left(e + \frac{1}{\sqrt{1-e}} - 1\right) \tag{6}$$

$$\dot{\gamma} = \frac{\sqrt{2}}{3}\left(\frac{1}{2(1-e)^{\frac{3}{2}}} + 1\right)\dot{e} \tag{7}$$

After that, the axial engineering strain (e) and strain rate ($\dot{e}$) were converted to true axial strain (ε) and strain rate ($\dot{\varepsilon}$) using Eq. (4) and Eq. (5).

For natural ice samples (top of the south dome, Barnes Ice Cap, Baffin Island) from Hooke and Hudleston (1981), Eq. (8) was used to calculate axial engineering strain (e) from natural octahedral unit shear strain ($\bar{\gamma}_{oc}$). Values of $\bar{\gamma}_{oc}$ were taken from Fig. 4 of Hooke and Hudleston (1981) based on the assumption that ice was deformed under uniaxial compression. After that, the axial engineering strains (e) were converted to true axial strains (ε) using Eq. (4). Hooke and Hudleston (1981) assumed their natural ice samples were deformed under a constant vertical strain rate, $\dot{e}$, of $5.71 \times 10^{-11} s^{-1}$, which converted to true axial strain rate ($\dot{\varepsilon}$) using Eq. (5). The derivations of Eq. (4-8) are shown in section S2 of the supplementary material.

$$\bar{\gamma}_{oc} = \frac{2\sqrt{2}}{3}\left(e + \frac{1}{\sqrt{1-e}} - 1\right) \tag{8}$$

To our knowledge, Fig. 13 contains data from all published 3-D uniaxial compression ice experiments and deformed natural ice that present *c*-axis CPOs as a function of strain. 2-D experiments, involving deformation on a microscope stage (e.g. Peternell et al., 2014; Peternell and Wilson, 2016) are excluded as these have different kinematics. There are numerous other high temperature and low strain rate axial compression experiments to strains of ~10% to 30% where *c*-axis cones have opening-angles of ~35 degrees (e.g., Wilson and Russell-Head, 1982; Gao and Jacka, 1987; Treverrow et al., 2012; Wilson et al., 2019). These data are consistent with the pattern shown in Fig. 13 but are not part of a strain series and are not added to the diagram to maintain clarity. There are comparatively few CPOs from samples at low temperatures (< -15 °C) so we have included all published data from experiments at < -15 °C irrespective of whether these are part of a strain series. The values of θ are scattered between 0° and 42° for all experiments. Experiments to low strains have random CPOs where a cone angle cannot be defined, and these data are not shown on Fig. 13. For experimental data, the evolution pattern of θ as a function of strain at temperatures warmer than -15 °C show θ decreases with increasing strain up to ~20% true axial strain. The only two data points of θ from samples deformed to the strain of ~50% are at 30°. There is little difference as a function of temperature at ≥ -15 °C. For natural ice deformed under temperatures of -4 to -6 °C, θ generally decreases with increasing strain for both "coarse" ice (>0.15 cm2) and "fine" ice (<0.1 cm2).

Samples deformed at temperatures colder than -20 °C have lower θ values compared with samples deformed at warmer temperatures at similar strains. At -30 °C, the opening-angle of the *c*-axis cone decreases to ~0° at strains of ~20%. The strain corresponding to the formation of a clear *c*-axis cone (non-random CPO) increases with decreasing temperature.

4 Discussion

4.1 Deformation mechanisms

4.1.1 Inferences from mechanical evolution

All stress-strain curves (Fig. 3) show stress rising to the peak stress and then relaxing, with the rate of stress drop decreasing with strain. This pattern matches published constant-displacement-rate experiments (Mellor and Cole, 1982; Durham et al., 1983; Durham et al., 1992; Piazolo et al., 2013; Vaughan et al., 2017; Qi et al., 2017; Craw et al., 2018; Qi et al., 2019), and has an approximate inverse relationship (Mellor and Cole, 1982, 1983; Weertman, 1983) to constant-load experiments (Budd and Jacka, 1989; Jacka and Li, 2000; Treverrow et al, 2012; Wilson and Peternell, 2012) where strain rate first decreases to a minimum and then increases to approach a near-constant strain rate.

Stress-strain curves of all experimental runs show a smooth and continuous increase of stress as a function of strain before reaching the peak. Approximately linear portions of the stress-strain data prior to peak have been termed quasi-elastic (Kirby et al., 1987). Slopes of ~1GPa are significantly below the published value of Young's modulus (~9GPa: Gammon et al, 1983) and indicate that there is significant dissipative deformation here. This likely includes anelastic deformation related to intergranular stress redistribution used to explain primary creep in constant load experiments (Duval et al, 1983; Castelnau et

al., 2008). The curvature of the stress-strain line at the start of each experiment may relate to initial porosity loss as suggested by rapid increases in ultrasonic p-wave velocity in comparable experiments by Vaughan and others (2017).

As our experiments are all at the same approximate strain rate, we cannot calculate the stress dependency of strain rate (the stress exponent, n). Qi and others (2017) calculate a peak stress n value of 3 and flow stress n value of 3.9 for comparable experiments (including PIL007 used here) at -10 °C. Craw and others (2018) calculate a peak stress n value of 4.1 for comparable experiments at -30 °C. Our experiments show higher peak and final stress values at colder temperatures than at warmer temperatures. This phenomenon is well known, and the temperature dependence of the creep rate is commonly parameterised using an Arrhenius relationship with an activation energy (Homer and Glen, 1978; Durham et al., 1983, 2010; Budd and Jacka, 1989; Cuffey and Paterson, 2010; Scapozza and Bartelt, 2003). Our peak and final stress data can be used to calculate the activation energy by assumption of a value of stress exponent, n (see section S6 of the supplementary material for the calculation). A best fit to all data (-10, -20 and -30 °C) give activation energy of 98 kJ/mol and 103 kJ/mol from peak and final stress data assuming n=3 and 131 kJ/mol and 138 kJ/mol from peak and flow stress data assuming n=4. These numbers are consistent with published values (64-250 kJ/mol) at relatively high temperature (Glen, 1955; Goldsby, 2001; Budd and Jacka, 1989; Cuffey and Paterson, 2010; Durham et al., 2010; Kuiper et al., 2020a, 2020b).

4.1.2 Inferences from microstructure

4.1.2.1. Nucleation

The number density (number of grains per unit area) of "distinct" grains (counting 2-D grains attributed to the same 3-D grain as one: section S4 of supplementary material) increases by more than a factor of 3 over that of the starting material in all deformed samples at all temperatures (Table 3). We can be reasonably confident that the number of grains in the samples has increased as a function of deformation, which requires a process of nucleation to create new grains. For all the deformed samples, the grain size distributions are characterised by peaks at finer grain sizes, and a smaller mean/median grain size compared with the undeformed sample (Fig. 2, 4-6, Table 3). The smallest grains in the deformed samples were not present in the starting material. These observations suggest that nucleation generates the grains with smaller sizes. The number of grains per unit area (accounting for multiple occurrences of the same 3-D grain) generally increases and all measures of 2-D grain size decrease with strain (Table 3), at all temperatures, suggesting that nucleation operates continuously as part of the recrystallisation process throughout the deformation.

4.1.2.2. Dislocation activity, recovery, subgrain rotation and subgrain rotation recrystallisation

Microstructure maps show subgrain boundaries in all deformed ice samples (Fig. 4(a-c), 5(a-c) and 6(a-c)). The subgrain boundary geometry is comparable with other experimentally or naturally deformed rock and metal samples, e.g. quartz (Cross et al., 2017a; Killian and Heilbronner, 2017), olivine (Hansen et al., 2012), Magnox alloy (Wheeler, 2009) and zircon (MacDonald et al., 2013). The misorientation axes for subgrain boundaries are generally rotations around rational crystallographic axes, particularly directions in the basal plane, suggesting that the boundaries may represent arrays of

dislocations (Humphreys and Hatherley, 2008; Shigematsu et al., 2006). There is much higher frequency of low angle (Particularly < 10°) neighbour-pair misorientations than are expected from the CPO (as shown by the random-pair misorientation angles). The subgrain boundaries and the pattern of misorientation angles are commonly interpreted as the result of dynamic recovery of dislocations generated during deformation and subsequent subgrain rotation related to ongoing

5   recovery (Guillope and Poirier, 1979; Trimby et al., 1998; Fliervoet et al., 1999; Wheeler et al., 2001) and has been observed from ice deformation experiments previously and interpreted in this way (e.g. Montagnat et al., 2015; Qi et al., 2017; Seidemann at al., 2020). The misorientation angle at which neighbour-pair frequency has reduced to be equal to the random-pair frequency increases with decreasing temperature (Fig. 4 (f), 5(f), 6(f)). This observation suggest intragranular distortion is more significant at lower temperatures.

10   Subgrain rotation is a process that involves an increase in the misorientation across a subgrain boundary forming via the progressive addition of dislocations (White., 1979; Lallemant, 1985). New grains will form as the misorientation across the subgrain boundary becomes large enough, with the subgrain boundary eventually dividing its parent grain (Poirier and Nicolas, 1975; Guillope and Poirier, 1979; Urai et al., 1986; Halfpenny et al., 2006; Gomez-Rivas et al., 2017). This process is known as subgrain rotation recrystallization (Hirth and Tullis, 1992; Stipp et al., 2002; Passchier and Trouw, 2005). When subgrain

15   rotation recrystallization is responsible for nucleation, the recrystallized "daughter" grains should be initially of a similar size to the internal subgrain size of the "parent" grain (Urai et al., 1986). At all temperatures and strains the mean, median, lower quartile and upper quartile values of subgrain sizes are smaller than that of grain sizes (Table 3). This indicates that the subgrain rotation recrystallization could be the nucleation mechanism that generates the "small" grain population. Previous studies on deformed metals and quartzites describe the structure of smaller grains encircling larger grains as "core-and-mantle" structure

20   (Gifkins, 1976; White, 1976). The production of smaller grains that form the "mantle" region was considered as a result of continual rotation of subgrains to develop small strain-free grains (White, 1976; Urai et al., 1986; Jacka and Li, 2000). The network of smaller grains that encircle bigger grains at strains higher than 12% at -20 and -30 °C is consistent with the operation of subgrain rotation recrystallization. The network of finer grains encircling larger grains has been observed in deformed metals, and it is named the "necklace structure" in the material science literature (e.g. Ponge and Gottstein, 1998; Jafari and

25   Najafizadeh, 2009; Eleti et al., 2020).

For all deformed samples, neighbour-pair misorientation axes at misorientation angles of 5°-10° show primary maxima lying in the basal plane (Fig. 4(g), 5(g), 6(g)). Similarly, misorientation axes of 5°-10° boundaries within the large reference grains of the "core-and-mantle" structure have primary maxima lying in the basal plane (Fig. 7(c)). These observations suggest low-angle boundaries (5°-10°) are crystallographically controlled, consistent with them being subgrain boundaries that comprise

30   arrays of dislocations.

The general understanding of the subgrain rotation recrystallisation process (Poirier, 1972; Poirier and Nicolas, 1975), is that a new "nucleus" forms when all of the enclosing subgrain boundaries, comprising arrays of dislocations, are transformed to grain boundaries, that have no formally defined structure (Rollett et al., 2017). In simplified terms there is a limit to the misorientation that can be sustained by an array of dislocations (related to limits of the Read-Shockley equation: Read and

16

Shockley, 1950; Rollett et al., 2017) so at some point continued addition of dislocations to a boundary prompts the change in boundary structure. There is no mechanism understood by which the misorientation of a subgrain boundary changes when it transforms to a grain boundary. Thus, high-angle grain boundaries of nuclei generated by subgrain rotation recrystallization should have the same orientation as the subgrain that forms the nucleus and should also be crystallographically controlled (Rollett et al., 2017), if additional processes are not activated after their production.

In all deformed samples, neighbour-pair misorientation axes at misorientation angles larger than 10° have a distribution close to random (Fig. 4(g), 5(g), 6(g)), suggesting high-angle grain boundaries lack a crystallographic control. The "core-and-mantle" structures observed at lower temperatures (-20 °C and -30 °C) have misorientations axes of boundaries between small grains and their large or small neighbours that do not lie in the basal plane and have no preferred nor rational crystallographic orientation (Fig. 7(d)). High-angle grain boundaries of "small" grains lack a crystallographic control within deformed samples. Subgrain rotation recrystallisation can be considered a nucleation mechanism, but alone it cannot explain the misorientation axes of high angle boundaries. Either a different nucleation mechanism is needed or an additional process is needed to change the orientation of grains during or after nucleation. This discussion continues in the context of the CPO data in section 4.1.4.

All measures of grain and subgrain sizes are smaller at lower temperatures (Table 3, Fig. 11(b)). This is likely a consequence of the higher stresses of the lower temperature experiments resulting in smaller subgrain and recrystallised grain sizes through a piezometer or similar relationship (Derby, 1991; Austin and Evans, 2007; Lopez Sanchez and Llana Funez, 2015; Cross et al., 2017a). Jacka and Li (1994) show an inverse relationship between ice grain size and stress from deformed ice samples that reach tertiary creep.

4.1.2.3. Grain boundary migration

Lobate grain boundaries are commonly interpreted as the result of strain-induced grain boundary migration (GBM) (Urai et al., 1986; Jessell, 1986; Duval and Castelnau., 1995). Samples deformed at -10 and -20 °C show more grains with lobate boundaries at higher strains (>~3%), suggesting more widespread strain-induced GBM with an increasing strain. The proportion of repeated (i.e. interconnected and highly lobate) grains is generally higher in the higher-temperature experiments (Table 2, section S4 of the supplementary material). This observation suggests that GBM is also more widespread at higher temperatures. It is worth noticing that data presented in this study is not sufficient enough to quantify the rate of GBM at high and low temperatures. Because the rate of GBM depends on two parameters; the boundary mobility, which is a function of temperature, and the driving force, conventionally the dislocation density difference (Humphreys and Hatherley, 2008). The dislocation density difference is likely to be controlled by stress (Bailey and Hirsch, 1960; Ajaja, 1991). Under a lower temperature, the grain boundary mobility is likely to reduce. However, the differential stress for a given strain rate increases (Fig. 3). Consequently, the dislocation density difference is likely to be higher at a lower temperature.

4.1.3 CPO development

The CPO intensity and opening-angle of the *c*-axis CPO decrease as the temperature drops. Previous studies suggest the CPO development is mainly controlled by the deformation and recrystallization mechanisms (Alley, 1992; Qi et al., 2017). Fig. 14 explains how key processes (Fig. 14(b)) involved in the deformation and recrystallization mechanisms (Fig. 14(a)) may affect the CPO development as a function of strain and temperature (Fig. 14(c)). Many deformed samples exhibit an incompleteness of *c*-axes cone (lack of cylindrical symmetry) (Fig. 8-10). The incompleteness of *c*-axes cone is more severe for 5 µm EBSD maps collected from a much smaller area than 30 µm EBSD maps (Fig. 12). These phenomena are common to all ice CPOs from measurements on a single sample planes (by EBSD or optical methods: see any of the papers cited), but are not so apparent in neutron diffraction data (Piazolo et al., 2013; Wilson et al., 2019), that sample a larger volume, suggesting that a single plane through a deformed sample does not generally contain sufficient grains for a fully representative CPO.

Our -10 °C series CPO data show a monotonic increase in CPO intensity as indicated by M-index, and a clearer cone-shaped pattern of the *c*-axes with increasing strain. Similar observations were made in previous ice deformation experiments (e.g. Jacka and Maccagnan, 1984; Piazolo et al., 2013; Montagnat et al., 2015; Vaughan et al., 2017; Qi et al., 2017). Cone-shaped *c*-axes CPOs have been related to strain-induced GBM favouring the growth of grains with easy slip orientations (high Schmid Factors) (Duval and Castelnau., 1995; Little et al., 2015; Vaughan et al., 2017; Qi et al., 2017). Linked to this is the idea that grains with hard slip orientations should have greater internal distortions (Duval and Castelnau., 1995; Bestmann and Prior 2003), and therefore store higher internal strain energy. If this is correct then hard slip grains are likely to be consumed by grains with easy slip orientations through GBM (Duval and Castelnau., 1995; Castelnau et al., 1996; Bestmann and Prior, 2003; Piazolo et al., 2006; Killian et al., 2011; Qi et al., 2017; Xia et al., 2018). However, we have to re-evaluate the detail of this idea, as recent studies on deformed ice samples show there is no systematic relation between orientation and strain localisation at low strain (Grennerat et al. 2012). Furthermore, studies of high-strain shear samples find no clear difference in the geometrically necessary dislocation density within the two maxima that develop in simple shear (Journaux et al. 2019). An alternative, and as yet incomplete, explanation from Kamb (1959) relates recrystallisation directly to the elastic anisotropy of crystals and through this to the orientation of the stress field. At this stage the observation that ice CPOs developed at relatively high temperature and particularly at low strain correspond to high Schmid factor orientations remains robust. The underlying mechanisms will need continual review as we collect new data.

At temperatures greater than -10° the cone opening angle (θ) from experiments decreases from 42° at ~3% strain to ~ 30° at 20-50% strain. Hooke and Huddleston's (1981) data from Barnes ice cap suggest it may reduce further to ~18° at ~143% strain (Table 4, Fig. 13). The cone opening angle does not stabilise at the easiest slip orientation of 45°, suggesting that GBM alone cannot be the mechanism that controls the CPO development. Previous studies suggest CPO evolves through the parallel operation of rotation and selective growth (e.g. Kamb, 1972; Qi et al., 2017). The narrowing of cone-shaped *c*-axis CPO has been explained by an activation of grain rotation (Jacka and Li., 2000; Qi et al., 2017). Jacka and Maccagnan (1984) show that the *c*-axis cone narrows in compression and opens in extension, consistent with the expected kinematics of grain rotation.

Neighbour-pair misorientation axes at misorientation angles of 5°-10° show primary maxima lying in the basal plane (Fig. 4(g), 5(g), 6(g)) at both low and high strains. Therefore, we infer the decreasing of opening-angle θ as a function of strain is likely to result from more active grain rotation driven by intracrystalline glide on the basal plane. For all deformed samples in this study, there is a large peak at 2° in neighbour-pair misorientation angle distribution, which is not present in the random-or neighbour-pair data of the starting material (Fig. 4(f), 5(f), 6(f)). Moreover, neighbour-pair misorientation angles show much higher frequencies between 2° and 10° than random-pair data. These observations suggest recovery and subgrain rotation operated in parallel with strain-induced GBM. The dislocation activity required to generate subgrain structures and to provide the strain energy driving force for strain-induced GBM is likely the primary control on grain rotation (Duval and Castelnau, 1995; Llorens et al., 2016).

The opening-angle θ of the c-axes cone as well as the CPO intensity decrease with decreasing temperature (Table 2, 4; Fig. 8-10, 11(c), 13). Earlier studies have inferred that the selective growth of the grains oriented for easy slip orientations becomes less active due to the reduction of GBM activity at lower temperatures (Qi et al., 2017, 2019). Lower temperatures, for constant displacement rate experiments, correspond to higher stresses. Previous studies in deformed metals suggest a higher stress is likely a cause of higher dislocation densities (Bailey and Hirsch, 1960; Ajaja, 1991), that in turn will require kinematically more lattice rotation. The misorientation angle at which neighbour-pair frequency reduces to be equal to the random-pair frequency increases with decreasing temperature (Fig. 4(f), 5(f), 6(f)). Moreover, neighbour-pair misorientation axes at misorientation angles of 5°-10° show primary maxima lying in the basal plane (Fig. 4 (g), 5(g), 6(g)) for all deformed samples. These observations support the hypothesis that grain rotation becomes more prominent at lower temperatures (Jacka and Li., 2000), and it is dominantly driven by intracrystalline glide on the basal plane. More active grain rotation can lead to a closure of c-axis cone at lower temperatures: maxima parallel to compression are characteristic of strains $\geq$ 20% at temperatures colder than -30 °C (Craw et al., 2018; Prior et al., 2015).

4.1.4 CPO development: differences related to grain size

The CPO intensity (as indicated by M-index) of "small" grains is generally lower than "big" grains, and this contrast strengthens with decreasing temperature (Fig. 11(d)). At ~12% strain, the CPO pattern of "big" grains is clearer than "small" grains, at all temperatures (Fig. 12). These observations suggest a mechanism that weakens the CPO development may be associated with the "small" grains. Microstructural analyses suggest subgrain rotation and subgrain rotation recrystallization are dominant processes responsible for the production of "small" grains within samples deformed at both high and low temperatures (see section 4.1.2.2). Subgrain rotation and subgrain rotation recrystallization will disperse orientations away from the parent grain orientation and small grains, if representative of nuclei formed by subgrain rotation recrystallization will represent the most extreme dispersion from the parent orientation. However, subgrain rotation recrystallization alone should produce nuclei with crystallographically controlled grain boundaries linked to the parent grain orientation. As this is not the case (see section 4.1.2.2) it is difficult to explain the weakening of the CPO by subgrain rotation recrystallization alone; additional processes must be responsible for a weaker CPO within small grains. Data from our experiments suggest such

19

hypothesis works better for experiments at -20 and -30 °C. At -10 °C the contrast of CPO intensity between "big" and "small" grains becomes less clear, and the "core-and-mantle" structure is absent. One way to explain these data is that the modification of grain boundary topology via grain boundary migration (GBM) could be more widespread at a warmer temperature, which could obscure evidence of the additional process responsible for a weaker CPO in smaller grains. The interaction of GBS with

5   dislocation processes and GBM is developed a little in the ice literature (Hondoh and Higashi, 1983; Liu et al, 1993; 1995; Duval, 1985; Faria et al., 2014) and experiments that show offsets of grain boundaries whilst GBM occurs (Drury and Humphreys 1988; Ree, 1994) suggest that GBS may not leave a clear microstructural signal when GBS and GBM coexist. There are two candidate processes that may explain weakening of CPO in smaller grains and the lack of rational crystallographic misorientation axes of small grains relative to each other or to larger grains.

10   1.   Previous rock deformation studies reported small recrystallized grains having CPOs that are randomly dispersed equivalents of the stronger parent grain CPOs (Jiang et al., 2000; Bestmann and Prior, 2003; Storey and Prior, 2005; Warren and Hirth, 2006). These observations are commonly interpreted as the result of an increase in the contribution of grain boundary sliding (GBS) in fine grains right after their formation via subgrain rotation recrystallization. Craw and others (2018) reported similar interpretations in uniaxially deformed Antarctic ice, and the reduction of CPO

15   intensity in grains with finer sizes was attributed to GBS. Bestmann and Prior (2003) suggest a randomization of boundary misorientation axes among "small" grains can result from sliding along boundaries of newly formed grains. GBS can accompany grain shape change by dislocation or diffusion processes (Raj and Ashby, 1971; Crossman and Ashby, 1975; Langdon 1994, 2006, 2009). Recently, Cross and others (2017b) found evidence for specific orientations (i.e., those lying in the plane of maximum vorticity) being randomized by GBS. GBS is inherently grain

20   size sensitive (Raj and Ashby, 1971; Gifkins 1976; Langdon, 1994; Warren and Hirth, 2006) and interpretation of GBS processes in fine polycrystalline ice was initially made by identification of grain size sensitivity of mechanical data for the deformation of fine-grained ice (Goldsby and Kohlstedt, 1997, 2001).

    2.   Microstructural studies of metals deformed under high homologous temperatures suggest a possibility of nucleation of grains with random orientations at the tip of irregular boundaries of "parent" grains (Hasegawa and Fukutomi,

25   2002; Hasegawa et al., 2003). Such hypothesis is similar to "spontaneous" nucleation (Duval et al., 2012), a process considered driven by the relaxation of the dislocation-related internal stress field that may produce nuclei with orientations not related to their corresponding parent grains. Adoption of this interpretation would require that small grains are not generated by subgrain rotation recrystallisation. Falus and others (2011) suggests bulging, which allows for higher misorientations between parent and recrystallized grains, could explain a higher dispersion of CPOs.

30   The two hypotheses—GBS and nucleation of grains with random orientations—can explain a weakening of CPO in "small" grains and these two ideas are not mutually exclusive. Further work is needed to test both hypotheses. Most critical are experiments where nuclei can be observed whilst they are very small and subsequent misorientations can be documented, as might be possible with 3-D microscopy methods (Lauridsen et al., 2003; Poulson et al., 2004), and experiments where fiducial

markers are used to confirm the physical existence of offsets on grain boundaries (Schmid et al, 1977; Spiers, 1979 ; Beeré, 1978; Drury and Humphreys, 1988; Ree, 1994; Maruyama and Hiraga, 2017; Eleti et al., 2020).

4.2 Future work: implications for enhancement (weakening)

The mechanical weakening, i.e. stress drop after peak in constant strain rate experiments and strain rate enhancement from secondary to tertiary creep in constant load experiments, has been associated with: (1) the softening owing to the reduction of stored strain energy by dynamic recrystallisation processes such as nucleation and grain boundary migration (Duval, 1979; Weertman, 1983; Derby and Ashby, 1987; Humphreys and Hatherley, 2008; Rollett et al 2017), (2) increased contribution of grain size sensitive deformation mechanisms due to grain size reduction resulting from dynamic recrystallization (De Bresser et al., 2001), and (3) development of strong CPO in viscously anisotropic materials (Durham and Goetze, 1977; Hansen et al., 2012) such as ice. The microstructural data as discussed in section 4.1 will enable us to comment on the potential contribution of different mechanisms to the weakening in deformed polycrystalline ice.

All experiments show weakening after peak stress (Fig. 3). The percentage of stress drop from peak to flow stress is similar between high and low temperatures. Weakening is classically observed during dynamic recrystallization; the mechanical evolution from peak to flow stress in constant displacement rate experiments or from secondary to tertiary creep stage in constant load experiments was attributed to a balance between processes favouring strain hardening (e.g. accumulation of stored strain energy through dislocation) and weakening (e.g. reduction of stored strain energy through dynamic recrystallisation) (Duval, 1979; Weertman, 1983; Derby and Ashby, 1987; Humphreys and Hatherley, 2008). In this study, mean and median ice grain size reduces with strain at all temperatures (Table 3, Fig. 11(a)). Grain size is commonly reduced during rock deformation in the laboratory (e.g. Pieri et al., 2001; Hansen et al., 2012) and in nature (Trimby et al., 1998; Bestmann and Prior, 2003). At smaller grain sizes the strain-rate contribution of grain size sensitive (GSS) mechanisms increases or the stress required to drive a given strain rate contribution of GSS decreases. For this reason, grain size reduction has been proposed as a weakening mechanism (Rutter and Brodie, 1988; De Bresser et al 2001; Kilian et al., 2011; Campbell and Menegon, 2019). On the other hand, many published papers on ice sheet mechanics imply that enhancement (weakening) is caused by anisotropy development and there are analytical numerical models that seek to quantify this relationship (Azuma, 1995; Morland and Staroszczyk, 2009; Placidi et al., 2010). At -10 °C, the CPO development includes many grains with basal plane orientations that would facilitate further axial shortening and it is intuitive that CPO development could provide a cause for the weakening. However, at -30 °C the CPO developed at high strain is a narrow cone or cluster with many basal planes sub-perpendicular to compression. Therefore, further studies are required to quantify the contribution of candidate weakening (enhancement) mechanisms including (1) dynamic recrystallisation processes such as nucleation and GBM, (2) grain size reduction and the resulting contribution of GBS, (3) CPO development to the mechanical weakening observed during ice deformation.

5 Conclusions

1. We deformed isotropic polycrystalline pure water ice to successive strains (~3%, 5%, 8%, 12% and 20%) under a constant displacement rate (strain rate $\sim 1.0 \times 10^{-5} s^{-1}$) at -10, -20 and -30 °C. For all deformed samples, stress first rises to a peak at ~1-4% strain and then drops to lower stresses at higher strains. Samples deformed at colder temperatures show higher peak and final stresses, as expected for the temperature dependency of creep. Microstructural and CPO analyses were conducted on deformed ice samples using cryo-EBSD.

2. All deformed samples develop distinct subgrain boundaries and show a peak at 2°-3° in the neighbour-pair misorientation angle distribution. Mean/median subgrain size is smaller than mean/median grain size. These observations suggest that dislocation glide and associated recovery and subgrain rotation were active in all deformed samples. Neighbour-pair low-angle (5°-10°) misorientation axes show primary maxima lying in the basal plane, for all samples, suggesting that basal glide dominated intragranular deformation processes. Subgrain boundary misorientation distributions extend to higher misorientation angles with strain and with decreasing temperature, suggesting that subgrain rotation develops progressively and is more effective at lower temperatures.

3. All deformed samples have skewed grain size distributions with a strong peak at small (<100 μm) sizes and a tail to larger sizes. The grain size peak is smaller than the grain size of the starting material (~297 μm) and a stereological analysis suggests that many of the small grains, measured in 2-D, are also small in 3-D. The number density of "distinct" grains (counting 2-D grains that are out of the analysis plane to the same 3-D grain) is more than 3 times that in the starting material for all deformed samples and the number density increases with strain. These data indicate that nucleation is involved in dynamic recrystallization. "Core-and-mantle" structures (small grains surrounding larger grains) are observed at high strains and are clearest at -20 and -30 °C, suggesting that subgrain rotation recrystallization has occurred and is more important at lower temperatures. Lobate grain boundaries suggest that strain-induced grain boundary migration has occurred in all samples.

4. Many of the deformed samples have CPOs defined by open cones (small circles) of *c*-axes. The cone opening-angle decreases with strain. The CPO intensity and *c*-axis opening-angle both decrease as the temperature drops from -10 to -30 °C. At -30 °C and 20% strain the *c*-axes define a cluster with maximum parallel to compression, rather than an open cone. We interpret that the open *c*-axis cone develops because strain-induced GBM favours the growth of grains in easy slip orientations. The closure of the *c*-axes cone with strain is interpreted primarily as the result of grain rotation related to intragranular dislocation glide on the basal plane. We infer that grain rotation becomes more prominent at lower temperatures, whilst GBM is more widespread at higher temperatures.

5. Small grains have a weaker CPO than large grains. This distinction is slight at -10 °C, but becomes much clearer at lower temperatures. Neighbour-pair high-angle ($\geq 10°$) misorientation axes, corresponding to grain boundaries are not strongly aligned in the basal plane, nor with any other crystal direction. An additional process is needed to explain these

observations. We identify two candidate processes; (1) grain boundary sliding causing rotation of grains without crystallographic control on the rotation axes, and (2) nucleation of grains with random orientations.

Competing interests. The authors declare that they have no conflict of interest.

Data availability. Data available on request from the authors.

References

Ajaja, O.: Role of recovery in high temperature constant strain rate deformation, J Mater Sci, 26, 6599–6605, https://doi:10.1007/BF02402651, 1991.

Alley, R. B.: Flow-law hypotheses for ice-sheet modeling, J. Glaciol., 38, 245–256, https://doi.org/10.1017/s0022143000003658, 1992.

Austin, N. J. and Evans, B.: Paleowattmeters: A scaling relation for dynamically recrystallized grain size, Geology, 35, 343–4, https://doi.org/10.1130/g23244a.1, 2007.

Azuma, N.: A flow law for anisotropic polycrystalline ice under uniaxial compressive deformation, Cold Regions Science and Technology, 23, 137–147, https://doi.org/10.1016/0165-232x(94)00011-l, 1995.

Bachmann, F., Hielscher, R., and Schaeben, H.: Grain detection from 2-D and 3-D EBSD data—Specification of the MTEX algorithm, Ultramicroscopy, 111, 1720-1733, https://doi.org/10.1016/j.ultramic.2011.08.002, 2011.

Bailey, J. E. and Hirsch, P. B.: The dislocation distribution, flow stress, and stored energy in cold-worked polycrystalline silver, Philosophical Magazine, 5, 485–497, https://doi.org/10.1080/14786436008238300, 1960.

Bamber, J. L., Oppenheimer, M., Kopp, R. E., Aspinall, W. P., and Cooke, R. M.: Ice sheet contributions to future sea-level rise from structured expert judgment, Proceedings of the National Academy of Sciences of the United States of America, 116, 11195-11200, https://doi.org/10.1073/pnas.1817205116, 2019.

Beeré, W.: Stresses and deformation at grain boundaries, Philosophical Transactions of the Royal Society of London. Series A, Mathematical and Physical Sciences, 288(1350), 177–196, https://doi.org/10.1098/rsta.1978.0012, 1978.

Berger, A., Herwegh, M., Schwarz, J.-O. and Putlitz, B.: Quantitative analysis of crystal/grain sizes and their distributions in 2D and 3D, Journal of Structural Geology, 33, 1751–1763, https://doi.org/10.1016/j.jsg.2011.07.002, 2011.

Bestmann, M. and Prior, D. J.: Intragranular dynamic recrystallization in naturally deformed calcite marble: diffusion accommodated grain boundary sliding as a result of subgrain rotation recrystallization, Journal of Structural Geology, 25, 1597-1613, https://doi.org/10.1016/s0191-8141(03)00006-3, 2003.

Bindschadler, R. A., Nowicki, S., Abe-Ouchi, A., Aschwanden, A., Choi, H., Fastook, J., Granzow, G., Greve, R., Gutowski, G., Herzfeld, U., Jackson, C., Johnson, J., Khroulev, C., Levermann, A., Lipscomb, W. H., Martin, M. A., Morlighem, M., Parizek, B. R., Pollard, D., Price, S. F., Ren, D. D., Saito, F., Sato, T., Seddik, H., Seroussi, H., Takahashi, K., Walker, R., and Wang, W. L.: Ice-sheet model sensitivities to environmental forcing and their use in projecting future sea level (the SeaRISE project), Journal of Glaciology, 59, 195-224, https://doi.org/10.3189/2013jog12j125, 2013.

Budd, W. F. and Jacka, T. H.: A review of ice rheology for ice sheet modelling, Cold Regions Science and Technology, 16, 107-144, https://doi.org/10.1016/0165-232x(89)90014-1, 1989.

Budd, W. F., Warner, R. C., Jacka, T. H., Li, J. and Treverrow, A.: Ice flow relations for stress and strain-rate components from combined shear and compression laboratory experiments, Journal of Glaciology, 59(214), 374–392, https://doi.org/10.3189/2013jog12j106, 2013.

Campbell, L. R. and Menegon, L.: Transient High Strain Rate During Localized Viscous Creep in the Dry Lower Continental Crust (Lofoten, Norway), Journal of Geophysical Research: Solid Earth, 124, 10240–10260, https://doi.org/10.1029/2019jb018052, 2019.

Castelnau, O., Duval, P., Lebensohn, R. A. and Canova, G. R.: Viscoplastic modeling of texture development in polycrystalline ice with a self-consistent approach: Comparison with bound estimates, Journal of Geophysical Research: Solid Earth, 101 13851–13868, https://doi.org/10.1029/96JB00412, 1996.

Castelnau, O., Duval, P., Montagnat, M. and Brenner, R.: Elastoviscoplastic micromechanical modeling of the transient creep of ice, Journal of Geophysical Research, 113(B11), 749–14, https://doi.org/10.1029/2008JB005751, 2008.

Chauve, T., Montagnat, M., Barou, F., Hidas, K., Tommasi, A. and Mainprice, D.: Investigation of nucleation processes during dynamic recrystallization of ice using cryo-EBSD, Phil. Trans. R. Soc. A, 375 20150345–20, https://doi.org/10.1098/rsta.2015.0345, 2017.

Craw, L., Qi, C., Prior, D. J., Goldsby, D. L., and Kim, D.: Mechanics and microstructure of deformed natural anisotropic ice, J. Struct. Geol., 115, 152–166, https://doi.org/10.1016/j.jsg.2018.07.014, 2018.

Cross, A. J., Prior, D. J., Stipp, M. and Kidder, S.: The recrystallized grain size piezometer for quartz: An EBSD-based calibration, Geophysical Research Letters, 44, 6667–6674, https://doi.org/10.1002/2017gl073836, 2017a.

Cross, A. J., Hirth, G. and Prior, D. J.: Effects of secondary phases on crystallographic preferred orientations in mylonites, Geology, 45, 955–958, https://doi.org/10.1130/g38936.1, 2017b.

5   Cole, D. M.: Preparation of polycrystalline ice specimens for laboratory experiments, Cold Regions Science and Technology, 1, 153-159, https://doi.org/10.1016/0165-232x(79)90007-7, 1979.

Cuffey, K.M. and Paterson, W.S.B. (4th Eds.): The Physics of Glaciers, Butterworth-Heinemann, Elsevier, U.S.A., 2010.

De Bresser, J., Ter Heege, J., and Spiers, C.: Grain size reduction by dynamic recrystallization: can it result in major rheological weakening?, Int. J. Earth Sci., 90, 28–45, https://doi.org/10.1007/s005310000149, 2001.

10   Derby, B. and Ashby, M. F.: On dynamic recrystallization, Scripta Metallurgica, 21(6), 879–884, https://doi.org/10.1016/0036-9748(87)90341-3, 1987.

Derby, B.: The dependence of grain size on stress during dynamic recrystallisation, Acta Metallurgica et Materialia, 39, 955–962, https://doi.org/10.1016/0956-7151(91)90295-c, 1991.

Drury, M. R. and Humphreys, F. J.: Microstructural shear criteria associated with grain-boundary sliding during ductile

15   deformation, Journal of Structural Geology, 10(1), 83–89, https://doi.org/10.1016/0191-8141(88)90130-7, 1988.

Dutton, A., Carlson, A. E., Long, A. J., Milne, G. A., Clark, P. U., DeConto, R., Horton, B. P., Rahmstorf, S., and Raymo, M. E.: Sea-level rise due to polar ice-sheet mass loss during past warm periods, Science, 349, 153, https://doi.org/10.1126/science.aaa4019, 2015.

Durham, W. B. and Goetze, C.: Plastic flow of oriented single crystals of olivine: 1. Mechanical data, Journal of geophysical

20   Research, 82, 5737-5753, https://doi.org/10.1029/jb082i036p05737, 1977.

Durham, W. B., Heard, H. C., and Kirby, S. H.: Experimental deformation of polycrystalline H2O ice at high pressure and low temperature: Preliminary results, Journal of Geophysical Research: Solid Earth, 88, B377-B392, https://doi.org/10.1029/jb088is01p0b377, 1983.

Durham, W. B., Kirby, S. H., and Stern, L. A.: Effects of dispersed particulates on the rheology of water ice at planetary

25   conditions, Journal of Geophysical Research: Planets, 97, 20883-20897, https://doi.org/10.1029/92je02326, 1992.

Durham, W. B., Prieto-Ballesteros, O., Goldsby, D. L., and Kargel, J. S.: Rheological and Thermal Properties of Icy Materials, Space Science Reviews, 153, 273-298, https://doi.org/10.1007/s11214-009-9619-1, 2010.

Duval, P.: Creep and recrystallization of polycrystalline ice, bulmi, 102, 80–85, https://doi.org/10.3406/bulmi.1979.7258, 1979.

30   Duval, P., Ashby, M. F., and Anderman, I.: Rate-controlling processes in the creep of polycrystalline ice, J. Phys. Chem., 87, 4066–4074, https://doi.org/10.1021/j100244a014, 1983.

Duval, P.: Grain Growth and Mechanical Behaviour of Polar Ice, Annals of Glaciology, 6, 79–82, https://doi.org/10.3189/1985AoG6-1-79-82, 1985.

Duval, P. and Castelnau, O.: Dynamic recrystallization of ice in polar ice sheets, J. Phys. IV, 05, C3–197–C3–205, https://doi:10.1051/jp4:1995317, 1995.

Duval, P., Montagnat, M., Grennerat, F., Weiss, J., Meyssonnier, J., and Philip, A.: Creep and plasticity of glacier ice: a material science perspective, Journal of Glaciology, 56, 1059–1068, https://doi.org/10.3189/002214311796406185, 2010.

5   Eleti, R. R., Chokshi, A. H., Shibata, A., and Tsuji, N.: Unique high-temperature deformation dominated by grain boundary sliding in heterogeneous necklace structure formed by dynamic recrystallization in HfNbTaTiZr BCC refractory high entropy alloy, Acta Materialia, 183, 64–77, https://doi.org/10.1016/j.actamat.2019.11.001, 2020.

Falus, G., Tommasi, A. and Soustelle, V.: The effect of dynamic recrystallization on olivine crystal preferred orientations in mantle xenoliths deformed under varied stress conditions, Journal of Structural Geology, 33(11), 1528–1540, 10   https://doi.org/10.1016/j.jsg.2011.09.010, 2011.

Faria, S. H., Weikusat, I., and Azuma, N.: The microstructure of polar ice. Part II: State of the art, Journal of Structural Geology, 61, 21–49, https://doi.org/10.1016/j.jsg.2013.11.003, 2014.

Fliervoet, T. F., Drury, M. R., and Chopra, P. N., Crystallographic preferred orientations and misorientations in some olivine rocks deformed by diffusion or dislocation creep: Tectonophysics, 303, 1-27, https://doi.org/10.1016/s0040-15   1951(98)00250-9, 1999.

Gammon, P. H., Kiefte, H., Clouter, M. J., and Denner, W. W.: Elastic constants of artificial and natural ice samples by Brillouin spectroscopy, Journal of glaciology, 29, 433-460, https://doi.org/10.3189/s0022143000030355, 1983.

Gao, X. Q. and Jacka, T. H.: The approach to similar tertiary creep rates for antarctic core ice and laboratory prepared ice, J. Phys. Colloques, 48, C1–289–C1–296, https://doi:10.1051/jphyscol:1987141, 1987.

20   Gifkins, R.: Grain-boundary sliding and its accommodation during creep and superplasticity, Metallurgical transactions a, 7, 1225-1232, https://doi.org/10.1007/bf02656607, 1976.

Glen, J. W.: The creep of polycrystalline ice. Proceedings of the Royal Society of London. Series A. Mathematical and Physical Sciences, 228, 519-538, https://doi.org/10.1098/rspa.1955.0066, 1955.

Goldsby, D. L. and Kohlstedt, D. L.: Grain boundary sliding in fine-grained ice I, Scripta Materialia, 37, 1399-1406, 25   https://doi.org/10.1016/s1359-6462(97)00246-7, 1997.

Goldsby, D. L. and Kohlstedt, D. L.: Superplastic deformation of ice: Experimental observations, Journal of Geophysical Research: Solid Earth, 106, 11017-11030, https://doi.org/10.1029/2000jb900336, 2001.

Gomez-Rivas, E., Griera, A., Llorens, M. G., Bons, P. D., Lebensohn, R. A., and Piazolo, S.: Subgrain rotation recrystallization during shearing: insights from full-field numerical simulations of halite polycrystals, Journal of Geophysical Research: 30   Solid Earth, 122, 8810-8827, https://doi.org/10.1002/2017jb014508, 2017.

Grennerat, F., Montagnat, M., Castelnau, O., Vacher, P., Moulinec, H., Suquet, P. and Duval, P.: Experimental characterization of the intragranular strain field in columnar ice during transient creep, Acta Materialia, 60, 3655–3666, https://doi.org/10.1016/j.actamat.2012.03.025, 2012.

26

Grimmer, H.: The distribution of disorientation angles if all relative orientations of neighbouring grains are equally probable, Scripta Metallurgica, 13, 161–164, https://doi.org/10.1016/0036-9748(79)90058-9, 1979.

Guillope, M. and Poirier, J. P.: Dynamic recrystallization during creep of single-crystalline halite: An experimental study, Journal of Geophysical Research: Solid Earth, 84, 5557-5567, https://doi.org/10.1029/jb084ib10p05557, 1979.

5 Halfpenny, A., Prior, D. J., and Wheeler, J.: Analysis of dynamic recrystallization and nucleation in a quartzite mylonite, Tectonophysics, 427, 3-14, https://doi.org/10.1016/j.tecto.2006.05.016, 2006.

Hansen, L. N., Zimmerman, M. E., and Kohlstedt, D. L.: The influence of microstructure on deformation of olivine in the grain-boundary sliding regime, J. Geophys. Res., 117, B09201, https://doi.org/10.1029/2012JB009305, 2012.

Hartmann, W. K.: Surface evolution of two-component stone / ice bodies in the Jupiter region, Icarus, 44, 441-453, 10 https://doi.org/10.1016/0019-1035(80)90036-6, 1980.

Hasegawa, M. and Fukutomi, H.: Microstructural Study on Dynamic Recrystallization and Texture Formation in Pure Nickel, Mater. Trans., 43(5), 1183–1190, https://doi.org/10.2320/matertrans.43.1183, 2002.

Hasegawa, M., Yamamoto, M. and Fukutomi, H.: Formation mechanism of texture during dynamic recrystallization in γ-TiAl, nickel and copper examined by microstructure observation and grain boundary analysis based on local orientation 15 measurements, Acta Materialia, 51(13), 3939–3950, https://doi.org/10.1016/S1359-6454(03)00218-0, 2003.

Heard, H. C., Durham, W. B., Boro, C. O., and Kirby, S. H.: A triaxial deformation apparatus for service at 77 ≤T≤ 273 K, in: The Brittle-Ductile Transition in Rocks, edited by: Duba, A. G., Durham, W. B., Handin, J. W., and Wang, H. F., 225–228, https://doi.org/10.1029/GM056p0225, 1990.

Hidas, K., Tommasi, A., Mainprice, D., Chauve, T., Barou, F. and Montagnat, M.: Microstructural evolution during thermal 20 annealing of ice-Ih, Journal of Structural Geology, 99, 31–44, https://doi.org/10.1016/j.jsg.2017.05.001, 2017.

Hirth, G., and Tullis, J.: Dislocation creep regimes in quartz aggregates, Journal of structural geology, 14, 145-159, https://doi.org/10.1016/0191-8141(92)90053-y, 1992.

Hobbs, B. E., Means, W. D., and Williams, P. F. (1st Eds.): An outline of structural geology, Wiley, 1976.

Homer, D. R. and Glen, J. W.: The creep activation energies of ice, Journal of Glaciology, 21, 429-444, 25 https://doi.org/10.1017/s0022143000033591, 1978.

Hondoh, T. and Higashi, A.: Generation and absorption of dislocations at large-angle grain boundaries in deformed ice crystals, The Journal of Physical Chemistry, 87(21), 4044–4050, https://doi.org/10.1021/j100244a009, 1983.

Hooke, R. L. and Hudleston, P. J.: Ice Fabrics in a Vertical Flow Plane, Barnes Ice Cap, Canada, Journal of Glaciology, 25(92), 195–214, doi:10.3189/S0022143000010443, 1980.

30 Hooke, R. L. and Hudleston, P. J.: Ice fabrics from a borehole at the top of the south dome, Barnes Ice Cap, Baffin Island, Geological Society of America Bulletin, 92(5), 274–281, https://doi.org/10.1130/0016-7606(1981)92<274:iffaba>2.0.co;2, 1981.

Hudleston, P.J.: Structures and fabrics in glacial ice: a review, J. Struct. Geol., 81, 1–27, https://doi.org/10.1016/j.jsg.2015.09.003, 2015.

27

Humphreys, F. J. and Hatherly, M. (2nd Eds.): Recrystallization and related annealing phenomena, Elsevier, 2008.

Iliescu, D., Baker, I. and Chang, H.: Determining the orientations of ice crystals using electron backscatter patterns, Microsc. Res. Tech., 63(4), 183–187, https://doi.org/10.1002/jemt.20029, 2004.

Jacka, T. H. and Maccagnan, M.: Ice crystallographic and strain rate changes with strain in compression and extension, Cold Regions Science and Technology, 8(3), 269–286, https://doi.org/10.1016/0165-232x(84)90058-2, 1984.

Jacka, T. H. and Li, J.: The steady-state crystal size of deforming ice, Annals of Glaciology, 20, 13-18, https://doi.org/10.3189/172756494794587230, 1994.

Jacka, T. H. and Li, J.: Flow rates and crystal orientation fabrics in compression of polycrystalline ice at low temperatures and stresses, in: International Symposium on Physics of Ice Core Records, Shikotsukohan, Hokkaido, Japan, 14–17 September 1998, edited by: Hondoh, T., 83–102, 2000.

Jafari, M. and Najafizadeh, A.: Correlation between Zener–Hollomon parameter and necklace DRX during hot deformation of 316 stainless steel, Materials Science and Engineering A, 501, 16–25, https://doi.org/10.1016/j.msea.2008.09.073, 2009.

Jessell, M. W.: Grain boundary migration and fabric development in experimentally deformed octachloropropane, Journal of Structural Geology, 8, 527–542, https://doi.org/10.1016/0191-8141(86)90003-9, 1986.

Jiang, Z., Prior, D. J., and Wheeler, J.: Albite crystallographic preferred orientation and grain misorientation distribution in a low-grade mylonite: implications for granular flow, Journal of Structural Geology, 22, 1663-1674, https://doi.org/10.1016/s0191-8141(00)00079-1, 2000.

Journaux, B., Chauve, T., Montagnat, M., Tommasi, A., Barou, F., Mainprice, D. and Gest, L.: Recrystallization processes, microstructure and crystallographic preferred orientation evolution in polycrystalline ice during high-temperature simple shear, The Cryosphere, 13, 1495–1511, https://doi.org/10.5194/tc-13-1495-2019, 2019.

Kamb, W. B.: Ice petrofabric observations from Blue Glacier, Washington, in relation to theory and experiment, Journal of Geophysical Research, 64, 1891–1909, https://doi:10.1029/JZ064i011p01891, 1959.

Kamb, W. B.: Experimental recrystallization of ice under stress, in: Flow and Fracture of Rocks, edited by Heard, H. C., Borg, I. Y., Carter, N. L., and Rayleigh, C. B., American Geophysical Union, 211–242, https://doi.org/10.1029/gm016p0211, 1972.

Kamb, B.: Basal Zone of the West Antarctic Ice Streams and its Role in Lubrication of Their Rapid Motion, in: Antarctic Research Series, American Geophysical Union (AGU), edited by: Alley, R. B., Bindschadle, R. A., Washington, D. C., USA, 157-199, https://doi.org/10.1029/AR077p0157, 2008.

Kilian, R., Heilbronner, R., and Stünitz, H.: Quartz grain size reduction in a granitoid rock and the transition from dislocation to diffusion creep, Journal of Structural Geology, 33, 1265-1284, https://doi.org/10.1016/j.jsg.2011.05.004, 2011.

Kirby, S. H., Durham, W. B., Beeman, M. L., Heard, H. C. and Daley, M. A.: Inelastic properties of ice 1h at low temperatures and high pressures, J. Phys. Colloques, 48, C1–227–C1–232, https://doi.org/10.1051/jphyscol:1987131, 1987.

Kopp, R. E., DeConto, R. M., Bader, D. A., Hay, C. C., Horton, R. M., Kulp, S., Oppenheimer, M., Pollard, D. and Strauss, B. H.: Evolving Understanding of Antarctic Ice-Sheet Physics and Ambiguity in Probabilistic Sea-Level Projections, Earth's Future, 5, 1217–1233, https://doi.org/10.1002/2017ef000663, 2017.

Kuiper, E.-J. N., Weikusat, I., de Bresser, J. H. P., Jansen, D., Pennock, G. M. and Drury, M. R.: Using a composite flow law to model deformation in the NEEM deep ice core, Greenland – Part 1: The role of grain size and grain size distribution on deformation of the upper 2207 m, The Cryosphere, 14(7), 2429–2448, https://doi.org/10.5194/tc-14-2429-2020, 2020.

Kuiper, E.-J. N., de Bresser, J. H. P., Drury, M. R., Eichler, J., Pennock, G. M. and Weikusat, I.: Using a composite flow law to model deformation in the NEEM deep ice core, Greenland – Part 2: The role of grain size and premelting on ice deformation at high homologous temperature, The Cryosphere, 14(7), 2449–2467, https://doi.org/10.5194/tc-14-2449-2020, 2020.

Lallemant, H. G. A.: Subgrain rotation and dynamic recrystallization of olivine, upper mantle diapirism, and extension of the Basin-and-Range Province, Tectonophysics, 119, 89-117, https://doi.org/10.1016/0040-1951(85)90034-4, 1985.

Langdon, T. G.: A unified approach to grain boundary sliding in creep and superplasticity, Acta Metallurgica et Materialia, 42, 2437–2443, https://doi.org/10.1016/0956-7151(94)90322-0, 1994.

Langdon, T. G.: Grain boundary sliding revisited: Developments in sliding over four decades, J Mater Sci, 41, 597–609, https://doi.org/10.1007/s10853-006-6476-0, 2006.

Langdon, T. G.: Seventy-five years of superplasticity: historic developments and new opportunities, J Mater Sci, 44, 5998–6010, https://doi.org/10.1007/s10853-009-3780-5, 2009.

Lauridsen, E. M., Poulsen, H. F., Nielsen, S. F. and Juul Jensen, D.: Recrystallization kinetics of individual bulk grains in 90% cold-rolled aluminium, Acta Materialia, 51, 4423–4435, https://doi.org/10.1016/s1359-6454(03)00278-7, 2003.

Little, T. A., Prior, D. J., Toy, V. G. and Lindroos, Z. R.: The link between strength of lattice preferred orientation, second phase content and grain boundary migration: A case study from the Alpine Fault zone, New Zealand, Journal of Structural Geology, 81(C), 59–77, https://doi.org/10.1016/j.jsg.2015.09.004, 2015.

Liu, F., Baker, I. and Dudley, M.: Dynamic observations of dislocation generation at grain boundaries in ice, Philosophical Magazine A, 67(5), 1261–1276, https://doi.org/10.1080/01418619308224770, 1993.

Liu, F., Baker, I. and Dudley, M.: Dislocation-grain boundary interactions in ice crystals, Philosophical Magazine A, 71(1), 15–42, https://doi.org/10.1080/01418619508242954, 1995.

Llorens, M.-G., Griera, A., Bons, P. D., Roessiger, J., Lebensohn, R., Evans, L. and Weikusat, I.: Dynamic recrystallisation of ice aggregates during co-axial viscoplastic deformation: a numerical approach, Journal of Glaciology, 62, 1–19, https://doi.org/10.1017/jog.2016.28, 2016.

Lopez-Sanchez, M. A. and Llana-Fúnez, S.: An evaluation of different measures of dynamically recrystallized grain size for paleopiezometry or paleowattometry studies, Solid Earth, 6, 475-495, https://doi.org/10.5194/se-6-475-2015, 2015.

MacDonald, J. M., Wheeler, J., Harley, S. L., Mariani, E., Goodenough, K. M., Crowley, Q. and Tatham, D.: Lattice distortion in a zircon population and its effects on trace element mobility and U–Th–Pb isotope systematics: examples from the

Lewisian Gneiss Complex, northwest Scotland, Contrib Mineral Petrol, 166, 21–41, https://doi.org/10.1007/s00410-013-0863-8, 2013.

Mainprice, D., Bachmann, F., Hielscher, R., and Schaeben, H.: Descriptive tools for the analysis of texture projects with large datasets using MTEX: strength, symmetry and components, Geological Society, London, Special Publications, 409, 251-271, https://doi.org/10.1144/sp409.8, 2015.

Maruyama, G. and Hiraga, T.: Grain- to multiple-grain-scale deformation processes during diffusion creep of forsterite + diopside aggregate: 1. Direct observations, Journal of Geophysical Research: Solid Earth, 122(8), 5890–5915, https://doi.org/10.1002/2017jb014254, 2017.

Mellor, M. and Cole, D. M.: Deformation and failure of ice under constant stress or constant strain-rate, Cold Regions Science and Technology, 5, 201-219, https://doi.org/10.1016/0165-232x(82)90015-5, 1982.

Mellor, M. and Cole, D. M.: Stress/strain/time relations for ice under uniaxial compression, Cold Regions Science and Technology, 6, 207–230, https://doi.org/10.1016/0165-232x(83)90043-5, 1983.

Montagnat, M., Azuma, N., Dahl-Jensen, D., Eichler, J., Fujita, S., Gillet-Chaulet, F., Kipfstuhl, S., Samyn, D., Svensson, A. and Weikusat, I.: Fabric along the NEEM ice core, Greenland, and its comparison with GRIP and NGRIP ice cores, The Cryosphere, 8, 1129–1138, https://doi.org/10.5194/tc-8-1129-2014, 2014.

Montagnat, M., Chauve, T., Barou, F., Tommasi, A., Beausir, B., and Fressengeas, C.: Analysis of dynamic recrystallization of ice from EBSD orientation mapping, Frontiers in Earth Science, 3, 81, https://doi.org/10.3389/feart.2015.00081, 2015.

Monz, M. E., Hudleston, P. J., Prior, D. J., Michels, Z., Fan, S.., Negrini, M., and Langhorne, P.: Electron backscatter diffraction (EBSD) based determination of crystallographic preferred orientation (CPO) in warm, coarse-grained ice: a case study, Storglaciären, Sweden, The Cryosphere Discuss, https://doi.org/10.5194/tc-2020-135, 2020.

Morawiec, A.: Misorientation-Angle Distribution of Randomly Oriented Symmetric Objects, J Appl Crystallogr, 28, 289–293, https://doi.org/10.1107/s0021889894011088, 1995.

Morland, L. W. and Staroszczyk, R.: Ice viscosity enhancement in simple shear and uni-axial compression due to crystal rotation, International Journal of Engineering Science, 47, 1297–1304, https://doi.org/10.1016/j.ijengsci.2008.09.011, 2009.

Obbard, R., Baker, I. and Sieg, K.: Using electron backscatter diffraction patterns to examine recrystallization in polar ice sheets, Journal of Glaciology, 52, 546–557, https://doi.org/10.3189/172756506781828458, 2006.

Passchier, C. W. and Trouw, R. A. (2nd Eds.): Microtectonics, Springer Science and Business Media, 2005.

Peternell, M., Dierckx, M., Wilson, C. J. L. and Piazolo, S.: Quantification of the microstructural evolution of polycrystalline fabrics using FAME: Application to in situ deformation of ice, Journal of Structural Geology, 61, 109–122, https://doi.org/10.1016/j.jsg.2013.05.005, 2014.

Peternell, M. and Wilson, C. J. L.: Effect of strain rate cycling on microstructures and crystallographic preferred orientation during high-temperature creep, Geology, 44, 279–282, https://doi.org/10.1130/g37521.1, 2016.

Piazolo, S., Bestmann, M., Prior, D. J., and Spiers, C. J.: Temperature dependent grain boundary migration in deformed-then-annealed material: observations from experimentally deformed synthetic rocksalt, Tectonophysics, 427, 55-71, https://doi.org/10.1016/j.tecto.2006.06.007, 2006.

Piazolo, S., Montagnat, M. and Blackford, J. R.: Sub-structure characterization of experimentally and naturally deformed ice using cryo-EBSD, Journal of Microscopy, 230, 509–519, https://doi.org/10.3189/172756506781828458, 2008.

Piazolo, S., Wilson, C. J., Luzin, V., Brouzet, C., and Peternell, M.: Dynamics of ice mass deformation: Linking processes to rheology, texture, and microstructure, Geochemistry, Geophysics, Geosystems, 14, 4185-4194, https://doi.org/10.1002/ggge.20246, 2013.

Pieri, M., Burlini, L., Kunze, K., Stretton, I. and Olgaard, D. L.: Rheological and microstructural evolution of Carrara marble with high shear strain: results from high temperature torsion experiments, Journal of Structural Geology, 23, 1393–1413, https://doi.org/10.1016/s0191-8141(01)00006-2, 2001.

Placidi, L., Greve, R., Seddik, H. and Faria, S. H.: Continuum-mechanical, Anisotropic Flow model for polar ice masses, based on an anisotropic Flow Enhancement factor, Continuum Mech. Thermodyn., 22, 221–237, https://doi.org/10.1007/s00161-009-0126-0, 2010.

Poirier, J. P.: High-temperature creep of single crystalline sodium chloride, The Philosophical Magazine: A Journal of Theoretical Experimental and Applied Physics, 26(3), 701–712, https://doi.org/10.1080/14786437208230114, 1972.

Poirier, J. P. and Nicolas, A.: Deformation-induced recrystallization due to progressive misorientation of subgrains, with special reference to mantle peridotites, The Journal of Geology, 83, 707-720, https://doi.org/10.1086/628163, 1975.

Pollard, D.: A retrospective look at coupled ice sheet–climate modeling, Climatic Change, 100, 173–194, https://doi.org/10.1007/s10584-010-9830-9, 2010.

Ponge, D. and Gottstein, G.: Necklace formation during dynamic recrystallization: Mechanisms and impact on flow behavior, Acta Materialia, 46, 69–80, https://doi.org/10.1016/s1359-6454(97)00233-4, 1998.

Prior, D.J., Lilly, K., Seidemann, M., Vaughan, M., Becroft, L., Easingwood, R., Diebold, S., Obbard, R., Daghlian, C., Baker, I., and Caswell, T.: Making EBSD on water ice routine, Journal of microscopy, 259, 237-256, https://doi.org/10.1111/jmi.12258, 2015.

Qi, C., Goldsby, D. L., and Prior, D. J.: The down-stress transition from cluster to cone fabrics in experimentally deformed ice, Earth Planet. Sc. Lett., 471, 136–147, https://doi.org/10.1016/j.epsl.2017.05.008, 2017.

Qi, C., Prior, D.J., Craw, L., Fan, S., Llorens, M.G., Griera, A., Negrini, M., Bons, P.D., and Goldsby, D.L.: Crystallographic preferred orientations of ice deformed in direct-shear experiments at low temperatures, The Cryosphere, 13, 351-371, https://doi.org/10.5194/tc-13-351-2019, 2019.

Raj, R. and Ashby, M. F.: On grain boundary sliding and diffusional creep, Metallurgical Transactions, 2, 1113–1127, https://doi:10.1007/BF02664244, 1971.

Read, W. T. and Shockley, W.: Dislocation Models of Crystal Grain Boundaries, Phys. Rev., 78(3), 275–15, https://doi.org/10.1103/PhysRev.78.275, 1950.

Ree, J. H.: Grain boundary sliding and development of grain boundary openings in experimentally deformed octachloropropane, Journal of Structural Geology, 16(3), 403–418, https://doi.org/10.1016/0191-8141(94)90044-2, 1994.

Rignot, E., Mouginot, J., and Scheuchl, B.: Ice flow of the Antarctic ice sheet, Science, 333, 1427-1430, https://doi.org/10.1126/science.1208336, 2011.

5   Rollett, A. D., Rohrer, G. S., and Humphreys, F. J., (3rd Eds.), Recrystallization and Related Annealing Phenomena, Elsevier Science, 2017.

Rutter, E. H. and Brodie, K. H.: The role of tectonic grain size reduction in the rheological stratification of the lithosphere, Geol Rundsch, 77, 295–307, https://doi.org/10.1007/bf01848691, 1988.

Scapozza, C. and Bartelt, P. A.: The influence of temperature on the small-strain viscous deformation mechanics of snow: a
10   comparison with polycrystalline ice, Annals of Glaciology, 37, 90-96, https://doi.org/10.3189/172756403781815410, 2003.

Schmid, S. M., Boland, J. N. and Paterson, M. S.: Superplastic flow in finegrained limestone, Tectonophysics, 43, 257-291, https://doi.org/10.1016/0040-1951(77)90120-2, 1977.

Seidemann, M., Prior, D. J., Golding, N., Durham, W. B., Lilly, K., and Vaughan, M. J.: The role of kink boundaries in the
15   deformation and recrystallisation of polycrystalline ice, Journal of Structural Geology, 136, 104010, https://doi.org/10.1016/j.jsg.2020.104010, 2020.

Shigematsu, N., Prior, D. J. and Wheeler, J.: First combined electron backscatter diffraction and transmission electron microscopy study of grain boundary structure of deformed quartzite, Journal of Microscopy, 224, 306–321, http://doi:10.1111/j.1365-2818.2006.01697.x, 2006.

20   Skemer, P., Katayama, I., Jiang, Z., and Karato, S. I.: The misorientation index: Development of a new method for calculating the strength of lattice-preferred orientation, Tectonophysics, 411, 157-167, https://doi.org/10.1016/j.tecto.2005.08.023, 2005.

Spiers, C. J.: Fabric development in calcite polycrystals deformed at 400° C, Bulletin de Minéralogie, 102, 282–289, https://doi.org/10.3406/bulmi.1979.7289, 1979.

25   Stern, L. A., Durham, W. B., and Kirby, S. H.: Grain-size-induced weakening of H2O ices I and II and associated anisotropic recrystallization, Journal of Geophysical Research: Solid Earth, 102, 5313-5325, https://doi.org/10.1029/96jb03894, 1997.

Stipp, M., StuÈnitz, H., Heilbronner, R., and Schmid, S. M.: The eastern Tonale fault zone: a 'natural laboratory'for crystal plastic deformation of quartz over a temperature range from 250 to 700 C, Journal of structural geology, 24, 1861-1884, https://doi.org/10.1016/s0191-8141(02)00035-4, 2002.

30   Storey, C. D. and Prior, D. J.: Plastic deformation and recrystallization of garnet: a mechanism to facilitate diffusion creep, Journal of Petrology, 46, 2593-2613, https://doi.org/10.1093/petrology/egi067, 2005.

Treverrow, A., Budd, W. F., Jacka, T. H., and Warner, R. C.: The tertiary creep of polycrystalline ice: experimental evidence for stress-dependent levels of strain-rate enhancement, Journal of Glaciology, 58, 301-314, https://doi.org/10.3189/2012jog11j149, 2012.

Trimby, P. W., Prior, D. J., and Wheeler, J.: Grain boundary hierarchy development in a quartz mylonite, Journal of Structural Geology, 20, 917-935, https://doi.org/10.1016/s0191-8141(98)00026-1, 1998.

Underwood, E. E., Quantitative Stereology for Microstructural Analysis, in McCall, J. L., and Mueller, W. M., eds., Microstructural Analysis: Tools and Techniques: Boston, MA, Springer US, p. 35-66, 1973.

5   Urai, J. L., Means, W. D., and Lister, G. S.: Dynamic recrystallization of minerals, in: Mineral and Rock Deformation, edited by: Hobbs, B. and Heard, H., Laboratory Studies, 36, 161–199, https://doi.org/10.1029/gm036p0161, 1986.

Vaughan, M. J., Prior, D. J., Jefferd, M., Brantut, N., Mitchell, T. M., and Seidemann, M.: Insights into anisotropy development and weakening of ice from in situ P wave velocity monitoring during laboratory creep, J. Geophys. Res.-Sol. Ea., 122, 7076–7089, https://doi.org/10.1002/2017JB013964, 2017.

10   Warren, J. M. and Hirth, G.: Grain size sensitive deformation mechanisms in naturally deformed peridotites, Earth and Planetary Science Letters, 248, 438-450, https://doi.org/10.1016/j.epsl.2006.06.006, 2006.

Weertman, J.: Creep deformation of ice, Annual Review of Earth and Planetary Sciences, 11, 215-240, https://doi.org/10.1146/annurev.ea.11.050183.001243, 1983.

Weikusat, I., Kuiper, E.-J. N., Pennock, G. M., Kipfstuhl, S. and Drury, M. R.: EBSD analysis of subgrain boundaries and
15   dislocation slip systems in Antarctic and Greenland ice, Solid Earth, 8, 883–898, https://doi.org/10.5194/se-8-883-2017, 2017.

Whalley, W. B. and Azizi, F.: Rock glaciers and protalus landforms: Analogous forms and ice sources on Earth and Mars, Journal of Geophysical Research: Planets, 108, https://doi.org/10.1029/2002je001864, 2003.

Wheeler, J., Prior, D., Jiang, Z., Spiess, R. and Trimby, P.: The petrological significance of misorientations between grains,
20   Contrib Mineral Petrol, 141(1), 109–124, https://doi.org/10.1007/s004100000225, 2001.

Wheeler, J., Jiang, Z., Prior, D. J., Tullis, J., Drury, M. R., and Trimby, P. W.: From geometry to dynamics of microstructure: using boundary lengths to quantify boundary misorientations and anisotropy, Tectonophysics, 376, 19-35, https://doi.org/10.1016/j.tecto.2003.08.007, 2003.

Wheeler, J., Mariani, E., Piazolo, S., Prior, D. J., Trimby, P., and Drury, M. R.: The weighted Burgers vector: a new quantity
25   for constraining dislocation densities and types using electron backscatter diffraction on 2-D sections through crystalline materials, Journal of microscopy, 233, 482-494, https://doi.org/10.1111/j.1365-2818.2009.03136.x, 2009.

White, S.: The effects of strain on the microstructures, fabrics, and deformation mechanisms in quartzites, Philosophical Transactions of the Royal Society of London, ser. A, Mathematical and Physical Sciences, 283, 69-86, https://doi.org/10.1098/rsta.1977.0014, 1976.

30   Wilson, C. J. L. and Russell-Head, D. S.: Steady-state preferred orientation of ice deformed in plane strain at –1° C, Journal of Glaciology, 28, 145–160, https://doi.org/10.3189/s0022143000011850, 1982.

Wilson, C. J. L. and Peternell, M.: Ice deformed in compression and simple shear: control of temperature and initial fabric, Journal of Glaciology, 58, 11-22, https://doi.org/10.3189/2012jog11j065, 2012.

Wilson, C. J. L., Peternell, M., Piazolo, S. and Luzin, V.: Microstructure and fabric development in ice: Lessons learned from in situ experiments and implications for understanding rock evolution, Journal of Structural Geology, 61, 50–77, https://doi.org/10.1016/j.jsg.2013.05.006, 2014.

5 Wilson, C. J. L., Hunter, N. J., Luzin, V., Peternell, M., and Piazolo, S.: The influence of strain rate and presence of dispersed second phases on the deformation behaviour of polycrystalline D2O ice, Journal of Glaciology, 65, 101-122, https://doi.org/10.1017/jog.2018.100, 2019.

Wilson, C. J. L., Peternell, M., Hunter, N. J. R. and Luzin, V.: Deformation of polycrystalline D2O ice: Its sensitivity to temperature and strain-rate as an analogue for terrestrial ice, Earth and Planetary Science Letters, 532, 115999, https://doi:10.1016/j.epsl.2019.115999, 2020.

10 Xia, H., and Platt, J. P.: Quartz grainsize evolution during dynamic recrystallization across a natural shear zone boundary, Journal of Structural Geology, 109, 120-126, https://doi.org/10.1016/j.jsg.2018.01.007, 2018.

Table 1 Summary of experiments

Sample No.	Temperature	Initial length	True axial strain	Peak stress (corrected)	Strain rate at peak stress	True axial strain at peak stress	Final stress (corrected)	Final strain rate
	T (°C)	L_0 (mm)	(ε)	σ_p (MPa)	$\dot{\varepsilon}_p$ (s-1)	ε_p	σ_f (MPa)	$\dot{\varepsilon}_f$ (s-1)
PIL176	-10	30.480	0.03	1.78	1.03×10^{-5}	0.02	1.70	1.04×10^{-5}
PIL163	-10	48.768	0.05	2.92	1.03×10^{-5}	0.01	2.42	1.06×10^{-5}
PIL178	-10	39.624	0.08	2.54	1.11×10^{-5}	0.02	1.97	1.19×10^{-5}
PIL177	-10	40.640	0.12	2.85	1.11×10^{-5}	0.03	1.90	1.21×10^{-5}
[1]PIL007	-10	63.754	0.19	2.13	1.03×10^{-5}	0.02	1.33	1.22×10^{-5}
PIL254	-20	39.624	0.03	4.33	1.05×10^{-5}	0.02	4.25	1.06×10^{-5}
PIL182	-20	46.990	0.04	4.88	8.09×10^{-6}	0.02	4.44	8.94×10^{-6}
PIL184	-20	31.242	0.08	3.64	1.13×10^{-5}	0.04	3.24	1.17×10^{-5}
PIL185	-20	41.656	0.12	4.69	1.09×10^{-5}	0.03	3.68	1.19×10^{-5}
PIL255	-20	49.530	0.20	4.66	1.10×10^{-5}	0.03	2.93	1.28×10^{-5}
PIL165	-30	37.846	0.03	8.24	1.08×10^{-5}	0.03	8.15	1.09×10^{-5}
PIL162	-30	50.546	0.05	8.71	1.07×10^{-5}	0.03	7.87	1.10×10^{-5}
PIL164	-30	45.974	0.07	8.93	1.03×10^{-5}	0.03	7.31	1.07×10^{-5}
PIL166	-30	45.466	0.12	7.60	1.11×10^{-5}	0.03	6.45	1.20×10^{-5}
PIL268	-30	47.240	0.21	7.82	1.10×10^{-5}	0.02	5.00	1.31×10^{-5}

[1] Experiment from study by Qi and others (2017).

Table 2 Summary of EBSD analyses

Sample No.	T (°C)	Data with 30 µm step size				Data with 5 µm step size			
		Map area (Width × Length (mm))	No. indexed	No. grains	M-index for all indexed pixels	Map area (Width × Length (mm))	No. indexed	No. grains	M-index for all indexed pixels
undeformed	-	33.18 × 20.55	545323	11318	0.00370	24.47 × 7.86	4444599	1242	0.004500
PIL176	-10	25.00 × 25.00	353781	4728	0.00119	5.41 × 4.00	785025	694	0.010244
PIL163	-10	24.53 × 10.28	201134	4851	0.00858	6.80 × 4.16	992513	1494	0.008886
PIL178	-10	16.20 × 20.30	235789	6270	0.05765	5.50 × 4.11	690117	1028	0.046907
PIL177	-10	16.67 × 15.38	163507	5018	0.04068	5.49 × 4.14	645076	1507	0.040403
[1]PIL007	-10	13.10 × 5.87	91830	1655	0.12457	1.88 × 12.43	1010898	1789	0.118133
PIL254	-20	34.26 × 9.33	166929	2735	0.00227	5.41 × 4.24	641292	903	0.006909
PIL182	-20	36.58 × 6.04	213919	4053	0.00540	5.48 × 4.28	691817	907	0.004948
PIL184	-20	21.09 × 7.14	120209	2440	0.01296	5.50 × 4.13	665454	1157	0.010872
PIL185	-20	26.36 × 7.92	121589	3127	0.01541	5.56 × 4.23	625128	3023	0.019941
PIL255	-20	12.42 × 7.95	25644	1213	0.101764	3.41 × 4.20	472774	3057	0.106619
PIL165	-30	19.57 × 14.78	258779	4728	0.00077	5.45 × 3.07	594671	589	0.006147
PIL162	-30	25.96 × 10.00	191672	4833	0.00442	8.11 × 3.97	937793	2399	0.004555
PIL164	-30	18.22 × 22.56	229261	6087	0.02164	4.04 × 5.55	598744	1515	0.017329
PIL166	-30	31.26 × 18.29	415185	8878	0.02334	8.08 × 3.98	1043672	6036	0.020205
PIL268	-30	5.76 × 20.76	93394	1039	0.101730	5.69 × 10.18	1664877	8215	0.063540

[1] Experiment from study by Qi and others (2017).

Table 3 Summary of subgrain and grain sizes

Sample No.	T (°C)	$_2\varepsilon$	$_3$Percentage of repeat counted grains in 2-D (%)	$_4$Number density of "distinct" grains(μm^{-2})	Number density of "distinct" grains as ratio to starting material	$_5\bar{D}$ (μm)	$_6D_{median}$ (μm)	$_7D_{q,25\%}$ (μm)	$_8D_{q,75\%}$ (μm)	$_9D_{SMR}$ (μm)	$_{10}\overline{D_{big}}$ (μm)	$_{11}\overline{D_{small}}$ (μm)	$_{12}D_{peak}$ (μm)	$_{13}\bar{d}/_{14}d_{median}$ (μm)	$_{15}d_{q,25\%}/_{16}d_{q,75\%}$ (μm)	$_{17}d_{peak}$ (μm)
															$_{18}\varphi \geq 2°$	
undeformed	-	-	1.90	9.97E-06	1.00	297	291	165	413	274	-	-	300	291/280	161/392	-
PIL176	-10	0.03	9.45	3.24E-05	3.25	156	117	48	250	132	250	51	30	134/79	39/219	20
PIL163	-10	0.05	11.71	4.75E-05	4.76	125	98	54	171	110	197	58	35	104/77	51/162	25
PIL178	-10	0.08	13.47	3.82E-05	3.83	140	119	72	188	127	194	63	55	127/108	62/170	50
PIL177	-10	0.12	14.19	5.14E-05	5.15	114	90	54	155	101	184	59	40	96/77	45/129	30
$_1$PIL007	-10	0.19	13.07	6.25E-05	6.27	106	88	51	143	96	174	58	50	96/78	46/129	45
PIL254	-20	0.03	7.40	5.75E-05	5.77	114	62	36	174	93	197	38	25	91/46	29/106	20
PIL182	-20	0.04	5.30	3.97E-05	3.98	148	122	62	220	131	188	42	30	103/67	33/146	25
PIL184	-20	0.08	10.61	4.73E-05	4.74	122	89	48	164	105	169	42	45	88/58	36/109	20
PIL185	-20	0.12	7.76	1.05E-04	10.49	75	53	36	85	66	132	41	30	55/40	28/63	20
PIL255	-20	0.20	12.29	1.28E-04	12.85	64	53	36	81	59	106	41	30	55/46	32/68	25
PIL165	-30	0.03	2.07	3.15E-05	3.16	149	108	48	241	126	203	38	40	108/60	32/152	20
PIL162	-30	0.05	4.87	7.27E-05	7.29	103	76	45	135	91	144	40	35	70/49	31/86	20
PIL164	-30	0.07	5.58	6.67E-05	6.69	98	61	39	113	82	158	39	30	59/38	27/65	20
PIL166	-30	0.12	6.01	1.34E-04	13.45	67	54	37	79	61	104	70	35	57/47	32/69	25
PIL268	-30	0.21	5.66	1.18E-04	11.88	60	37	29	53	50	158	35	30	42/30	24/41	20

[1]Experiment from study by Qi and others (2017). [2]True axial strain. [3]See section S4 of supplementary material for method. 2-D grains attributed to the same 3-D grain are selected by a critical misorientation angle threshold of 10°. [4]Number density of "distinct" grains, which is calculated from number of "distinct" grains divided by total grain area. "Distinct" grains are calculated by counting 2-D grains attributed to the same 3-D grain as one. 2-D grains attributed to the same 3-D grain are selected by a critical misorientation angle threshold of 10° (section 3.3.2 and section S4 in supplementary material). [5]Mean grain size. [6]Median grain size. [7]Lower quartiles, which split off the lowest 25% of the grain sizes from the highest 75%. [8]Higher quartiles, which split off the highest 25% of the grain sizes from the lowest 75%. [9]Square mean root grain size. [10]Mean grain size of "big grains". [11]Mean grain size of "small grains". [12]Peak grain size in grain size distribution. [13]Mean subgrain size (with $\varphi \geq 2°$). [14]Median subgrain size (with $\varphi \geq 2°$). [15]Lower quartiles (with $\varphi \geq 2°$), which split off the lowest 25% of the subgrain sizes from the highest 75%. [16]Higher quartiles (with $\varphi \geq 2°$), which split off the highest 25% of the subgrain sizes from the lowest 75%. [17]Peak subgrain size in subgrain size (with $\varphi \geq 2°$) distribution. [18]Boundary misorientation angle.

Table 4 Summary of the open half-angle of the c-axis cone (θ) from this study and the literature

| Reference	Name	Material	T (°C)	No. of c-axes	θ (°)	Conditions*		True axial strain rate converted (s-1)	True axial strain converted (%)
This study	PIL163	H_2O	-10	353781	40		$\varepsilon = 5\%$	1.06×10^{-5}	5.0
	PIL178	H_2O	-10	201134	36		$\varepsilon = 8\%$	1.19×10^{-5}	8.0
	PIL177	H_2O	-10	235789	36		$\varepsilon = 12\%$	1.21×10^{-5}	12.0
	PIL007	H_2O	-10	163507	34		$\varepsilon = 19\%$	1.22×10^{-5}	19.0
	PIL182	H_2O	-20	213919	30	Constant displacement rate $\dot{\varepsilon} = {\sim}1 \times 10^{-5} s^{-1}$	$\varepsilon = 4\%$	8.94×10^{-6}	4.0
	PIL184	H_2O	-20	120209	26		$\varepsilon = 8\%$	1.17×10^{-5}	8.0
	PIL185	H_2O	-20	121589	28		$\varepsilon = 12\%$	1.19×10^{-5}	12.0
	PIL255	H_2O	-20	25644	32		$\varepsilon = 20\%$	1.28×10^{-5}	20.0
	PIL164	H_2O	-30	229261	14		$\varepsilon = 7\%$	1.07×10^{-5}	7.0
	PIL166	H_2O	-30	415185	16		$\varepsilon = 12\%$	1.20×10^{-5}	12.0
	PIL268	H_2O	-30	93394	8		$\varepsilon = 21\%$	1.31×10^{-5}	21.0
Jacka and Maccagnan (1984)	A2	H_2O	-3	132	42		$\dot{\gamma} = 3.6 \times 10^{-8} s^{-1}, \gamma = 2.4\%$	5.17×10^{-8}	3.4
	A3	H_2O	-3	98	36		$\dot{\gamma} = 4.0 \times 10^{-8} s^{-1}, \gamma = 2.9\%$	5.77×10^{-8}	4.1
	A4	H_2O	-3	111	28	Constant load $\sigma = {\sim}0.2$ MPa	$\dot{\gamma} = 6.1 \times 10^{-8} s^{-1}, \gamma = 6.8\%$	9.04×10^{-8}	9.8
	A5	H_2O	-3	95	36		$\dot{\gamma} = 6.3 \times 10^{-8} s^{-1}, \gamma = 7.3\%$	9.37×10^{-8}	10.6
	A6	H_2O	-3	108	26		$\dot{\gamma} = 6.1 \times 10^{-8} s^{-1}, \gamma = 15.0\%$	9.53×10^{-8}	22.3
	A7	H_2O	-3	96	30		$\dot{\gamma} = 6.0 \times 10^{-8} s^{-1}, \gamma = 32.5\%$	1.02×10^{-7}	51.0
Jacka and Li (2000)	N/A	H_2O	-5	87	26	Constant load, $\sigma = 0.2$ MPa	$\dot{\gamma} = 3.4 \times 10^{-8} s^{-1}, \gamma = 11.0\%$	5.18×10^{-8}	16.2
	N/A	H_2O	-10	100	32	Constant load, $\sigma = 0.2$ MPa	$\dot{\gamma} = 6.6 \times 10^{-9} s^{-1}, \gamma = 10.0\%$	9.99×10^{-9}	14.6
	N/A	H_2O	-15	173	38	Constant load, $\sigma = 0.5$ MPa	$\dot{\gamma} = 7.5 \times 10^{-8} s^{-1}, \gamma = 11.0\%$	1.14×10^{-7}	16.2
	N/A	H_2O	-15	199	32	Constant load, $\sigma = 0.4$ MPa	$\dot{\gamma} = 3.6 \times 10^{-8} s^{-1}, \gamma = 11.0\%$	5.49×10^{-8}	16.2
Piazolo et al (2013)	MD6	D_2O	-7	N/A	35		$\dot{e} = 6 \times 10^{-7} s^{-1}, e = 10\%$	6.67×10^{-7}	11.0
	MD10	D_2O	-7	N/A	35		$\dot{e} = 2.5 \times 10^{-6} s^{-1}, e = 10\%$	2.78×10^{-6}	11.0
	MD3	D_2O	-7	N/A	35	Constant displacement rate	$\dot{e} = 2.5 \times 10^{-6} s^{-1}, e = 20\%$	3.13×10^{-6}	22.0
	MD12	D_2O	-7	N/A	35		$\dot{e} = 1.0 \times 10^{-5} s^{-1}, e = 10\%$	1.11×10^{-5}	11.0
	MD4	D_2O	-7	N/A	35		$\dot{e} = 1.0 \times 10^{-5} s^{-1}, e = 20\%$	1.25×10^{-5}	22.0
	MD22	D_2O	-7	N/A	30		$\dot{e} = 1.0 \times 10^{-5} s^{-1}, e = 40\%$	1.67×10^{-5}	51.0
Montagnat et al (2015)	N/A	H_2O	-5	2838	40	Constant load, $\sigma = 0.8$ MPa	$\dot{e} = 1.2 \times 10^{-7} s^{-1}, e = 7\%$	1.30×10^{-7}	7.0
	N/A	H_2O	-5	N/A	35	Constant load, $\sigma = 0.75$	$\dot{e} = 3.9 \times 10^{-7} s^{-1}, e = 12\%$	4.43×10^{-7}	12.8
	N/A	H_2O	-5	1862	35	Constant load, $\sigma = 0.7$ MPa	$\dot{e} = 3.8 \times 10^{-7} s^{-1}, e = 13\%$	4.37×10^{-7}	13.9
	N/A	H_2O	-5	830	33	Constant load, $\sigma = 0.8$ MPa	$\dot{e} = 3.8 \times 10^{-7} s^{-1}, e = 18\%$	4.63×10^{-7}	19.9

| Reference	Sample	Medium	Temp			Test type	Condition	Value	
Qi et al (2017)	PIL7	H₂O	-10	N/A	37	Constant displacement rate	$\dot{\varepsilon} = \sim 1 \times 10^{-5} s^{-1}, \varepsilon = 18\%$	1.10×10^{-5}	18.0
	PIL32	H₂O	-10	N/A	34		$\dot{\varepsilon} = \sim 2 \times 10^{-6} s^{-1}, \varepsilon = 21\%$	2.31×10^{-6}	21.0
	PIL33	H₂O	-10	N/A	26		$\dot{\varepsilon} = \sim 2 \times 10^{-4} s^{-1}, \varepsilon = 22\%$	2.42×10^{-4}	22.0
	PIL35	H₂O	-10	N/A	35		$\dot{\varepsilon} = \sim 1 \times 10^{-5} s^{-1}, \varepsilon = 13\%$	1.35×10^{-5}	13.0
	PIL36	H₂O	-10	N/A	34		$\dot{\varepsilon} = \sim 5 \times 10^{-5} s^{-1}, \varepsilon = 19\%$	5.02×10^{-5}	19.0
Vaughan et al (2017)	def013	H₂O	-5	206641	42	Constant displacement rate $\dot{e} = \sim 1 \times 10^{-6} s^{-1}$	$e = 3\%$	1.03×10^{-6}	3.0
	def012	H₂O	-5	309428	36		$e = 5\%$	1.05×10^{-6}	5.1
	def011	H₂O	-5	218653	38		$e = 7.5\%$	1.08×10^{-6}	7.8
	def010	H₂O	-5	335722	34		$e = 10\%$	1.11×10^{-6}	10.5
Craw et al (2018)	PIL133	H₂O	-30	N/A	0	Constant displacement rate	$\dot{\varepsilon} = \sim 2 \times 10^{-6} s^{-1}, \varepsilon = 20\%$	2.60×10^{-6}	20
	PIL141	H₂O	-30	N/A	0		$\dot{\varepsilon} = \sim 5 \times 10^{-6} s^{-1}, \varepsilon = 23\%$	7.20×10^{-6}	23
	PIL132	H₂O	-30	N/A	0		$\dot{\varepsilon} = \sim 2 \times 10^{-5} s^{-1}, \varepsilon = 20\%$	2.80×10^{-5}	20
Wilson et al (2020)	MD7	D₂O	-3	N/A	34	Constant displacement rate	$\dot{e} = 1.0 \times 10^{-5} s^{-1}, e = 20\%$	1.25×10^{-5}	22
	MD9	D₂O	-10	N/A	33		$\dot{e} = 2.5 \times 10^{-6} s^{-1}, e = 20\%$	3.13×10^{-6}	22
	DH24	D₂O	-20	N/A	30		$\dot{e} = 2.5 \times 10^{-6} s^{-1}, e = 20\%$	3.13×10^{-6}	22
	D1_5	D₂O	-3	N/A	34		$\dot{e} = 2.5 \times 10^{-6} s^{-1}, e = 20\%$	3.13×10^{-6}	22
	D1_1	D₂O	-1	N/A	36		$\dot{e} = 2.5 \times 10^{-6} s^{-1}, e = 20\%$	3.13×10^{-6}	22
Hooke and Hudleston (1981)	Coarse -100m	Natural ice	-4 ~ -6	65	22-32	Constant uniaxial strain rate $\dot{e} = 5.7 \times 10^{-11} s^{-1}$	$\bar{\gamma}_{oc} = 40\%$	7.71×10^{-11}	30
	Coarse -125m			53	28-38		$\bar{\gamma}_{oc} = 50\%$	8.37×10^{-11}	38
	Coarse -154m			82	22-32		$\bar{\gamma}_{oc} = 60\%$	9.09×10^{-11}	47
	Coarse -175m			56	20-30		$\bar{\gamma}_{oc} = 70\%$	9.90×10^{-11}	55
	Coarse -191m			93	19-29		$\bar{\gamma}_{oc} = 80\%$	1.08×10^{-10}	64
	Coarse -215m			155	18-28		$\bar{\gamma}_{oc} = 90\%$	1.18×10^{-10}	73
	Coarse -238m			61	15-25		$\bar{\gamma}_{oc} = 110\%$	1.41×10^{-10}	90
	Coarse -291m			119	14-24		$\bar{\gamma}_{oc} = 150\%$	2.00×10^{-10}	126
	Coarse -315m			102	13-23		$\bar{\gamma}_{oc} = 170\%$	2.38×10^{-10}	143
	Fine -125m			52	26		$\bar{\gamma}_{oc} = 40\%$	7.71×10^{-11}	30
	Fine -150m			89	21		$\bar{\gamma}_{oc} = 50\%$	8.37×10^{-11}	38
	Fine -175m			65	28		$\bar{\gamma}_{oc} = 60\%$	9.09×10^{-11}	47

|						
Fine -238m	79	17		$\bar{\gamma}_{oc} = 110\%$	1.41×10^{-10}	90

* $\dot{\varepsilon}$ is the true axial strain rate, ε is the true axial strain, $\dot{\gamma}$ is the octahedral shear strain rate, γ is the octahedral shear strain, $\dot{e}$ is the engineering axial strain rate, e is the engineering axial strain, σ is the initial stress, $\bar{\gamma}_{oc}$ is the natural octahedral unit shear.
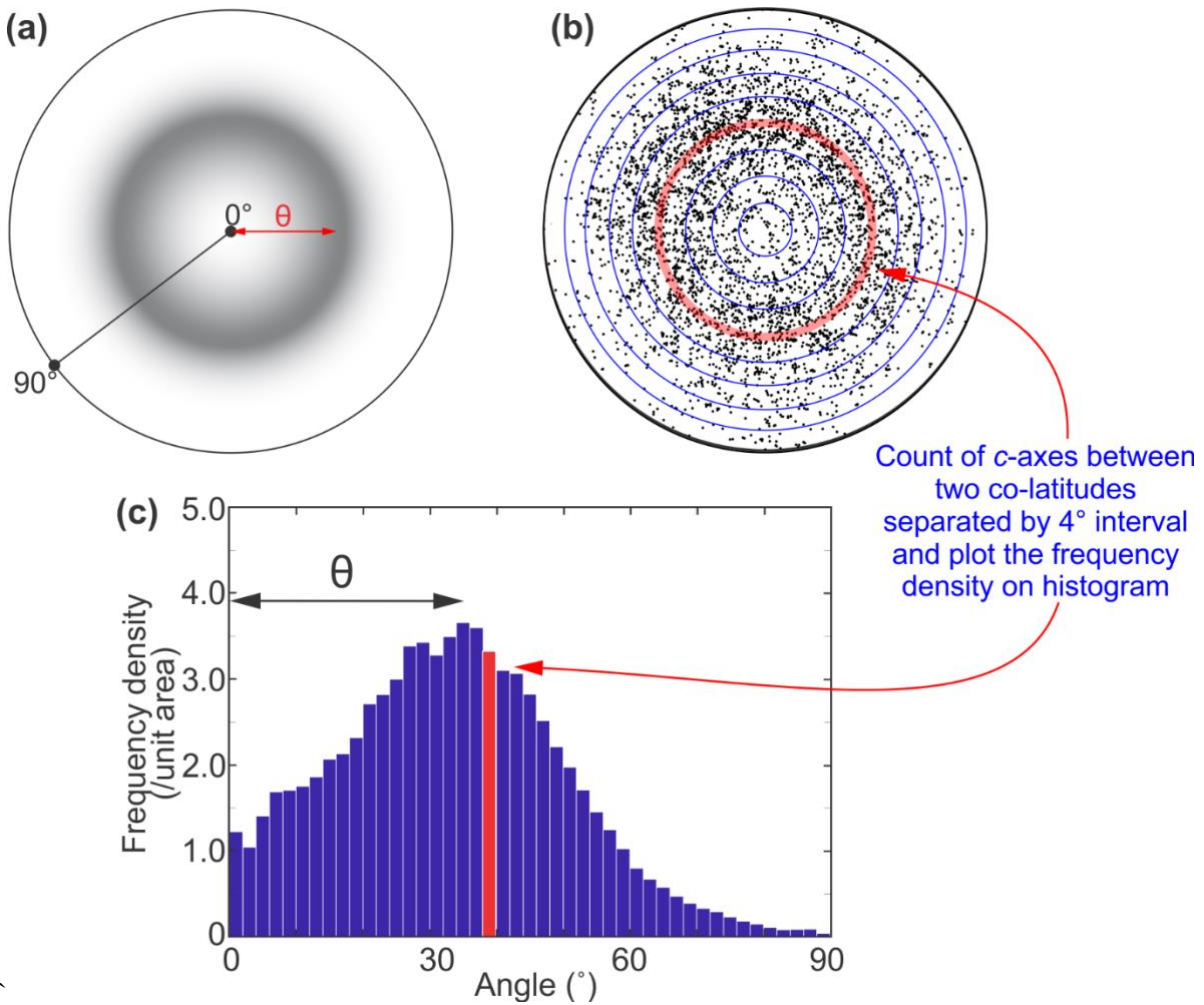
Figure 1. (a) Typical *c*-axes distribution at high temperatures with compression axis perpendicular to the page. **(b)** A schematic drawing explaining the method used to quantify the distribution of *c*-axes. The *c*-axes point pole figure taken from PIL178 is used as an example. The pole figure is plotted with lower hemisphere equal-area projection, and compression axis perpendicular to the page. Only 3000 points are plotted for demonstration purpose. At a given angle, red transparent circle covering co-latitudes separated by 4 degrees' interval is drawn. The points lying between the given co-latitudes (covered by the red transparent circle) are counted. The frequency density of the points is calculated from the normalised counts divided by the normalised area between the given co-latitudes. **(c)** The distribution of *c*-axes frequency density as a function of angle to the compression axis. The angle corresponds to the peak in the distribution is taken as the opening half-angle θ for the cone (small circle) shaped *c*-axes distribution. Throughout the text this is referred to as the opening-angle.
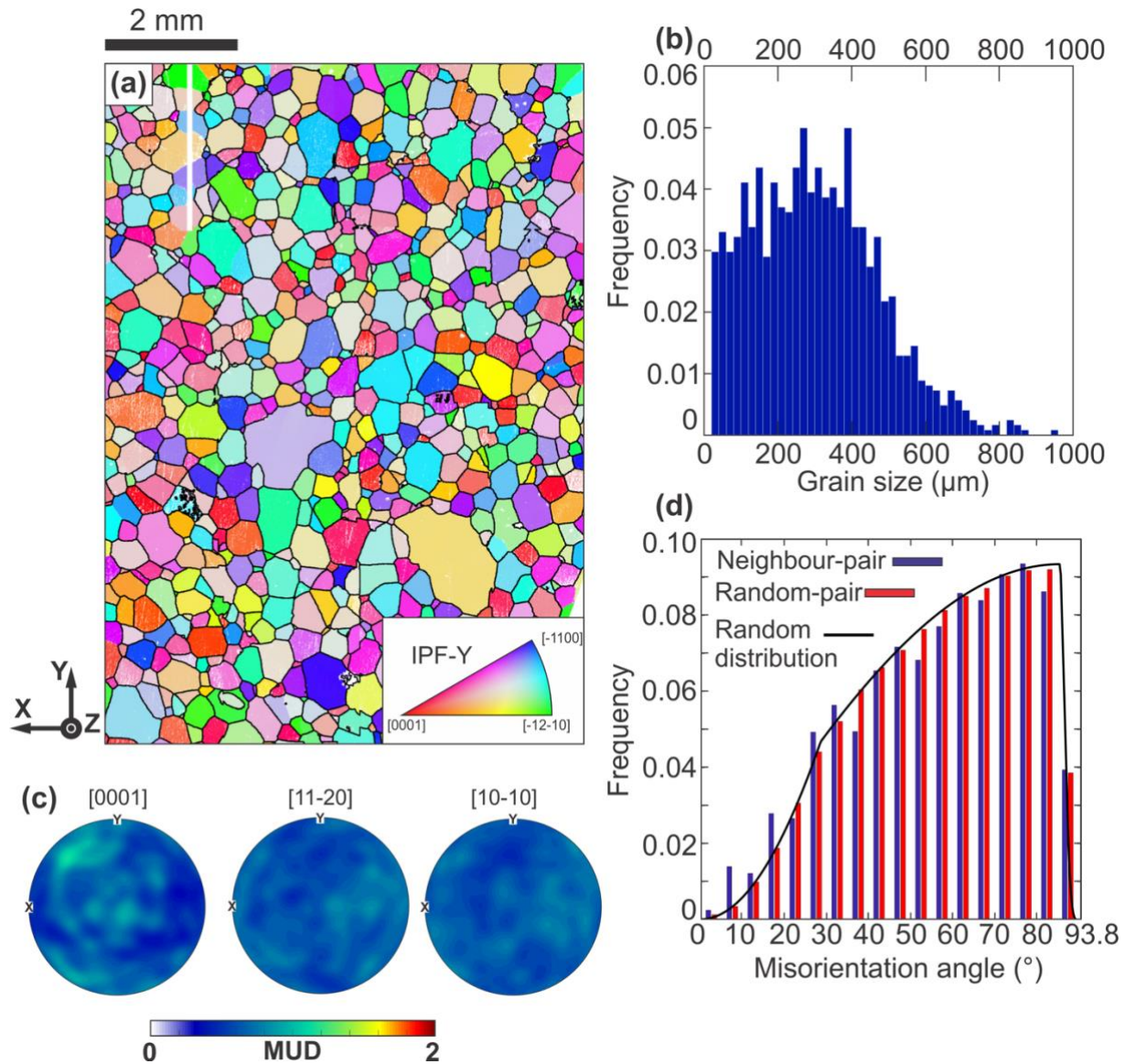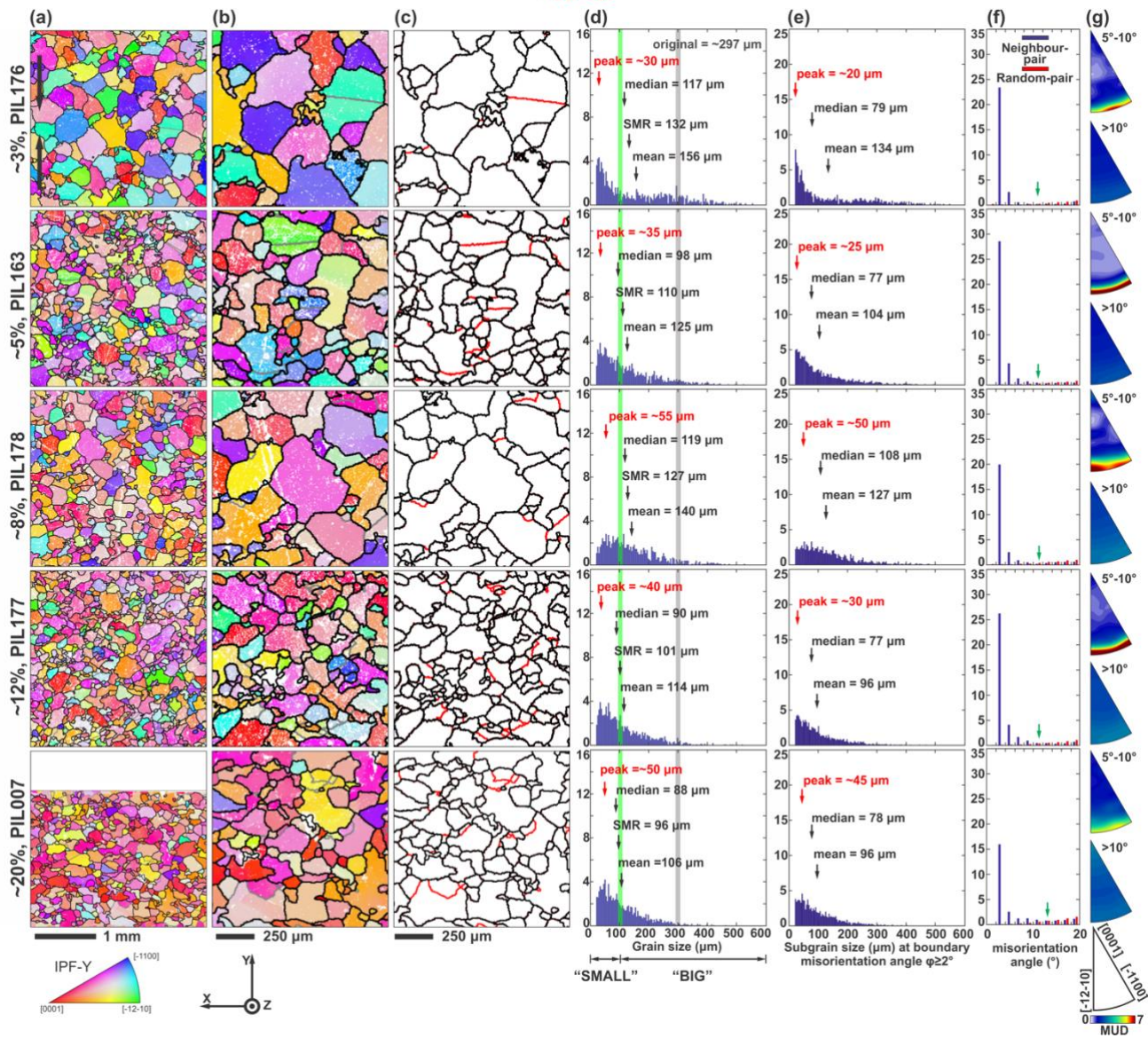
Figure 2. Microstructural details of undeformed standard ice. The EBSD data collected with 5 µm step size are presented as (**a**) Orientation maps coloured by IPF-Y, which uses the colour map to indicate the crystallographic axes that are parallel to the y-axis as shown by the black arrows. (**b**) Grain size distribution. (**c**) The distributions of orientations for [0001] (*c*-axes), [11-20] (*a*-axes) and [10-10] (poles to *m*-planes). (**d**) Misorientation angle distribution for (**a**). Neighbour-pair misorientation angle distribution is shown with blue bars. Random-pair misorientation angle distribution is shown with red bars. Misorientation angle distribution calculated for randomly distributed ice 1h crystals are shown with black line.
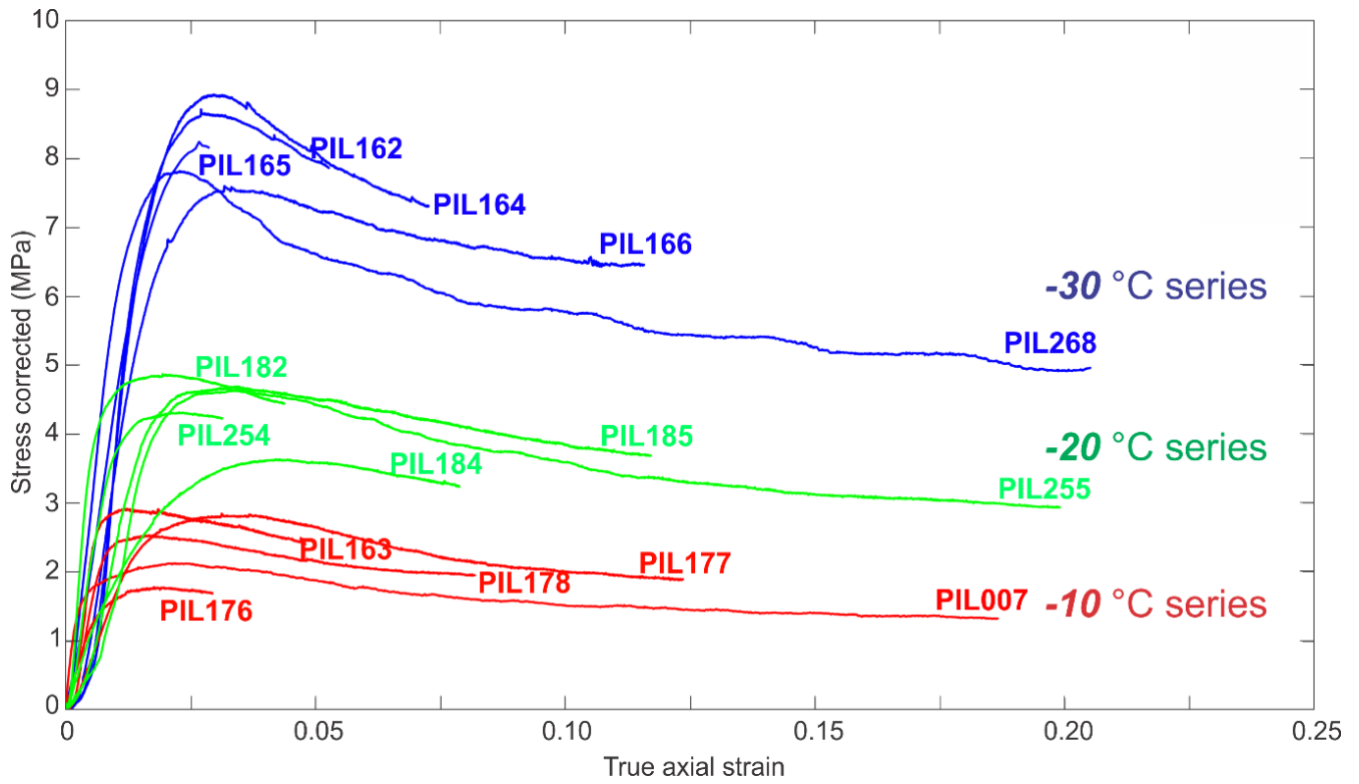
Figure 3. The stress-strain curves for all the deformed ice samples. The *x*-axis is the true axial strain (Eq. (2)). The *y*-axis is the uniaxial stress. The stress has been corrected for the change of sample cross-sectional area, assuming constant sample volume during the deformation.

-10 °C

(a) IPF-Y · (b) · (c) · (d) Grain size (μm) · (e) Subgrain size (μm) at boundary misorientation angle φ≥2° · (f) misorientation angle (°) · (g)

~3%, PIL176

- (d) original = ~297 μm; peak = ~30 μm; median = 117 μm; SMR = 132 μm; mean = 156 μm
- (e) peak = ~20 μm; median = 79 μm; mean = 134 μm
- (f) Neighbour-pair; Random-pair
- (g) 5°-10°; >10°

~5%, PIL163

- (d) peak = ~35 μm; median = 98 μm; SMR = 110 μm; mean = 125 μm
- (e) peak = ~25 μm; median = 77 μm; mean = 104 μm
- (g) 5°-10°; >10°

~8%, PIL178

- (d) peak = ~55 μm; median = 119 μm; SMR = 127 μm; mean = 140 μm
- (e) peak = ~50 μm; median = 108 μm; mean = 127 μm
- (g) 5°-10°; >10°

~12%, PIL177

- (d) peak = ~40 μm; median = 90 μm; SMR = 101 μm; mean = 114 μm
- (e) peak = ~30 μm; median = 77 μm; mean = 96 μm
- (g) 5°-10°; >10°

~20%, PIL007

- (d) peak = ~50 μm; median = 88 μm; SMR = 96 μm; mean = 106 μm
- (e) peak = ~45 μm; median = 78 μm; mean = 96 μm
- (g) 5°-10°; >10°

Scale bars: 1 mm; 250 μm; 250 μm

IPF-Y legend: [-1100], [0001], [-12-10]

"SMALL" ↔ "BIG"

MUD 0–7

45

Figure 4. Microstructural analyses of deformed ice samples at -10 °C. Axial true strain increases from ~3% on top to ~20% to bottom. The EBSD data collected with 5 µm step size are presented as **(a)** orientation maps at low magnification and **(b)** orientation maps of selected areas at high magnification. Orientation maps are coloured by IPF-Y, which uses the colour map to indicate the crystallographic axes that are parallel to the vertical shortening direction as shown by the black arrows. Ice grain boundaries with a misorientation larger than 10° are shown black. Non-indexed pixels are shown white. Subgrain boundaries, where misorientation angles between neighbouring pixels are between 2° and 10°, are shown grey. Maps show data without interpolation. **(c)** Distribution of subgrain boundaries. Subgrain boundaries are shown red. Grain boundaries are shown black. **(d)** Distribution of ice grain size presented in 4 µm bins. Mean, median and square mean root (SMR) diameters are indicated by black arrows. The main peak of the grain size distribution is indicated by a red arrow. Vertical grey line marks the mean grain size of the starting material. Vertical green line marks the threshold grain size between "big grains" and "small grains" (see text). **(e)** Distribution of subgrain size presented in 4 µm bins. The subgrain size is calculated by applying the boundary misorientation angle of $\varphi \geq 2°$. **(f)** Distribution of neighbour-pair and random-pair misorientation angles. The misorientation angle at which neighbour-pair frequency reduces to be equal to the random-pair frequency is marked with a green arrow. **(g)**. Misorientation axes distribution plotted in crystal reference frame as contoured inverse pole figure (IPF). The contoured IPFs are coloured by MUD. Neighbour-pair misorientation axes for neighbouring pixels with misorientation angles of 5°-10° are presented in the upper box. Grain boundary (>10°) misorientation axes using pixels along the grain boundaries of neighbouring grains are presented in the lower box.
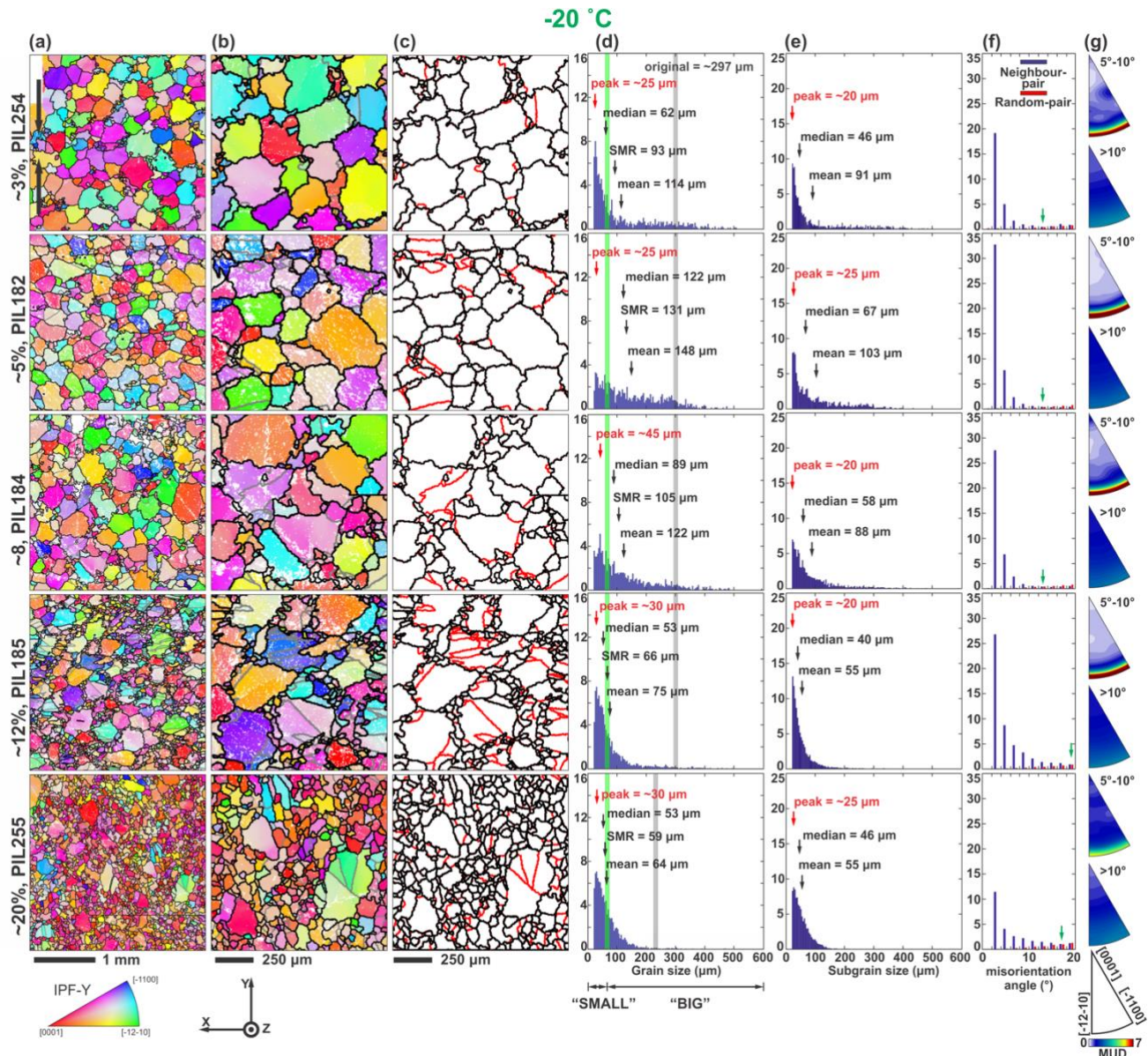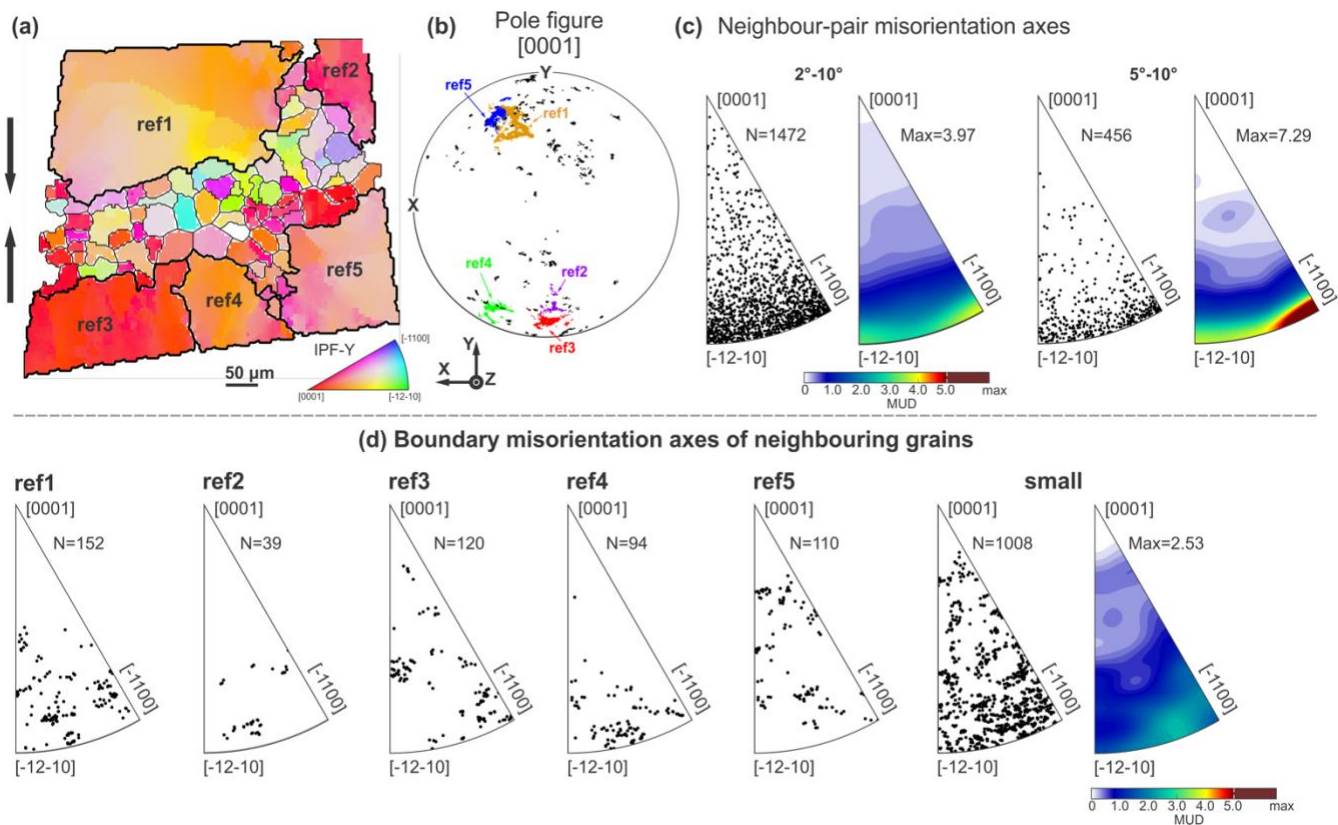
Figure 5. Microstructural analyses of deformed ice samples at -20 °C. Axial true strain increases from ~3% on top to ~20% to bottom. The descriptions of columns **(a)** to **(g)** are the same as in Fig. 4.
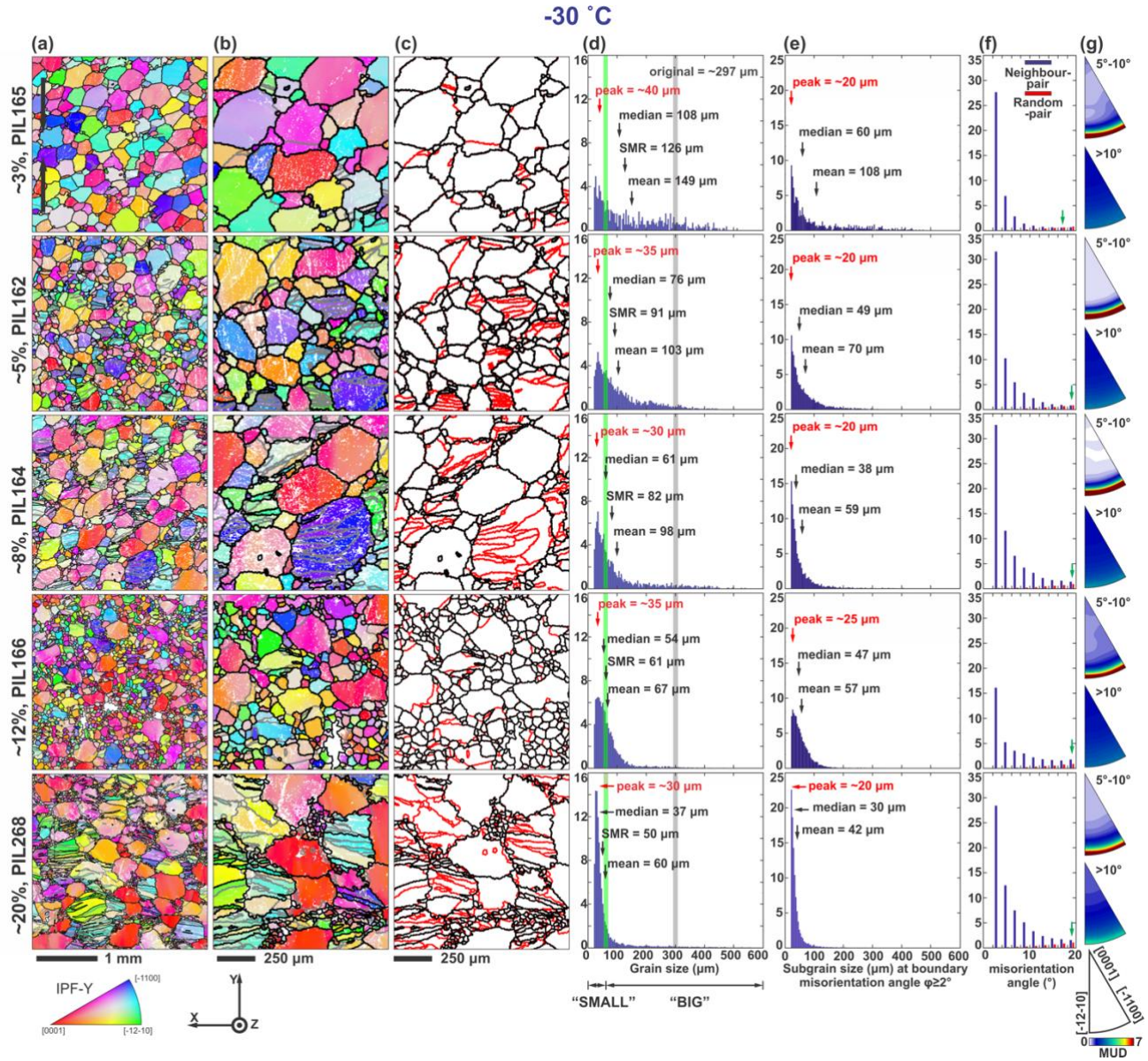
Figure 6. Microstructural analyses of deformed ice samples at -30 °C. Axial true strain increases from ~3% on top to ~20% to bottom. The descriptions of columns **(a)** to **(g)** are the same as in Fig. 4.

Figure 7. Misorientation axes analyses of a sub-area from the EBSD map of sample PIL268 (-30 °C, ~20% strain). **(a)** orientation map coloured by IPF-Y, which uses the colour map to indicate the crystallographic axes that are parallel to the vertical shortening direction as shown by the black arrows. Ice grain boundaries with a misorientation larger than 10° are shown black. "Big" reference grains are shown with thick black boundaries. "Small" grains are shown with thin black boundaries. **(b)** The pole figure of *c*-axes corresponding to orientations of all pixels of grains in **(a)**. *c*-axes of "small" grains are shown with black dots. *c*-axes of "big" reference grains are shown with dots coloured by non-black colours. **(c)** Neighbour-pair misorientation axes for neighbouring pixels with misorientation angles of 2°-10° and 5°-10° corresponding to **(a)**. The misorientation axes are plotted in crystal reference frame as inverse pole figure (IPF). The IPF either shows all points or coloured by MUD. The number of points or maximum value of MUD are given next to each IPF. **(d)** Boundary misorientation axes of "big" reference grains and corresponding neighbouring grains, and neighbouring grains among "small" grains. Grain boundary misorientation axes are calculated using pixels along the grain boundaries of neighbouring grains.
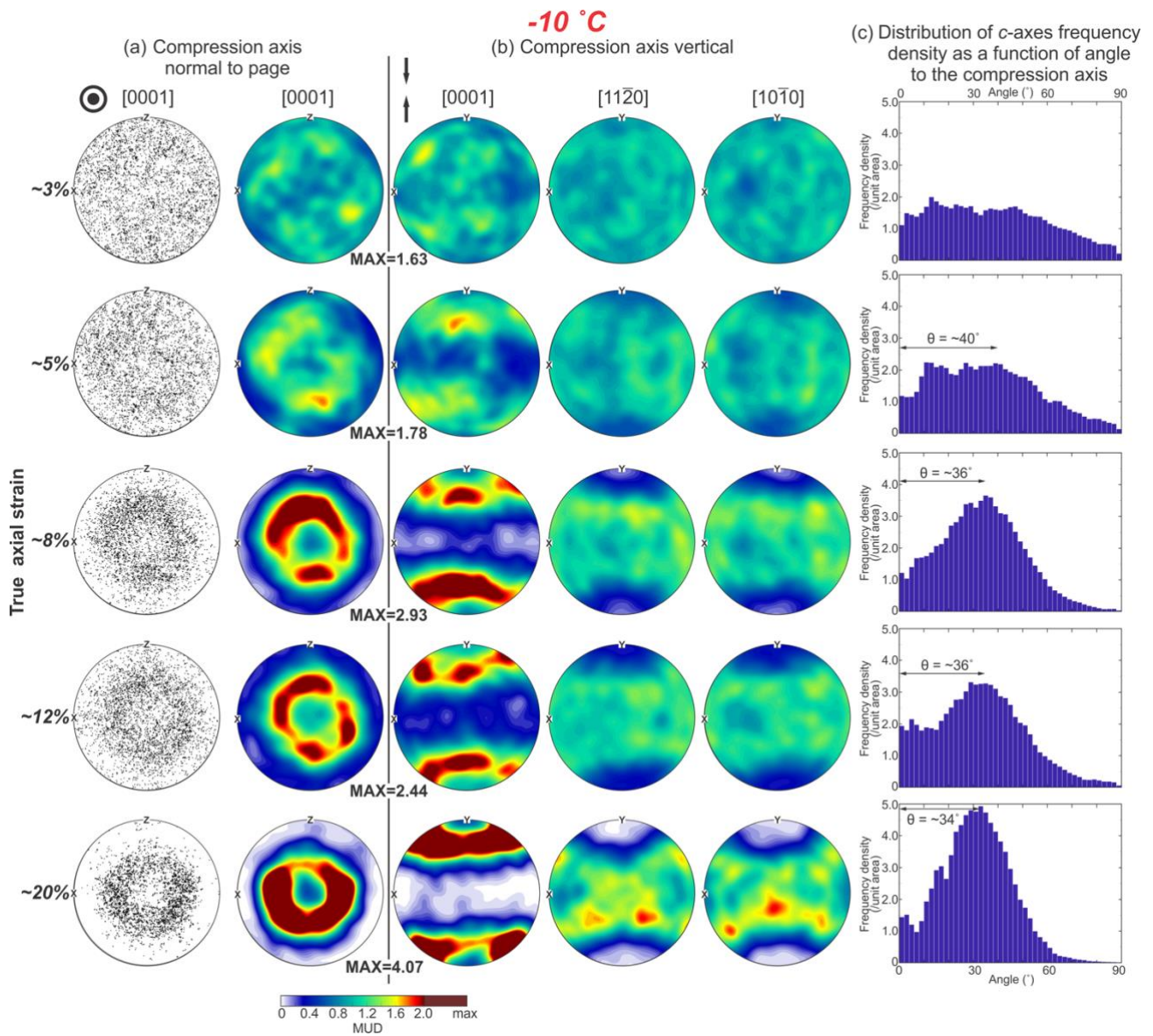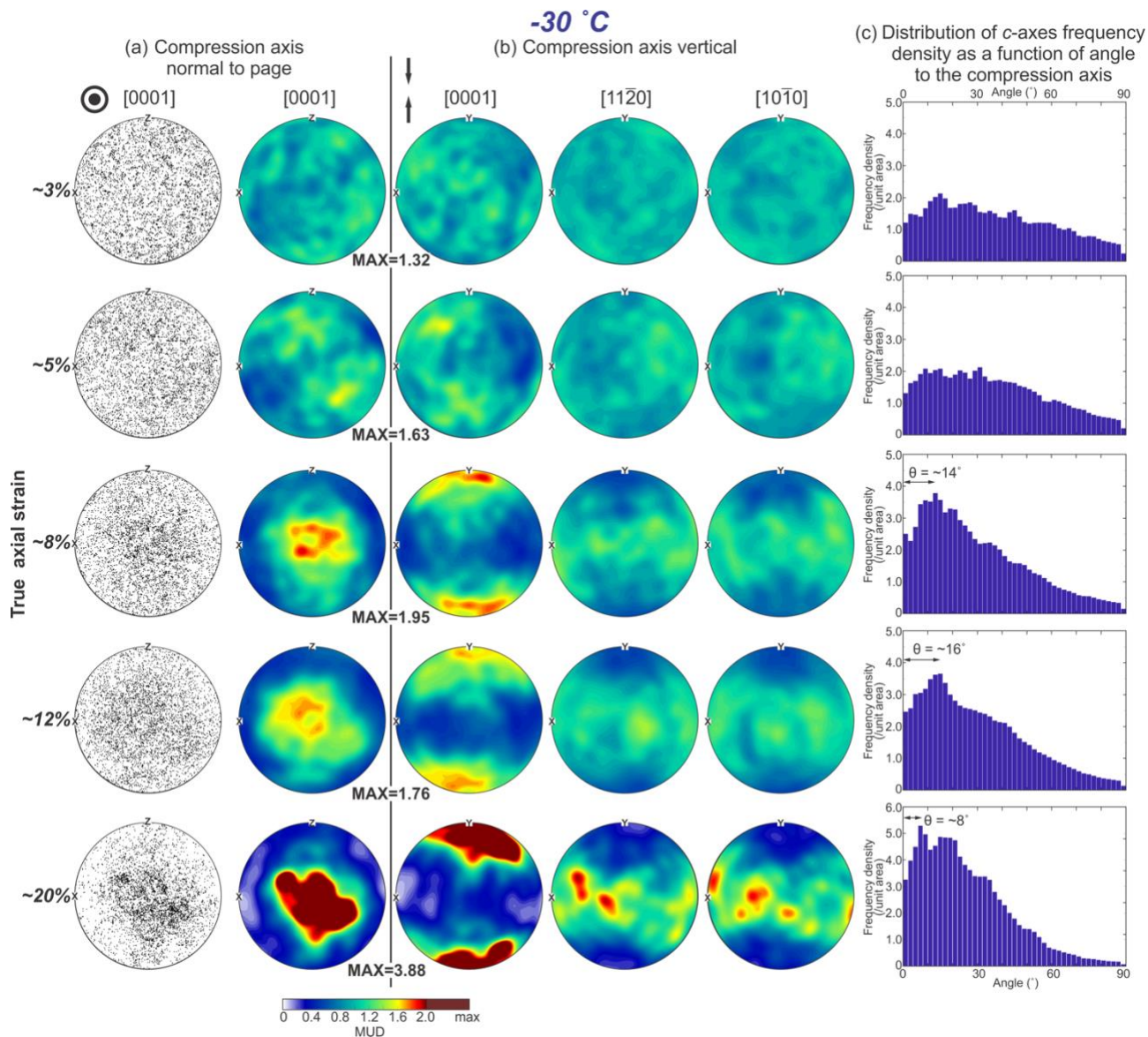
Figure 8. Crystallographic preferred orientations (CPOs) from EBSD data with 30 μm step size for ice samples deformed at -10 °C. Axial true strain increases from ~3% on top to ~20% to bottom. **(a)** The distributions of [0001] (*c*-axes) orientations plotted as point pole figures with 5000 randomly selected points and contoured pole figures. The compression axis is perpendicular to the page. **(b)** The distributions of orientations for [0001] (*c*-axes), [11-20] *a*-axes and [10-10] (poles to *m*-planes) plotted as contoured pole figures. The compression axis is vertical. Contoured pole figures are contoured based on MUD. The maximum value of MUD for the *c*-axis CPO of each sample is given between columns (a) and (b). **(c)** Distributions of the [0001] axes frequency density as a function of angle to the compression axis. Open half-angle θ of the cone (small circle) is presented on each histogram.

50
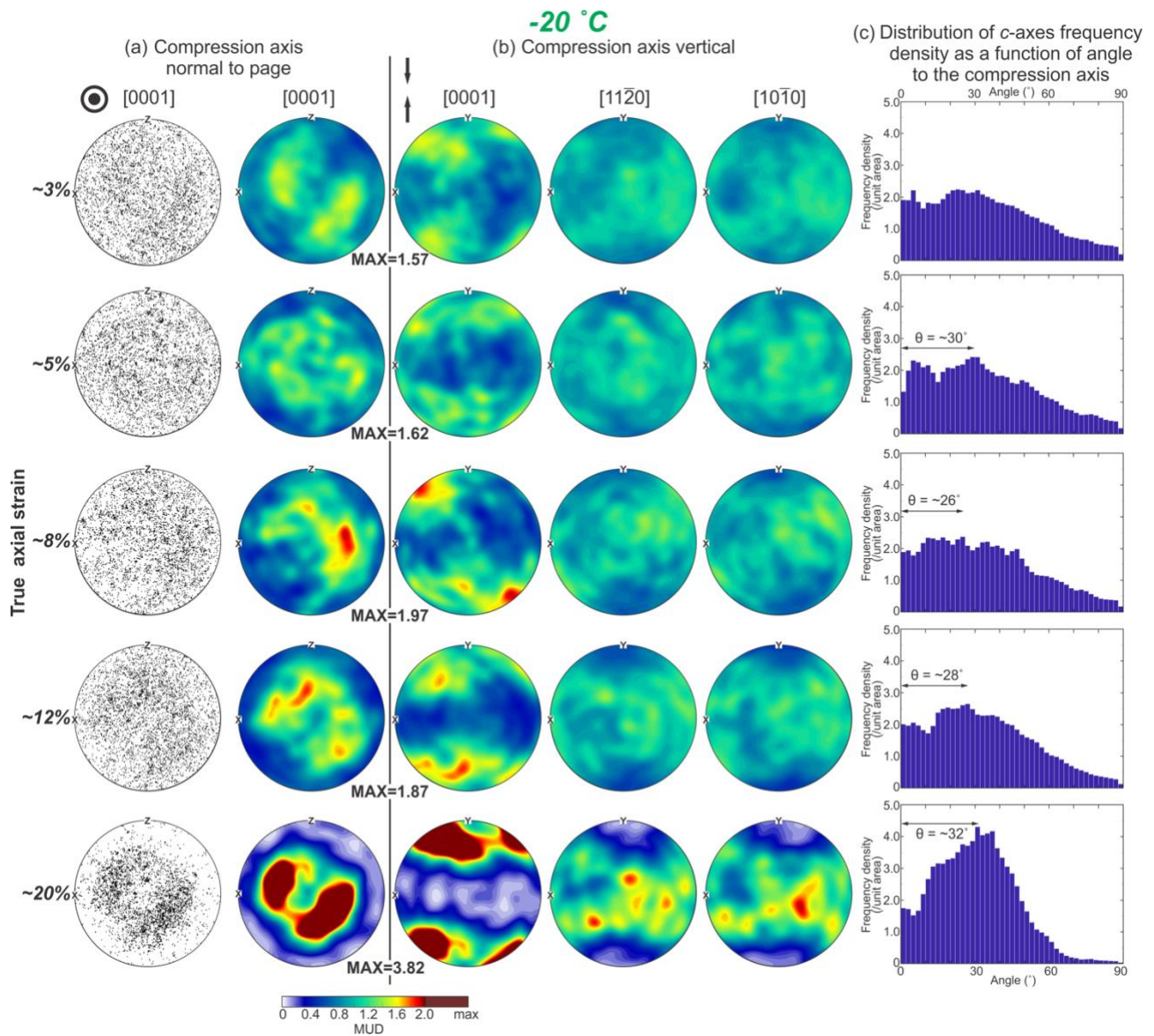
Figure 9. Crystallographic preferred orientations (CPOs) from EBSD data with 30 µm step size for ice samples deformed at -20 °C. Explanation of annotations and the descriptions of sections **(a)** to **(c)** are the same as in Fig. 8.

51

Figure 10. Crystallographic preferred orientations (CPOs) from EBSD data with 30 µm step size for ice samples deformed at -30 °C. Explanation of annotations and the descriptions of sections **(a)** to **(c)** are the same as in Fig. 8.

5
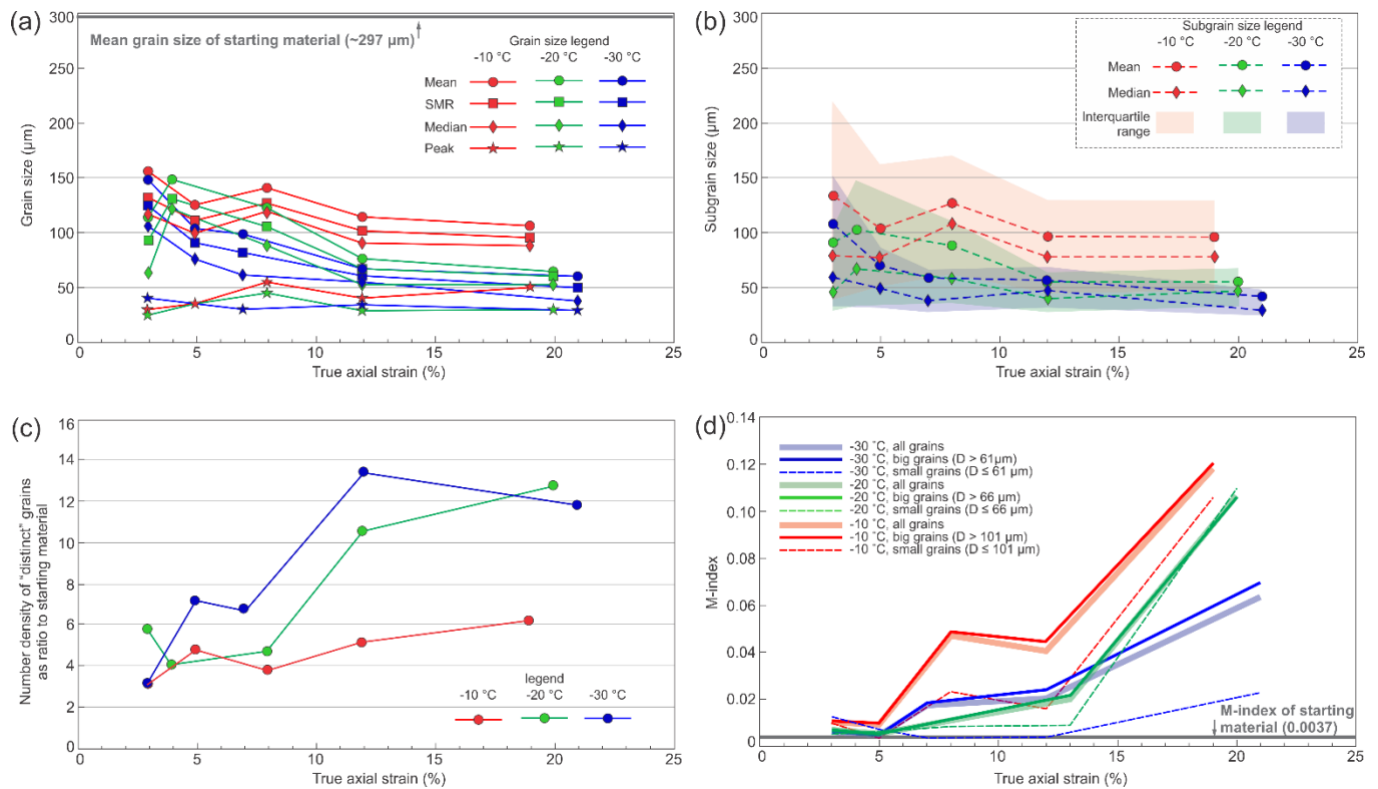
Figure 11. (a) Variation in the mean, SMR (square mean root), median and peak grain size as a function of true axial strain in each temperature series. **(b)** Variation in the mean, median subgrain grain size and interquartile range of subgrain size at boundary misorientation angle threshold of 2° as a function of true axial strain in each temperature series. The upper and lower bounds of interquartile range are constrained by lower quartile subgrain size and higher quartile subgrain size, respectively. **(c)** Variation in number density of "distinct" grains as ratio to starting material relative to true axial strain in each temperature series. **(d)** Variation in CPO strength (M-index) as a function of true axial strain for different grain size categories in each temperature series. M-indices are calculated from 5 µm EBSD data.
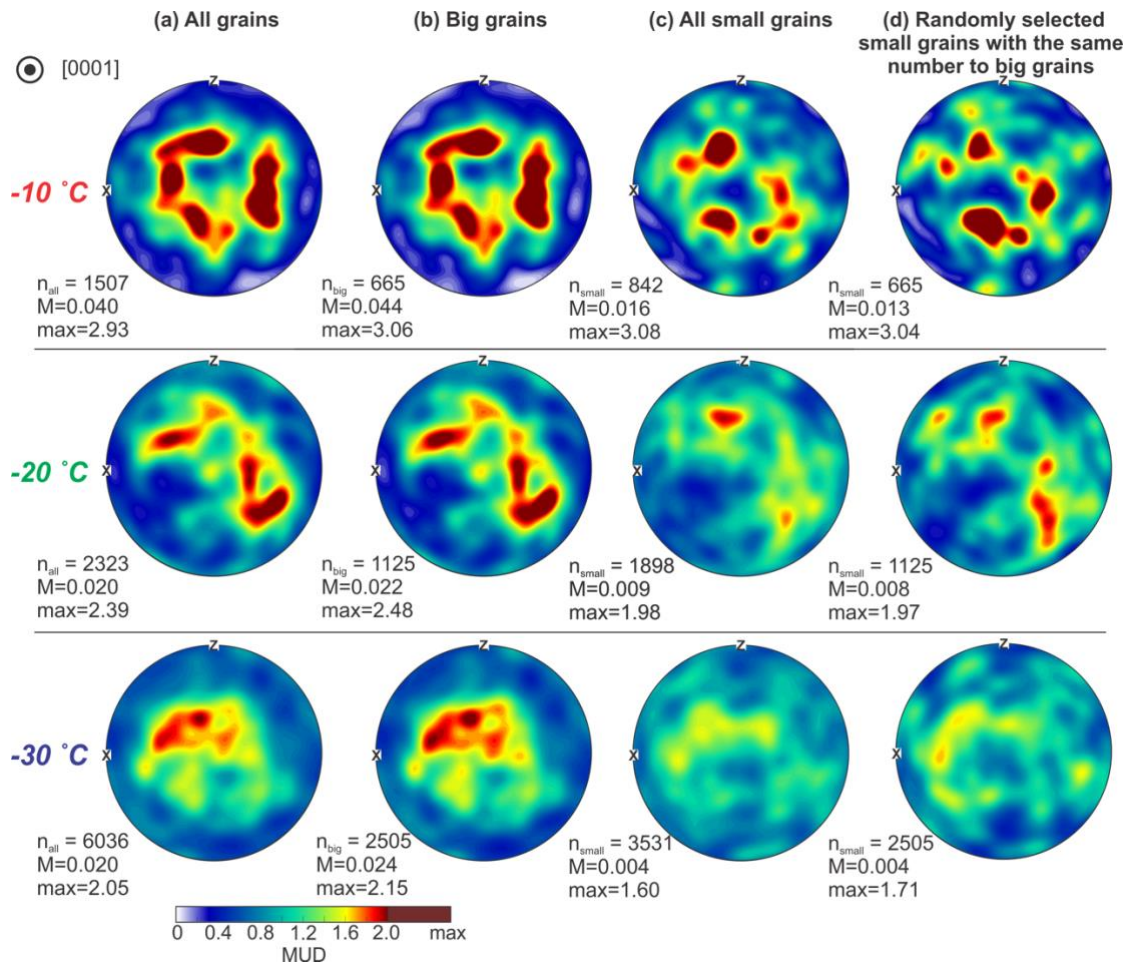
Figure 12. Contoured [0001] (*c*-axis) CPOs of **(a)** all grains, **(b)** "big grains", **(c)** "small grains" and **(d)** randomly selected "small" grains with the same grain number of "big" grains, for the samples deformed to ~12% strain at different temperatures. The number of grains, M-indices and max MUD values are marked on the bottom left of pole figures. The *c*-axis CPOs are calculated based on all pixels taken from the EBSD data with 5 µm step size. Compression axis is in the centre of the stereonets.
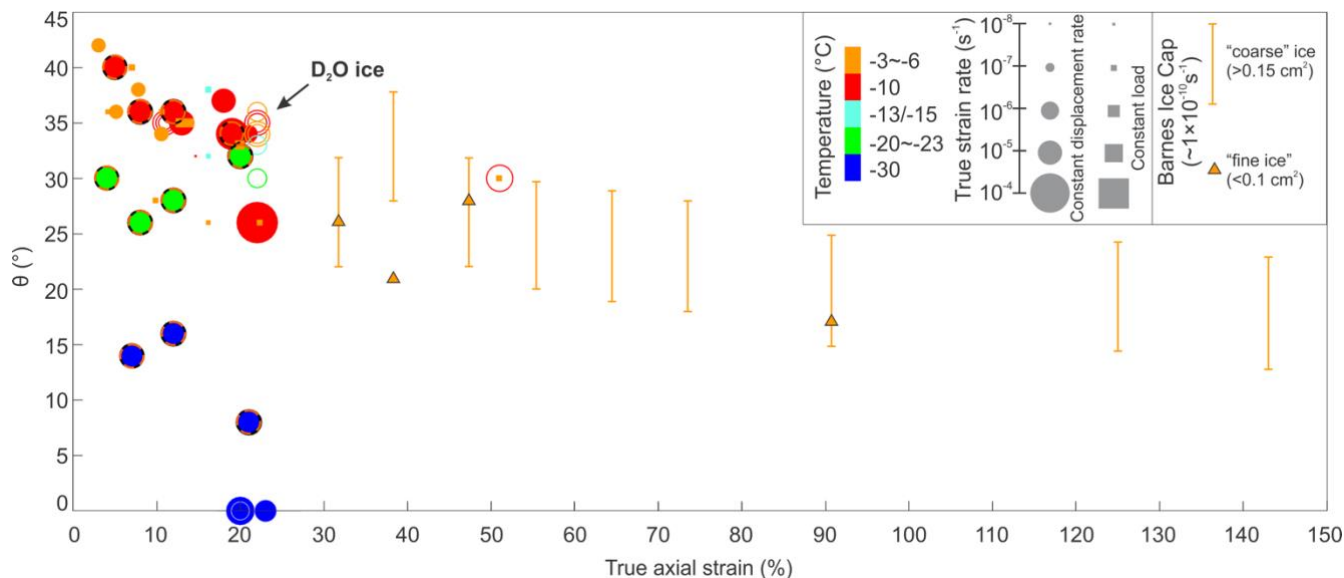
Figure 13. Plot of the relationship between the opening-angle, θ, of the cone-shaped c-axis CPO and the true strain. The data come from this study and the literature (Table 4). The data from naturally deformed ice (Hooke and Hudleston, 1981) are illustrated by bars with whiskers (cover uncertainty range of the open angle) for "coarse" ice and triangles with black edges for "fine" ice. The data from constant displacement rate experiments on D_2O ice (Piazolo et al, 2013; Wilson et al., 2020) are illustrated by hollow circles. The deformation of D_2O ice at -7 °C is a direct analogue for deforming H_2O ice at −10 °C (Wilson et al., 2019). The data from constant displacement rate experiments on H_2O ice (this study, Vaughan et al., 2017, Qi et al., 2017, Craw et al., 2018) are illustrated by filled circles. Data from this study are highlighted by orange-black edges. The data from constant load experiments (Jacka and Maccagnan, 1984; Jacka and Li, 2000; Montagnat et al., 2015) are illustrated by solid squares. Each marker is sized and coloured by the corresponding true strain rate and temperature, respectively. For all experiments the strain rate shown is the strain rate at the end of the experiment.
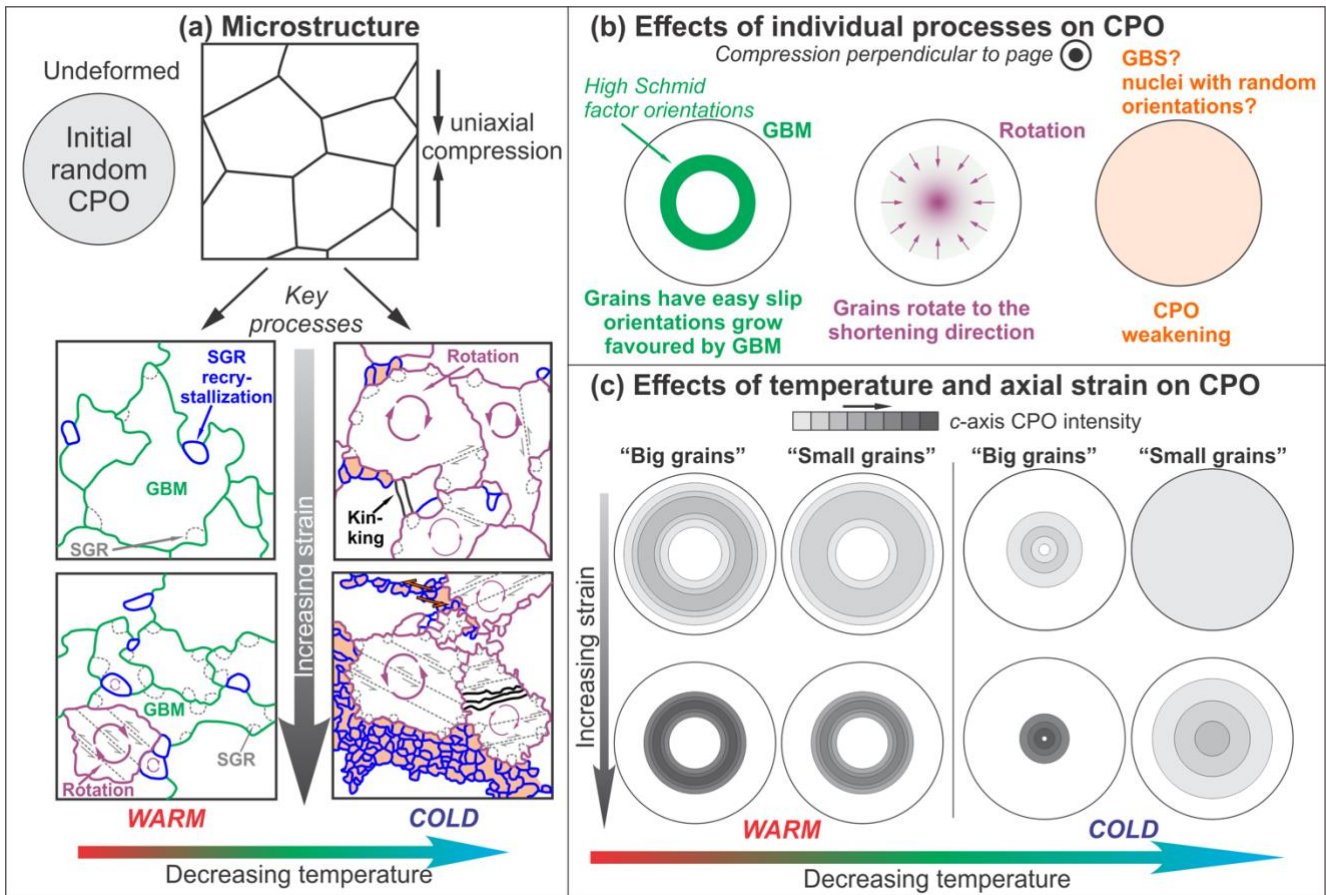
Figure 14. Schematic drawing of the microstructure and CPO development in ice deformed under uniaxial compression. **(a)** The effects of temperature and axial strain on the microstructural evolution. Grains undergoing different deformation processes are marked by different colours, with interpretations of the processes presented. **(b)** The effects of individual processes on CPO development. **(c)** The development of CPOs for "small grains" and "big grains" with strain at different temperatures. Starting point (shown in (a)) is a random CPO. SGR: subgrain rotation. GBM: grain boundary migration. GBS: grain boundary sliding.